


# Thermal Analysis of a High Speed Electrical Machine

by

Antonino La Rocca, MEng (Hons)

Thesis submitted to the University of Nottingham for the degree of Doctor of Philosophy

November 2015

# Abstract

This work has analysed, designed, commissioned and validated the performance of a novel cooling system for an innovative high speed, three-phase synchronous permanent magnet machine designed for an aero-engine starter/generator with a power rating of 45 kW and maximum speed of 32,000 rpm.

The cooling system designed consisted into inserting a 1 mm non-electrically conductive stator sleeve in the machine airgap, this separates the rotor region from the stationary components letting the rotor running dry at all times; the stator region can then be flooded with oil. Oil enters from one side of the machine through some radial openings impinging directly over the end-winding, it then flows through two rows of equally sized axial ducts located along the inner and outer diameter of the stator to give an even distribution of the coolant, and finally it flows over the surface of the rear end-winding and leaves the machine.

The thermal modelling was carried out by the joint use of Computational Fluid Dynamics (CFD) and Lumped Parameter Thermal Network (LPTN); this allowed the investigation of heat transfer phenomena and the optimisation of the cooling design.

CFD was primarily employed to investigate the fluid flow and to perform conjugate heat transfer analyses; these allowed the determination of heat transfer coefficients and the prediction of temperature distribution inside the machine.

Thermal networks were developed to investigate the heat flow through machine components, to perform the design optimisation and to maximise overall machine performance. A thermal network was also developed by the author to investigate the heat transfer phenomena inside the bearing chambers.

An experimental apparatus was designed and commissioned in order experimentally validate the thermal models developed. Temperatures, pressures and torque up to 20,000 rpm were recorded throughout the tests and data collected were compared to quantities predicted analytically and numerically. Maximum winding temperatures measured performing a short circuit test agree well with analytical and numerical prediction with a maximum difference of 10%; mechanical losses measured carrying out a no-load test agree well at speeds over 10,000 rpm with differences between 2 and 12%. Throughout tests, pressure drops were monitored across the machine and an agreement of 13% with prediction were achieved.

Design improvements are also proposed to further enhance the cooling of stator slots and of rotor components.

# Acknowledgements

I would like to thank my supervisors Prof Stephen J. Pickering, Prof Christopher Gerada and Dr. Carol Eastwick for their valuable support and encouragement throughout the duration of the PhD.

I am grateful to the whole team who collaborated to the project for their support. Thanks to Dr. Zeyuan Xu, Dr. Peter Connor, Dr. Puvaneswaran Arumugam and Dr. Sergei Bozhko.

Thanks to George Thornhill and John Hinchliffe for their help with constructing the experimental apparatus.

I am grateful to Clean Sky for the financial support of this PhD project.

Last, but no least, I give my special thanks to my wife and my whole family for their support and unconditional love.

# *Table of Contents*


1 Introduction ..... 1

1.1 Aim ..... 3

1.2 Objectives ..... 3

1.3 AEGART Project ..... 3

1.3.1 Machine Design and Functioning ..... 4

1.4 Thesis Structure ..... 6

2 Literature Review ..... 8

2.1 Introduction ..... 8

2.2 Heat Transfer in Electrical Machines ..... 8

2.2.1 Conduction Heat Transfer ..... 9

2.2.2 Convection Heat Transfer ..... 11

2.2.3 Radiation Heat Transfer ..... 13

2.3 Machine Losses ..... 14

2.3.1 Copper Losses ..... 14

2.3.2 Iron Losses ..... 15

2.3.3 Magnet Losses ..... 16

2.3.4 Windage Loss ..... 17

2.3.5 Bearing Losses ..... 18

2.4 Analysis Techniques ..... 18

2.4.1 Lumped Parameters Thermal Network ..... 19

2.4.2 Finite Elements Analysis ..... 19

2.4.3 Computational Fluid Dynamics ..... 20

2.5 Cooling of High Speed Electrical Machines ..... 21

2.6 State of Art of Cooling Systems for aerospace starter generators ..... 23

2.6.1 Air Cooling ..... 24

2.6.2 Fuel Cooling ..... 26

2.6.3 Oil Cooling ..... 27

2.7 Summary ..... 29

3 Cooling strategy identification ..... 31

3.1 Introduction ..... 31
3.2 Design criteria ..... 31
3.3 Design selection ..... 32
3.4 Design features ..... 34
3.4.1 Stator Sleeve ..... 34
3.4.2 Oil entry region ..... 37
3.4.3 Axial ducts and Flow deflector ..... 39
3.5 Summary ..... 41
4 Machine Analytical Thermal Modelling ..... 42
4.1 Introduction ..... 42
4.2 Design strategy ..... 42
4.3 Machine Thermal Modelling using MotorCAD ..... 43
4.3.1 Machine Geometry ..... 43
4.3.2 Definition boundary conditions and materials properties ..... 46
4.3.3 Cooling method implementation ..... 48
4.3.4 Generation Machine Thermal Network ..... 51
4.4 Thermal Modelling of Bearing Chambers ..... 53
4.4.1 Thermal Resistance between Rolling Elements and Races ..... 55
4.4.2 Convective Heat Transfer in Bearing Chambers ..... 56
4.4.3 Bearings Friction loss ..... 57
4.4.4 Overall Chambers' Material Properties ..... 59
4.4.5 Thermal network developed in MatLab-Simulink ..... 60
4.5 Summary of Analytical Modelling ..... 65
5 Machine Numerical Thermal Modelling ..... 66
5.1 Introduction ..... 66
5.2 Overview of CFD Theory ..... 66
5.3 Domains Analysed ..... 67
5.3.1 Airgap Domain ..... 68
5.3.2 Drive End (DE) Region ..... 73
5.3.3 Non-Drive End (NDE) Region ..... 75
5.3.4 Stator Ducts ..... 76

5.3.5 20 Degrees Machine Sector ..... 78
5.3.6 Full Machine Domain ..... 83
5.4 Summary of Numerical Modelling ..... 86
6 Experimental Facility ..... 88
6.1 Introduction ..... 88
6.2 Oil Circuit ..... 88
6.2.1 Thermal Measurement ..... 92
6.2.2 Flow rate Measurement ..... 93
6.2.3 Pressure Measurement ..... 94
6.2.4 Torque and Speed Measurement ..... 95
6.2.5 Data acquisition system ..... 96
6.2.6 Uncertainty Analysis ..... 96
6.3 Summary ..... 96
7 Results and Validation ..... 97
7.1 Introduction ..... 97
7.2 Wet Stator Cooling Performance ..... 97
7.2.1 Machine Temperature Rise ..... 97
7.2.2 Wet Stator vs Oil Jacket Cooling ..... 100
7.3 Testing and Validation ..... 102
7.3.1 Validation Machine Thermal Performance ..... 102
7.3.2 Validation Mechanical Losses ..... 106
7.3.3 Fluid Flow Validation ..... 109
7.4 Summary ..... 111
8 Thermal Modelling and Design Advancements ..... 113
8.1 Introduction ..... 113
8.2 Enhanced Stator Cooling ..... 113
8.3 Considerations on Enhancing Rotor Cooling ..... 117
8.4 Reduced Node Thermal Network ..... 119
8.5 Summary ..... 123
9 Conclusions and Recommendations ..... 125
9.1 Cooling Design Conclusions ..... 125

9.2 Thermal Modelling Conclusions ..... 127
9.2.1 Analytical Thermal Modelling ..... 127
9.2.2 Numerical Thermal Modelling ..... 127
9.3 Novelty in this Thesis ..... 128
9.4 Suggestions for Future Works ..... 129
Appendices ..... 136
A Dimensionless Numbers ..... 136
B Theory behind the Lumped Parameters Thermal Network Method 137
B.1 Evaluation of critical parameters of electrical machines ..... 140
B.1.1 Stator slots ..... 141
B.1.2 End Spaces ..... 143
B.1.3 Airgap ..... 144
B.1.4 Stator axial ducts ..... 145
B.1.5 Bearings ..... 147
B.2 Calculation Bearing Friction losses ..... 147
B.2.1 Simulink Thermal Network ..... 151
C Theory Behind CFD ..... 152
C.1 Fluid Flow Equations ..... 152
C.2 Turbulence Modelling ..... 153
C.3 Wall Treatment ..... 155
D CFD General Algorithm ..... 157
D.1 Domain Identification ..... 158
D.2 Geometry of Domain ..... 158
D.3 Domain Discretisation ..... 159
D.4 Solver Settings ..... 160
D.5 Convergence ..... 162
D.6 Post-Processing ..... 163
E PC Specification ..... 163

# *List of Figures*

Figure 1.1: Torque-Speed Characteristic of AEGART Starter/ Generator .....4
Figure 1.2: Machine External View [ref] .....5
Figure 1.3: Machine Axial Section.....5
Figure 2.1: Main Stator Components .....8
Figure 2.2: Machine Rotor.....9
Figure 2.3: Main Heat Flow Paths in an Electrical Machine.....9
Figure 2.4: Representation of Interface at a contact between two solids .....11
Figure 2.5: Oil jacket cooling.....22
Figure 2.6: Growth of On-Board Aircraft Power Demand [46].....24
Figure 2.7: Air Cooled Generator [47].....25
Figure 2.8: Jet Engine Oil Circuit [47].....28
Figure 3.1: Wet Stator cooling .....33
Figure 3.2: Wet Stator radial section.....33
Figure 3.3: Stator sleeve connection at non-drive end .....36
Figure 3.4: Stator sleeve connection at drive end.....36
Figure 3.5: Cross-section highlighting the location of the stator sleeve…….37
Figure 3.6: Main oil inlet.....38
Figure 3.7: Inlet oil path .....39
Figure 3.8: Stator design.....40
Figure 3.9: Flow deflector .....41
Figure 4.1: Modelling Flow Diagram.....43
Figure 4.2: Machine Geometry Creation - Axial Dimensions.....44
Figure 4.3: Machine Geometry Creation - Radial dimensions.....44
Figure 4.4: Creation of Stator Windings .....45
Figure 4.5: Stator End-Space.....50
Figure 4.6: MotorCAD thermal network of machine designed.....52
Figure 4.7: Cross-sectional view of bearings used.....53
Figure 4.8: Cross-sectional view of bearing chambers.....54
Figure 4.9: Bearing thermal resistances showing node locations.....60
Figure 4.10: Bearing Chamber Conductive Path.....61
Figure 4.11: Chamber full thermal network.....62
Figure 4.12: Active Rotor Thermal Network .....63
Figure 4.13: Schematic Active Rotor Thermal Network.....64
Figure 4.14: Schematic Full Rotor Thermal Network.....64
Figure 5.1: Airgap Domain Considered .....69
Figure 5.2: Airgap Mesh.....70
Figure 5.3: Normalised velocity profiles across airgap.....71

Figure 5.4: Windage loss ..... 71
Figure 5.5: Airgap Heat Transfer Coefficient ..... 72
Figure 5.6: DE End Region Domain ..... 73
Figure 5.7: NDE End Region Domain ..... 75
Figure 5.8: Discretisations duct domain ..... 77
Figure 5.9: Velocity profiles inside stator ducts ..... 78
Figure 5.10: 20 degrees machine domain ..... 79
Figure 5.11: Oil Domain ..... 79
Figure 5.12: Air Domain ..... 80
Figure 5.13: 2D axisymmetric slice of 20° sector of full machine ..... 80
Figure 5.14: Results of the conjugate heat transfer analysis ..... 82
Figure 5.15: Section view Full 360° Machine Model ..... 83
Figure 5.16: Oil Inlet port domain ..... 84
Figure 5.17: Mesh of 360° Machine Model ..... 85
Figure 6.1: Schematic of Test Rig ..... 88
Figure 6.2: Oil Circuit ..... 89
Figure 6.3: Hydraulic machine connections ..... 90
Figure 6.4: Control Main Oil Line ..... 90
Figure 6.5: Thermocouple location ..... 92
Figure 6.6: Oil flow meter ..... 93
Figure 6.7: Pressure transducer ..... 94
Figure 6.8: Torque transducer ..... 95
Figure 7.1: Temperature Plot Cross-Sectional View – Oil inlet at 120°C ..... 98
Figure 7.2: Predicted maximum Temperature Rises at Full Power (rise above inlet oil temperature of 120°C) ..... 99
Figure 7.3: Predicted Temperature Rises Using Different Cooling Options Using MotorCAD Thermal Network (oil inlet temperature: 120 °C) ..... 101
Figure 7.4: Maximum Windings Temperature rise Short Circuit Test ..... 105
Figure 7.5: No-Load Losses Trend ..... 108
Figure 7.6: Pressure Contour Inlet Region ..... 110
Figure 7.7: Pressure Contour Stator Region ..... 111
Figure 8.1: Cross-Section of Rectangular Coils for future Machines ..... 113
Figure 8.2: Detail of New Stator Winding (Rectangular Conductors) ..... 114
Figure 8.3: Slot Configurations for stator with rectangular coils ..... 114
Figure 8.4: Simplified Stator Model ..... 115
Figure 8.5: Temperature Contours of Cases Analysed ..... 116
Figure 8.6: Temperature Contour Case 2 without flow in outer ducts ..... 117
Figure 8.7: Potential Rotor cooling enhancement ..... 118
Figure 8.8: Reduced Thermal Network ..... 120
Figure 8.9: Models comparison ..... 123

Figure B.1: Discretisation ..... 138
Figure B.2: Conductive thermal resistance ..... 139
Figure B.3: Typical wires distribution in slots ..... 141
Figure B.4: Representation Layer Model ..... 142
Figure B.5: Bearing Power Losses ..... 151
Figure C.1: Near-Wall Regions [96] ..... 155
Figure C.2: Wall Modelling Approaches [96] ..... 156
Figure D.1: CFD process ..... 157
Figure D.2: Typical Mesh Elements ..... 159
Figure D.3: Control Volume ..... 161

# *List of Tables*

Table 2.1: Typical Thermal conductivity of Machine parts ..... 10
Table 2.2: Typical Values of Emissivity ..... 13
Table 2.3: *A*, α and β coefficients for different Flow Regimes [26] ..... 17
Table 2.4: Standard Atmosphere [50] ..... 26
Table 2.5: Specifications of Aviation Fuels ..... 27
Table 2.6: Summary of In-Flight Cooling Methods ..... 28
Table 4.1: Employed materials ..... 47
Table 4.2: Machine losses at 32,000 rpm ..... 48
Table 4.3: Oil properties ..... 49
Table 4.4: Numerical data implemented ..... 50
Table 4.5: Nodes input data ..... 51
Table 4.6: Bearing dimensions ..... 53
Table 4.7: Thermal conductance of bearings ..... 56
Table 4.8: Bearing chambers overall heat transfer coefficients ..... 57
Table 4.9: Bearings losses in W at 32,000 rpm ..... 59
Table 4.10: Heat Removed by Lubricant at 32,000 rpm ..... 64
Table 5.1: First cell heights ..... 70
Table 5.2: 20 degress sector versus 360 degrees domain ..... 74
Table 5.3: DE End Region boundary conditions ..... 75
Table 5.4: NDE End Region Parametric study ..... 76
Table 5.5: Mesh Details 20° Machine Sector ..... 81
Table 5.6: Mesh details of 360° Model ..... 85
Table 5.7: Comparison Machine key temperatures ..... 86
Table 7.1: Machine Losses Short Circuit Test ..... 103
Table 7.2: Thermal Measurements Short Circuit Test ..... 104
Table 7.3: SC Test Temperatures Comparison ..... 105
Table 7.4: Power Losses No-Load Test ..... 108
Table 7.5: Pressure Readings ..... 109
Table 7.6: Inlet Region Data ..... 110
Table 8.1: Volumetric Heat Input ..... 116
Table 8.2: Cases Comparison ..... 116
Table 8.3 Nodes List ..... 121
Table 8.4: List of Thermal Resistances ..... 122
Table B.1 Thermal-Electrical Analogy ..... 137
Table B.2: End space curve fit coefficients ..... 143
Table B.3: Bearing equivalent interface gap ..... 147

Table B.4: S and R values for paired angular contact bearings.....149
Table B.5: S and R values for cylindrical roller bearings.....150
Table B.6: Kz values .....150
Table E.1: PC specification .....163

# *Nomenclature*

Symbols

| Symbol | Description | Units |
|---|---|---|
| A | Surface area | $m^2$ |
| $C_M$ | Torque coefficient | |
| Cp | Heat Capacity | J/kgK |
| $C_{th}$ | Thermal capacity | J/K |
| D | Diameter | m |
| $D_h$ | Hydraulic diameter | M |
| h | Heat transfer coefficient | $W/m^2K$ |
| I | Electric current | Ampère |
| $f$ | Frequency | Hz |
| $f_D$ | Darcy Factor | |
| k | Thermal conductivity | W/mK |
| l | Length | m |
| M | Torque | Nm |
| Nu | Nusselt | |
| p | Pressure | Pa |
| P | Power | Watts |
| Q” | Heat flux | $W/m^2$ |
| Re | Reynolds | |
| R | Resistance | Ω (ohms) |
| $R_{th}$ | Thermal resistance | K/W |
| r | radius | m |
| T | Temperature | K |
| u | velocity | m/s |
| $\bar{u}$ | Mean velocity | m/s |
| $\dot{v}$ | Volume flow rate | $m^3/s$ |
| y | distance | m |
| $y^+$ | Near wall distance | |

Greek symbols

| Symbol | Description | Units |
|---|---|---|
| α | Linear temperature coefficient | |
| δ | Density | $kg/m^3$ |
| ε | Emissivity | |
| μ | Dynamic viscosity | kg/ms |
| σ | Stefan-Boltzmann constant | $W/m^2K^4$ |
| τ | Shear strees | Pa |
| ν | Kinematic viscosity | $m^2/s$ |
| ω | Rotational speed | rad/s |

Abbreviations

| Abbreviation | Description |
|---|---|
| AC | Alternating current |
| DC | Direct current |
| CFD | Computational Fluid Dynamics |
| MRF | Moving reference frame |
| SM | Sliding Mesh |
| 2D | 2 dimensional |
| 3D | 3 dimensional |

# 1 Introduction

An aero-engine starter generator acts as a motor to start the engine. Once the engine is operational it is driven and acts as a generator to provide power for the aircraft electrical systems. Air transportation has significantly grown during last fifty years at a rate of 9% [1] per year; this has a direct impact on the emission of pollutants and particularly the production of $CO_2$, indeed it has been estimated that the civil air transport will account the 3% of the man-made $CO_2$ emissions by the 2050 [2]. This significant growth and the strict limitations imposed on the pollutants emissions, has pushed the aerospace industry to move towards more efficient designs. The strategy adopted during last decade consists of replacing most of the non-propulsive aircraft systems such as mechanical, hydraulic, and pneumatic with electrically driven actuators; this design concept has been named More Electric Aircraft (MEA) [3].

The advantage of electrical systems is the high efficiency achievable, usually above 90% [4]; this can lead to improve the overall aircraft performance and at the same time reducing the weight and hence reducing fuel consumption. Although electrical systems are usually highly efficient, this design strategy is leading to an increasing on-board power demand, growing from the 0.2 MW for the Boeing 747 to 1.5 MW for the Boeing 787. The main challenge is then the generation of high power at high efficiency whilst minimising size and weight; the achievement of these goals requires not only an accurate electromagnetic but also mechanical and thermal design. The optimisation of all these aspects of the design can indeed lead to reliable and efficient systems.

The cooling of electrical machines is of fundamental importance in the design process; an effective thermal management approach leads to a reduction in the temperature dependent losses and thus increases the overall efficiency of the machine; therefore the amount of fuel required by the engine to drive the alternator is reduced [3]. The choice of using a direct liquid cooling technique

can furthermore lead to significantly reduce the machine size and weight and increase the power density. Lower temperatures can increase the lifetime of the machine as the deterioration of the winding insulation is slowed down; just 10°C temperature rise can indeed reduce the insulation life by 50% [5].

The thermal management of electrical machines has become the object of much attention during the last decade. In the past, as the literature shows, [6] the electromagnetic aspects of the electric machines have been largely investigated but the thermal aspects have been the object of fewer detailed studies. This is probably because the design of the electrical machines has been mainly considered a matter for electrical engineering.

In the past, the investigation of the thermal performances of the machines was usually based on the prior knowledge of parameters related to the operating conditions such as winding to ambient thermal resistance, housing heat transfer coefficient, etc [7]. These parameters were generally estimated from test conducted on pre-existing machines and catalogues [6]. In reality very complex heat transfer phenomena involving conduction, convection and radiation take place in the electrical machine and they are also related to the electromagnetic phenomena. [7]

A wide range of modelling tools based numerical and analytical approaches is nowadays available for the investigation of the thermal aspects related to the electrical machines. The most common analysis methods used, especially during last few years are the following:

- Thermal network based on the lumped parameters
- Computational fluid dynamics (CFD)
- Finite elements analysis (FEA)

## 1.1 Aim

The project aim is to develop a novel cooling solution for an aircraft electrical starter/generation system capable of maximising the performance and minimising size and weight. More details about the project are provided in section 1.3.

## 1.2 Objectives

This work has the following objectives

1) Investigate the state of art of the cooling of electrical machines for aerospace application.

2) Understand the power losses distribution for the given machine design and identify a suitable and effective cooling strategy.

3) Use of analytical and numerical methods (Lumped parameters thermal network and Computational Fluid Dynamics) for the investigation of the temperature fields and optimisation of the cooling capabilities of the cooling strategy adopted.

4) Experimental validation of the analytical/numerical model.

5) Identify further potential solutions to further enhance the cooling of the starter/generator.

## 1.3 AEGART Project

This work is part of an EU-funded project AEGART (Aircraft Electrical Generation System with Active Rectification and Health Monitoring). AEGART aims to develop an innovative aircraft electrical starter-generation system for a small aircraft; this includes the electrical machine and the power electronic converter.

In this thesis the thermal management of the starter/generator is developed; this includes the identification of the cooling strategy, thermal modelling of the machine, thermal design optimisation and experimental validation.

### 1.3.1 Machine Design and Functioning

A three-phase synchronous permanent magnet machine was the machine type identified as starter/generator. As shown in Figure 1.a the machine runs as motor during engine start and supplies a constant torque $T_{start}$ (42 Nm) from start to 8,000 rpm ($\omega_{start}$). Between $\omega_{start}$ and $\omega_{min}$ the machine provides the same power to accelerate the engine. Between $\omega_{min}$ and $\omega_{max}$ the machine works as generator providing a constant power of 150 kW; as the machine is designed to work as generator for most of the time it is designed to maximise the performance between 19,000 and 32,000 rpm.

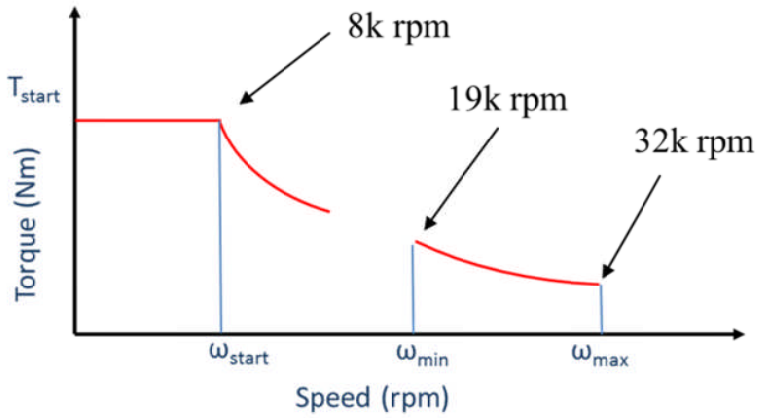



**Figure 1.a: Torque-Speed Characteristic of AEGART Starter/ Generator**

In Figure 1.b and Figure 1.c an external and section views are shown and main components are highlighted. The machine has an overall length of 200 mm and an outer diameter of 170 mm; the total mass is around 20 kg. A direct liquid cooling where part of the machine is flooded with oil was designed in order to achieve higher power density and maximise the overall performance; this will be extensively described within this work. More information about all components and materials used will be provided in Chapters 3 and 4.

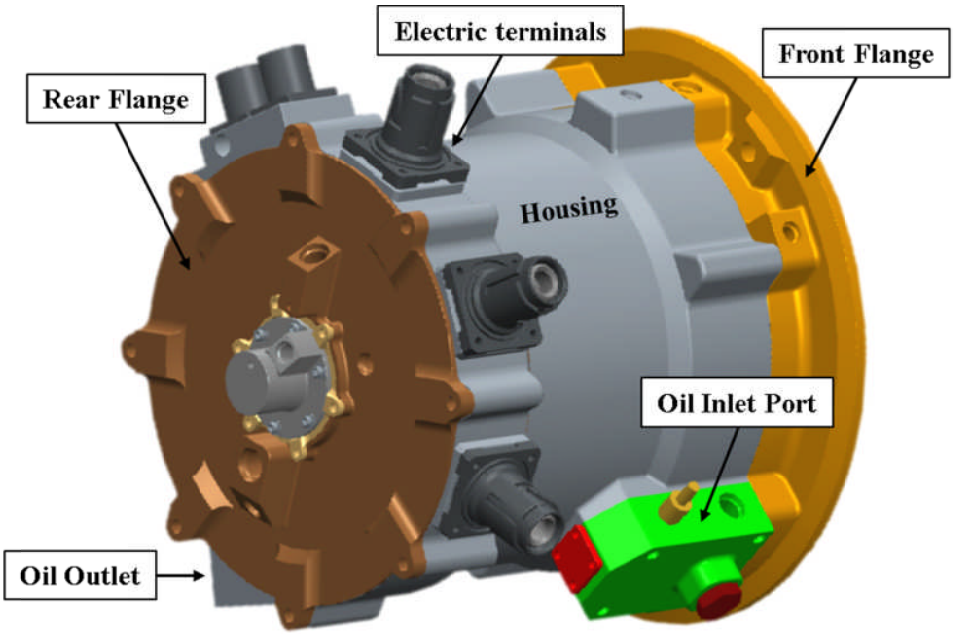



**Figure 1.b: Machine External View**

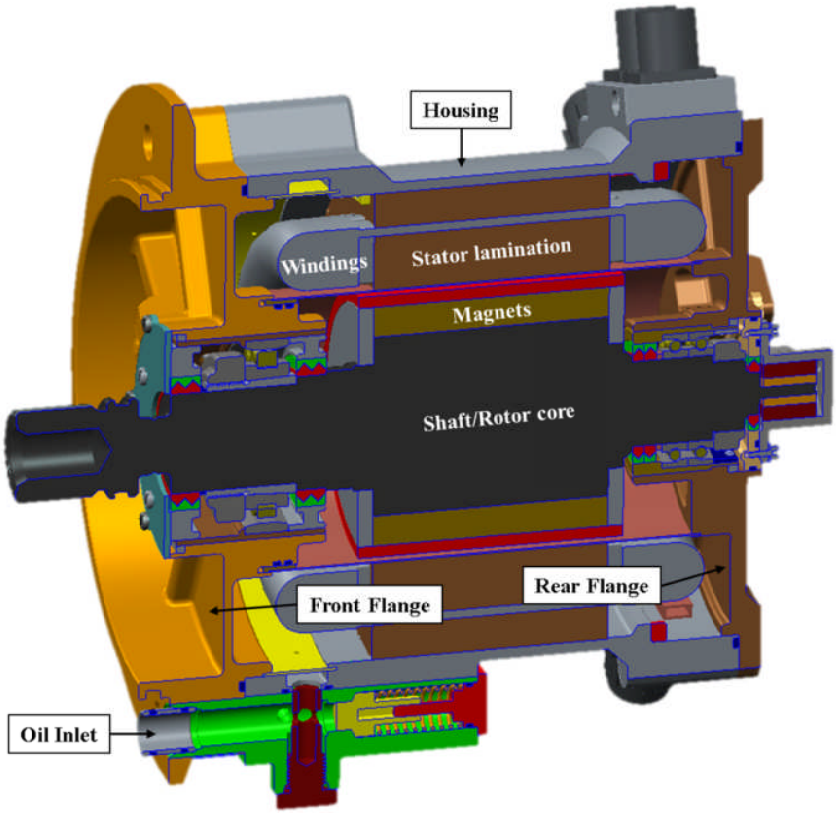



**Figure 1.c: Machine Axial Section**

During the motoring phase the three phases are powered by feeding electrical power to the stator windings through the electrical terminals shown in Figure 1.b; due to the phases' delay a rotating magnetic field is generated in the stator, the permanent magnets located in the rotor try to "follow" this field causing the rotation of the rotor body and hence mechanical power is provided from the shaft.

In generation mode the shaft receives mechanical power from the engine; the rotation of the permanent magnets produce a rotating magnetic field, this magnetic field induces a back emf (electro-motive force) in the stator windings according Faraday's Law. The potential induced generates current in the copper windings and hence electric power.

## 1.4 Thesis Structure

- Chapter 2 introduces extensively the heat transfer problem in electrical machines and provides a literature review of the state of the art of cooling of aerospace generator and more in general of high speed electrical machines.
- Chapter 3 describes the cooling option designed and highlights its main features.
- Chapter 4 shows how the machine and bearing analytical thermal networks were built.
- Chapter 5 describes the CFD thermal modelling of the machine and of some of its critical areas.
- Chapter 6 describes the experimental apparatus designed and used to collect data during testing.
- Chapter 7 shows a comparison between results predicted using analytical/ numerical approaches and provides experimental validation for the models used.

- Chapter 8 describes further design and modelling improvements aiming to enhance the cooling of the machine and to improve the thermal analysis.
- Chapter 9 makes conclusions and future recommendations for the modelling and analysis of the electrical machine.

# 2 Literature Review

## 2.1 Introduction

This chapter will cover a review of thermal aspects related to the electrical machines. The nature of the major power losses in electrical machines and heat transfer methods will be described. An overview of the modelling techniques used to carry out thermal analyses will be also provided. Finally the state of the art of the cooling of starter generators for aerospace applications will be investigated.

## 2.2 Heat Transfer in Electrical Machines

Heat transfer in electrical machines occurs according to the three heat exchange modalities existing: conduction, convection and radiation. Due to the anisotropy of some the machine parts and complex geometries such as windings and bearings, the study of these phenomena is not straightforward. Figure 2.a and Figure 2.b illustrate main elements constituting the starter/generator designed and whilst Figure 2.c shows the major thermal flow paths in a typical electrical machine.

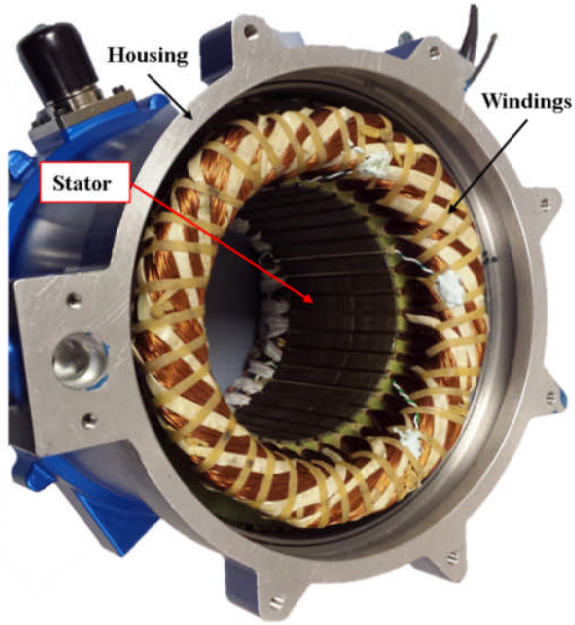



**Figure 2.a: Main Stator Components**

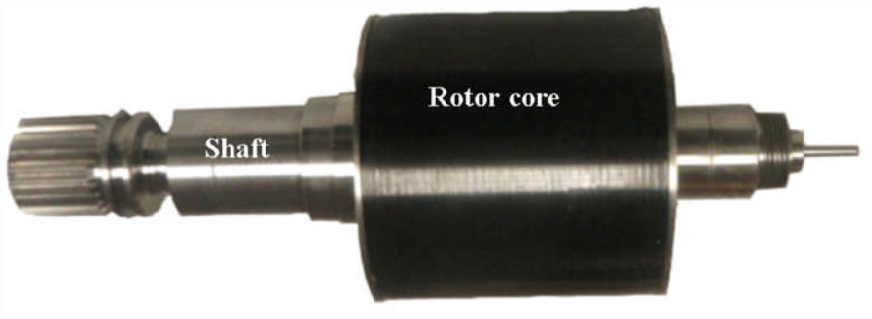



**Figure 2.b: Machine Rotor**

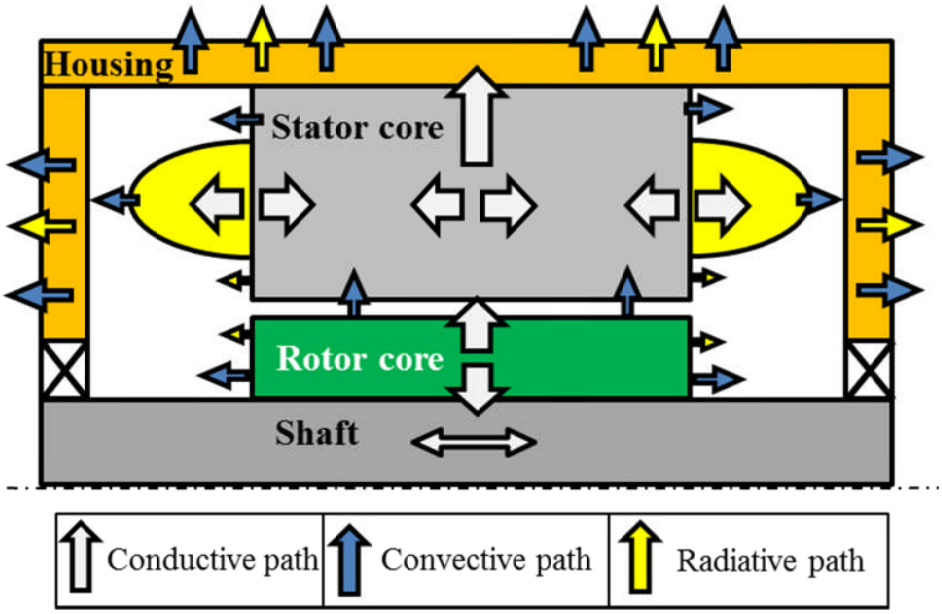



**Figure 2.c: Main Heat Flow Paths in an Electrical Machine**

### 2.2.1 Conduction Heat Transfer

Conduction takes place in the solids when a temperature gradient exists. The amount of heat transferred along one direction $q_x$ in W is evaluated according the Fourier's law as in Equation 2.1 [8]:

$$q_x = k(T)A\frac{\delta T}{\delta x} \qquad 2.1$$

where the coefficient $k$ in W/mK is the thermal conductivity of the material, $A$ in $m^2$ is the total area perpendicular to the direction of heat transferred, $\delta T$ is the temperature gradient between the surfaces considered in K and $\delta x$ is the material thickness expressed in m. The thermal conductivity is a temperature dependent property of the material may vary more or less significantly according the material used and the range of the temperature considered. Table 2.1 indicates some typical values of thermal conductivity of some parts of a typical electrical machine: [4, 9]

| **Material** | **Part** | **k (W/mK) –at ambient temperture** |
|---|---|---|
| Al-Si 20 | Frame | 161 |
| Steel (0.5%C) | Shaft | 54 |
| Carbon Steel(1.5%C) | Stator and rotor core | 36 |
| Copper | Stator winding | 386 |
| Unsaturated polyester | Stator winding impregnation and slot insulation | 0.2 |
| NdFeB | Permanent magnet | 9 |
| Samarium-Cobalt | Permanent magnet | 11.6 |

**Table 2.1: Typical Thermal conductivity of Machine parts**

In electrical machines some materials employed are not isotropic so the material properties are direction dependent; for example the stator iron, the rotor core and sometimes even the magnets are laminated, thus the thermal conductivity changes according the direction considered, radial or axial. However, the determination of the axial thermal conductivity is still a topic

which requires further investigation as it is a problem which involves many variables, such as lamination thickness, lamination surface finish and inter-lamination insulation material [10].

Other factors, such as the insulation of the winding, interface between the lamination and the frame and the interface between lamination and the winding should be also considered as they can determine variations of the overall thermal conductivity. In some applications, especially where the heat is dissipated through the frame, particular attention must be paid to the interface between the lamination and the frame; indeed if air gaps exists at the interface due to significant surface roughness as in shown in Figure 2.d, the overall thermal resistance may be negatively affected [11].

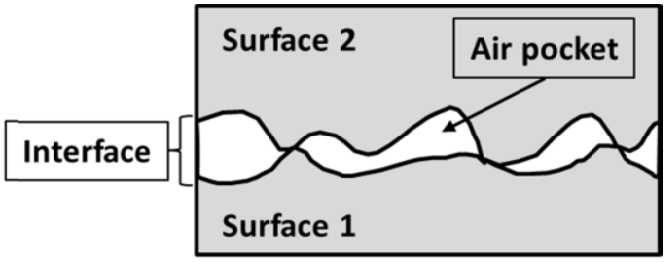



**Figure 2.d: Representation of Interface at a contact between two solids**

### 2.2.2 Convection Heat Transfer

Convective heat transfer occurs when a temperature gradient exists between a solid surface and a fluid in motion. If the fluid motion is caused by natural buoyancy effects the convection is natural, otherwise, if the fluid is pushed by external mechanisms the convection is forced [8]. This mode of heat transfer is described by the Newton's law in Equation 2.2:

$$q = h\,A\,(T_{wall} - T_{fluid}) \qquad 2.2$$

Where $h$ is the convective heat transfer coefficient in W/m$^2$K and $(T_{wall} - T_{fluid})$ is the temperature gradient between the wall and the fluid. The determination of $h$ requires a detailed analysis of the problem considered, that is because this parameter is influenced by many factors such as the fluid state,

fluid properties, the flow regime, geometry of the surface and surface finish. Typical values of $h$ for natural convection in air are between 5 and 25 W/m$^2$ K, for forced convection main between 10 and 300 W/m$^2$ K and between 50-20k W/m$^2$ K if liquids are used as cooling medium [8] .

The study of the convective heat transfer is usually conducted using dimensionless numbers such as Nusselt (*Nu*), Grashof (*Gr*), Prandlt (*Pr*), Reynolds (*Re*) [12]:

- **Nusselt** number: evaluates the effectiveness of the convective heat transfer respect the conductive heat transfer.
- **Grashof** number: is the ratio between the buoyancy and the viscous force.
- **Prandlt** number: is the ratio between the momentum and the thermal diffusivity of the fluid. In practice it needs to evaluate the relative thickness of the momentum and the thermal boundary layers.
- **Reynolds** number: it is the ratio between the inertia and the viscous force. This number indicates if the flow is laminar or turbulent.

Equations of the dimensionless numbers are provided in Appendices.

Due to the complex geometries and fluid flows, the end space regions of electrical machines are usually the most challenging areas to be examined in terms of prediction of convective heat transfer coefficients and hence, of heat exchanged. For this reason many analytical and experimental studies have been conducted [10, 11, 13-15] to investigate the phenomena occurring in this region.

As shown in [13, 15] numerical approached based on the Computational Fluid Dynamics were adopted for predicting both fluid flow and heat transfer.

### 2.2.3 Radiation Heat Transfer

Radiative heat transfer is based on the fact that all bodies emit a thermal radiation. The thermal radiation is electromagnetic radiation whose magnitude is function of the material of the body, its surface and its temperature. The heat flux exchanged between two surfaces is defined by the Stefan-Boltzmann law in Equation 2.3 [12]:

$$q'' = \varepsilon \sigma T^4 \qquad 2.3$$

Where ε is the emissivity of the surface, σ is the Stefan-Boltzmann constant ($5.6703\ 10^{-8}$ W/m$^2$K$^4$) and T is the surface temperature.

The emissivity ε depends upon the material; Table 2.2 shows typical values of emissivity for some materials commonly used in electrical machines [4]:

| **Material** | **Emissivity** |
|---|---|
| Polished aluminium | 0.04 |
| Polished copper | 0.025 |
| Mild steel | 0.2-0.3 |
| Cast iron | 0.3 |
| Stainless steel | 0.5-0.6 |
| Black paint | 0.9-0.95 |
| Aluminium paint | 0.5 |

**Table 2.2: Typical Values of Emissivity**

The heat exchanged by radiation does not usually represent a significant part of the total heat transferred in the machine, so that for some applications it can be neglected [15]; nevertheless for applications in which machine cooling relies on natural convection, the radiative heat transfer can be considerable and it must be accounted for.

## 2.3 Machine Losses

To effectively investigate the heat transfer phenomena occurring in an electrical machine a better understanding of the nature of heat sources and their distribution is required.

Depending upon their nature, the losses can be classified as:

- Electrical: consist of purely resistive losses generated in the windings generally made of several thin copper wires.
- Electro-Magnetic: are generated in the stator lamination and rotor and they are caused by the variation of magnetic fields.
- Mechanical: are generated due the friction of rotating components; these occur mainly in bearings and in the annular airgap between rotor and stator.

Typically in an electrical machine total power losses converted into heat represent the 5-10% of the input power [4].

### 2.3.1 Copper Losses

Copper losses usually represent the main loss occurring in electrical machines [4, 6]. The electric power flowing through conductors is partly converted into heat and the amount of heat is proportional to the resistance of the conductors and the square of the current as shown in Equation 2.4 , this phenomena is also known as Joule's effect.

$$P_{cu} = R_{operation}\, I^2 \qquad 2.4$$

where $I$ is the current in Ampère and $R_{operation}$ is the electrical resistance of conductors at the operating temperature expressed in Ω. The conductors' resistivity varies with the operating temperature and this can be quantified by using Equation 2.5 [16] where $\alpha_{ref}$ and $R_{ref}$ are the linear temperature coefficient

and the electrical resistance at the reference temperature $T_{ref}$. For copper at 20°C $\alpha_{ref}$ is 0.39%/°C.

$$R_{operation} = R_{ref}\left(1 + \alpha_{ref}\left(T_{operation} - T_{ref}\right)\right) \quad 2.5$$

It can be seen that these losses are strongly dependent upon the working temperature; as example a temperature rise of 50°C leads to an increase of the resistivity and hence power loss of around 20 %. An intensive cooling of the windings can then contribute to significantly reduce this loss.

When conductors are subjected to high frequency alternating currents like in high speed applications an additional loss component, called AC winding loss, need to be taken into account when evaluating copper losses. Two effects are mainly responsible for AC losses, these are the skin effect and the proximity effect [17].

Skin effect is the tendency for high-frequency currents to flow on the surface of a conductor so the bigger conductors are more significant the effect will be. The proximity effect is the tendency for current to flow in undesirable patterns due to current unbalance between conductors; this effect is usually contrasted by grouping and twisting the conductors' strands together in order to have the same current in each conductor [17].

As can be noted the AC loss component depends not only on the material used but also by its geometry, by the conductors' manufacturing process and also by the winding process. Due to the unpredictability of some factors listed above, the prediction of this loss component is not easily approachable analytically or numerically, it follows that an experimental approach is required.

### 2.3.2 Iron Losses

Core losses taking place in the stator lamination represents the second of the main losses [4] in permanent magnet machines. They can be divided into two components, hysteresis and eddy current loss [18], Equation 2.6.

$$P_I = P_h + P_{eddy} \quad (2.6)$$

The hysteresis loss is caused by the variations of the magnetic field; they are related to the energy required in moving domain walls from a naturally occurring state of orientation of that of the applied external field. The eddy current loss is associated to the variation of the magnetic field applied; as ideally the rotor does not see a changing magnetic field this loss can be considered mainly occurring in the stator iron. [19, 20]. These two loss components can be predicted numerically but also analytically using Equation 2.7 and Equation 2.8. Eddy currents are induced by the variation of the magnetic field according the Faraday's Law.

Hysteresis loss $$P_h = k_h \, f \, B_m^{\alpha} \quad (2.7)$$

Eddy current loss $$P_{eddy} = \frac{G_{lam} \, l^2}{12\tau} \int_0^{\tau} B(t)dt + 8.67 \, k_e f^{1.5} B_m^{1.5} \quad (2.8)$$

Where $G_{lam}$ is the lamination electrical conductivity, $l$ the lamination thickness, $f$ the frequency of flux density waveform, $B_m$ is the peak flux density and the constants $k_e$ and $k_e$ depend on the grade of the lamination material.

Iron losses can also depend on the lamination cutting process as shown in [21]. Studies conducted [22, 23] show that the use of alternative materials and an accurate design of slots (removal of sharp corners, teeth sizing) can lead to reduce this power loss.

### 2.3.3 Magnet Losses

The management of these losses is important because high temperatures can lead to the demagnetisation of the magnets and then, this can significantly affect the performance of the whole machine [24].

Losses occurring in permanent magnets are often neglected, however for some applications they need to be accounted for. As magnets are electrically conductive the magnetic flux passing through them induces eddy currents generating heat.

As well as iron losses, magnets losses can be evaluated either numerically or analytically as shown in [25].

### 2.3.4 Windage Loss

Windage is the power loss generated due to the viscous friction between rotating surfaces and the surrounding fluid. For concentric cylinders the power loss generated into the airgap between the cylinders can be estimated as in Equation 2.9 [4], where $k$ is a dimensionless roughness coefficient of the moving surface (for slotless and smooth surfaces $k$ = 1, for slotted surface $k$<1, for rough surfaces $k$>1), $\rho$ is the density of the fluid in kg/m$^3$, $\omega$ is the rotating speed in rad/s, $D_r$ and $l_r$ are the rotor outer diameter and length in m and $C_M$ is the torque coefficient.

$$P_w = \frac{1}{32}\, k\, C_M \pi\, \rho\, \omega^3 D_r^4\, l_r \qquad 2.9$$

The torque coefficient $C_M$ is calculated as in Equation 2.10 where $\delta$ is the airgap length in m, Re is the Reynolds number and coefficients $A$, α and β depend on the flow regime as shown in Table 2.3.

$$C_M = A \left(\frac{2\,\delta}{D_r}\right)^{\alpha} Re^{\beta} \qquad 2.10$$

| **Flow Regime** | ***A*** | **α** | **β** |
|---|---|---|---|
| Laminar: Re < 64 | 10 | 0.3 | -1 |
| Transition: 64 < Re < 500 | 2 | 0.3 | -0.6 |
| Turbulent I: Re < $10^4$ | 1.03 | 0.3 | -0.5 |
| Turbulent II: Re > $10^4$ | 0.065 | 0.3 | -0.2 |

**Table 2.3: *A*, α and β coefficients for different Flow Regimes [26]**

As the problem involves rotation the Taylor-Couette Reynolds number is used, this can be calculated using Equation 2.11 where $\mu$ is the fluid dynamic viscosity in kg/ms.

$$Re = \frac{\rho\ \omega\ D_r \delta}{2\ \mu} \tag{2.11}$$

As can be seen the windage loss mainly depends on the geometry, the rotating speed and the nature of the fluid.

### 2.3.5 Bearing Losses

Bearing losses are generated by the friction between the rotating elements and the races where these elements move. This power loss is function of several factors such as shaft speed, bearing type, lubricant used and the loads applied. In [4] a very generic approach for the estimation of this friction loss and is shown in Equation 2.12 where $\mu_0$ is a friction coefficient provided by manufacturers, F is the load applied in to the bearing in N and $D_b$ is the bearing inner diameter in m.

$$P_B = 0.5\ \omega\ \mu_0 F\ D_b \tag{2.12}$$

For a more accurate prediction of this power loss more complex analytical models are available. More detailed information will be provided in sections 4.5.3 and appendix B.2.

## 2.4 Analysis Techniques

Nowadays many techniques to investigate the thermal aspects of electrical machines exist. Depending on the approach, they can be split into analytical and numerical methods:

- Analytical: thermal network based on the lumped parameters (section 2.4.1 below).
- Numerical: finite elements analysis (FEA), computational fluid dynamic (CFD) (sections 2.4.2 and 2.4.3 below).

Improvements of these techniques, proposed during last few years, allowed more accurate thermal analyses to be performed [7].

### 2.4.1 Lumped Parameters Thermal Network

This method is based on the thermoelectric analogy. A thermal network is created by linking the thermal resistances representing the machine elements. One of the most common commercial software highlighted within literature, also used in this project, is MotorCAD [29]. As the literature shows, this approach is widely used for the thermal analyses of electrical machines [27-31].

The network is constituted using thermal resistances, representing the motor components, and power sources representing the heat sources. The thermal resistances are evaluated from motor dimensions and material data [32] whereas heat sources, are evaluated separately and are manually implemented by the user.

The main strength of this technique is the calculation speed. Once the thermal network is generated, based on the machine design, output data such as temperatures within the machine, power flow, and thermal resistances are nearly instantaneously available. The limit of this technique is the prediction of the convective phenomena as complex fluid flow cannot be the resolved.

Detailed description of the theory behind this modelling technique is provided Appendix B.

### 2.4.2 Finite Elements Analysis

This numerical method is usually mainly used to investigate the electromagnetic aspects of the machines design. Some studies show that, for some applications, combined electromagnetic-thermal analyses were conducted with this method [33, 34].

This technique discretizes the model analysed into many elements. The heat transferred by conduction is evaluated through each cell; for this reason

prediction of the conduction phenomena can be very accurate also in geometrically complex areas such as electrical conductors. Due to its capability of accurately predicting losses and temperatures distribution, the finite elements analysis method can be used to improve the thermal networks based on the lumped-parameters method.

The main limit of this technique is that no flow field can be modelled, for this reason the evaluation of convective heat transfer is only based on assumptions made by the user. Another limit is that the process of the geometry discretization can is be very time consuming if large and complex domains are analysed. However, despite the limits described, the finite elements analysis method is an efficient technique of analysis which can potentially be integrated with other analysis methods.

### 2.4.3 Computational Fluid Dynamics

Computational fluid dynamics (CFD) is one of the most accurate numerical methods used to simulate and to predict fluid flow, heat transfer phenomena and chemical reactions by numerically solving set of governing mathematical equations such as conservation of mass, momentum, energy, and species [35].

Like the FEA method this technique can require a high computational cost. Significant effort is also required to properly setup the model and the time required to run the simulation can be long if complex cases are considered analysed. However with respect to the FEA method CFD is capable of resolving the fluid flow and can lead effectively predict the convective heat transfer phenomena but also it allows performing conjugate heat transfer analyses involving at the same time conduction, convection and radiation.

The CFD code used in this work is Fluent, software of the commercial package Ansys [36]. All CFD codes are generally constituted by the main following elements: pre-processor, solver and post-processor. In the pre-processor stage the computational domain is generated; it consists of the geometry of the region of interest, fluid, solid or both. The domain is then divided into sub-

domains and a mesh is created. Once the domain has been defined models and boundary conditions specified and the case can be solved; this represents the solver phase [35]. Finally when convergence is achieved data can be processed and analysed and this constitutes the post-processor stage.

This method has great potential but at the same time it presents many difficulties. For example, the discretization of the model into sub-domains is a very critical step of the setup process as the results strongly depend on how the mesh is generated in terms of elements type, elements size, elements number, quality, etc. Another aspect to consider is that, in order to obtain consistent results, the physics of fluid flows of the examined problems must be fully understood before the setup of the model. For this reason, there are no specific guidelines and every case must be considered singularly [35].

Detailed description of the theory behind CFD codes and the modelling of electrical machine are provided in Appendix C.

## 2.5 Cooling of High Speed Electrical Machines

During last decade high speed electrical machines have been employed for an increasing number of industrial applications such as power generation, turbo compressors, spindles, etc; that is mainly because of the higher power densities, efficiencies and reliability achievable [37-39] . However smaller sizes introduce significant challenges from the mechanical and thermal design point of view as stress and loss densities are higher.

Several cooling arrangements, indirect and direct, are commonly used in high speed electrical drives. The main difference between indirect and direct is that using an indirect cooling option primary coolant is not directly in contact with the machine inner components.

One of the most widely employed indirect methods is jacket cooling [40-42] . This generally consists of grooves, which may be axial or spiral, created in the machine housing, where a coolant can flow as shown in Figure 2.e; this

provides a compact solution as it does not require any external fin or fans. However the cooling of the rotor is not as effective as for the stator, so if significant losses occur in the rotor this option may be not appropriate.

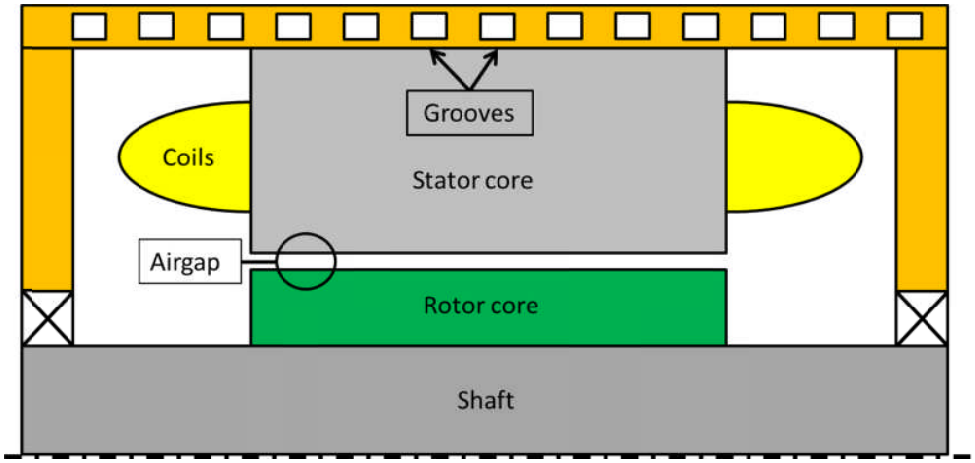



**Figure 2.e: Oil jacket cooling**

The main feature of direct cooling options is that the coolant wets all internal surfaces of the machine. Commonly used direct methods are Wet Rotor and Spray cooling.

Using the Wet Rotor method, the machine is flooded with coolant which flows from one side of the machine to the other passing through the air gap and this may guarantee good cooling of the whole machine as described in [43].

Spray cooling technique usually employs nozzles or in some cases a hollow shaft to spray the coolant at high pressure directly over the end-windings. This option may be more challenging from the manufacturing point of view due to high pressure nozzles and sealing issues; however it is experimentally demonstrated that very high convective heat transfer coefficients can be achieved [44].

Other cooling arrangements are presented in [45] where several configurations suitable for very high speed applications (up to 200,000 rpm); these are:

- Heat Pipes Made of Graphite Sheet: thin highly thermally conductive (k = 700 W/mK) with a thickness of 100 µm are located through the

stator lamination. Although this solution can significantly enhance the cooling of stationary components the assembly can be very complex; furthermore as graphite is also electrically conductive additional eddy losses can take place.

- Axial Ducts: several enclosed axial ducts are inserted through the stator lamination, particularly in the middle of stator teeth, allowing the coolant to flow through the machine.
- Annular Gap: an enclosed annular gap where the coolant flows is placed into the air-gap and attached to the stator inner diameter; this solution can enhance the cooling of the rotor although the coolant does not directly wet rotational components. The separation of the stator from the rotor is not a new solution, this was already described in [44] where a coolant is spayed over stationary components of a large and low speed machine and a sleeve was introduced into the air-gap to avoid the contamination of the rotor.

## 2.6 State of Art of Cooling Systems for aerospace starter generators

In Chapter 1 the importance of an effective thermal management of the aircraft electrical starter/generation system has been highlighted. The introduction of new design concepts such as More Electrical Aircraft (MEA) and More Electrical Engines (MEE) aiming to replace mechanical, hydraulic and pneumatic systems with electrically driven actuators, leads to an increasing demand of on board power [3]. Figure 2.f illustrates the growth of the on-board power demand during last 50 years.

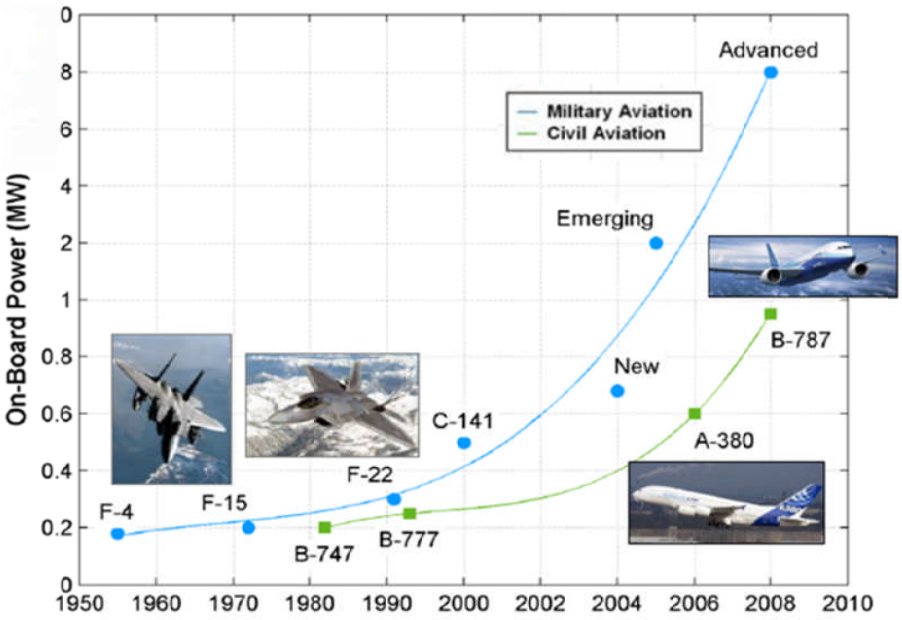



**Figure 2.f: Growth of On-Board Aircraft Power Demand [46]**

The significant growth of the power demand makes the problem of the thermal management even more challenging, as the amount of heat which must be removed can be considerable; for example assuming that each of the two generators in the Boeing 787 generates around 500 kW with an efficiency of 98%, the total losses which need to be dissipated is 10 kW. For this reason the traditional cooling systems require to be improved in order to achieve an effective cooling of the starter/generators.

Generally, electrical machines for aerospace applications are cooled using fluids available in flight: air, fuel and oil.

### 2.6.1 Air Cooling

Air cooling method usually requires ducts to let the air flow from the airframe to the generator, the air is scooped from the ambient surrounding the aircraft by some intake openings placed on the external surface of the aircraft. Figure 2.g illustrates the common displacement of the starter/generator and the cooling method described.

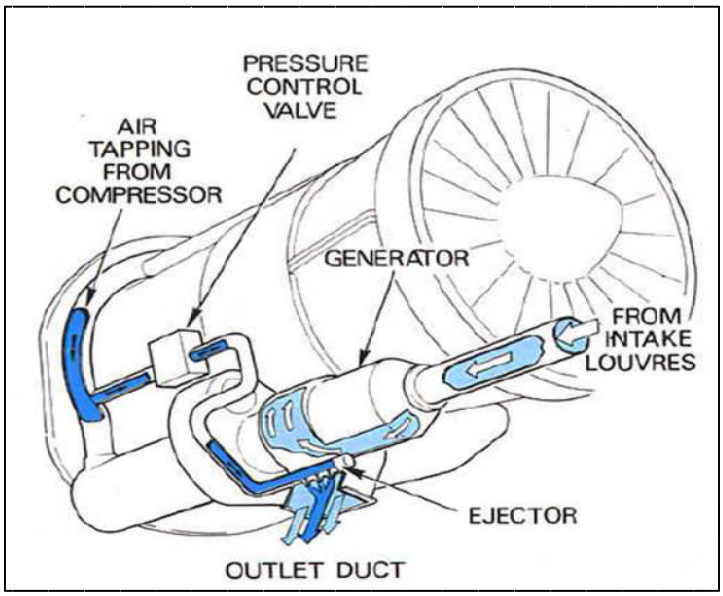



**Figure 2.g: Air Cooled Generator [47]**

Although air is largely available at low temperature around the aircraft during flight, some other aspects must be taken in consideration:

- **Low heat transfer coefficients**: as highlighted in section 2.2.2 air is not a good cooling medium as the achievable heat transfer coefficients cannot be high. Consequently, larger surfaces are needed to dissipate the heat and hence more mass to be carried.

- **Altitude**: at the high altitude the air density can be low and this negatively influences its cooling effectiveness [48, 49].

- **Aerodynamics**: air intake openings can affect the aerodynamics of the aircraft causing drag and hence, increasing the fuel consumption.

Table 2.4 shows the physical properties of standard atmosphere. Typical cruise altitudes for civil aircraft are highlighted.

| Altitude (m) | Temperature ( °C ) | Pressure ( Pa ) | Density ( Kg/m$^3$) | Viscosity (N-s/m$^2$ ) |
|---|---|---|---|---|
| 0 | 15.05 | 1.01e+05 | 1.225 | 1.79E-05 |
| 1000 | 8.55 | 8.99e+04 | 1.112 | 1.76E-05 |
| 2000 | 2.05 | 7.95e+04 | 1.007 | 1.73E-05 |
| 3000 | -4.45 | 7.01e+04 | 9.09E-01 | 1.69E-05 |
| 4000 | -10.95 | 6.17e+04 | 8.19E-01 | 1.66E-05 |
| 5000 | -17.45 | 5.41e+04 | 7.36E-01 | 1.63E-05 |
| 6000 | -23.95 | 4.72e+04 | 6.60E-01 | 1.60E-05 |
| 7000 | -30.45 | 4.11e+04 | 5.90E-01 | 1.56E-05 |
| 8000 | -36.95 | 3.57e+04 | 5.26E-01 | 1.53E-05 |
| 9000 | -43.45 | 3.08e+04 | 4.67E-01 | 1.49E-05 |
| **10000** | **-49.85** | **2.65e+04** | **4.14E-01** | **1.46E-05** |
| **15000** | **-56.45** | **1.21e+04** | **1.95E-01** | **1.42E-05** |
| 20000 | -56.45 | 5.53e+03 | 8.89E-02 | 1.42E-05 |
| 30000 | -46.65 | 1.20e+03 | 1.84E-02 | 1.48E-05 |
| 40000 | -22.75 | 2.87e+02 | 4.00E-03 | 1.60E-05 |
| 50000 | -2.45 | 7.98e+01 | 1.03E-03 | 1.70E-05 |

**Table 2.4: Standard Atmosphere [50]**

### 2.6.2 Fuel Cooling

Fuel is widely available during the cruise. The use of this fluid as medium cooling can be convenient for several reasons. Heating the fuel upstream of the

combustor can increase the engine efficiency, but it can also prevent from crystallization phenomena, as the freezing point of conventional fuels (Table 2.5 below) [51] is very close to the temperatures reached during the flight as shown in Table 2.4 above.

| Fuel | Freezing point (°C) | Auto-ignition temp. (°C) |
|---|---|---|
| Jet A | -40 | 210 |
| Jet A-1 | -47 | |
| Jet B | -50 | |

**Table 2.5: Specifications of Aviation Fuels**

Degradation of the fuel can occur if thermal limits are exceeded. As result of the oxidizing reactions some viscous deposits are formed and if they foul the heat exchange surfaces the cooling can be less effective [52].

### 2.6.3 Oil Cooling

Oil cooled generators for aircraft were first introduced during 50's and were employed for a military application (B-58) [53]. Oil is widely available in aircraft engines for lubrication of mechanical components such as gearboxes and engine bearings; as with fuel, high temperatures may lead to oxidation and the significant viscosity reduction can eventually affect the lubricating capability leading to mechanical failures, for this reason oil coolers are commonly available in all aircraft [52]. Figure 2.h illustrates a typical oil circuit of a jet engine, as can be seen air-oil and fuel-oil heat exchangers are integrated in the jet engine oil circuit. It should be also considered that due to the high values of Pr number, the oil should not be used at very low temperatures.

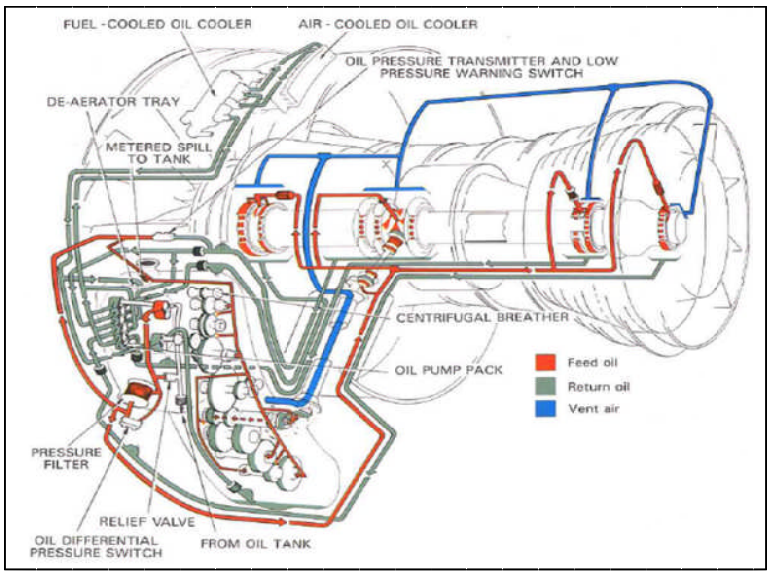



**Figure 2.h: Jet Engine Oil Circuit [47]**

One of the first studies which investigated the potentialities of using oil to cool an aircraft starter/generator, was conducted in 1970 [53]. Here the advantages of using oil rather than air are highlighted and description of direct and indirect oil cooling systems is conducted. It is also shown that oil cooling can bring considerable benefits in terms of weight reduction of the generator.

Table 2.6 summarise the advantages and the disadvantages that the use of mentioned fluids imply.

| **Fluid** | **Advantages** | **Disadvantages** |
|---|---|---|
| Air | - available at low temperatures during cruise | - limited effectiveness<br>- larger heat exchange surfaces required<br>- aerodynamics issues |
| Fuel | - available in flight<br>- higher *h* values than air<br>- leads to compact cooling systems<br>- benefit for engine efficiency | - temperature limited |
| Oil | - available in flight<br>- higher *h* values than air<br>- leads to compact cooling systems | - temperature limited<br>- oil cooler required |

**Table 2.6: Summary of In-Flight Cooling Methods**

The opinion of the author is that, oil cooling can be the optimal solution between those described because in addition to the advantages listed in Table 2.6 oil can be used to pre-heat the fuel in order to obtain the benefits described in section 2.6.2.

## 2.7 Summary

Nowadays the thermal management of electrical machines represents a key step of the design process. Indeed due to the increasing demand of high power, high reliability and efficiency a critical analysis of the thermal aspects related to the electrical machines is required; this can lead to a detailed understanding of the heat power released by each machine component and hence to the selection of an appropriate cooling strategy.

Wide range of cooling techniques is currently employed for high speed machines and integration of the systems reviewed can lead to design a novel and efficient cooling option. The identification of an optimal cooling configuration, however, strongly depends on the machine type and design; as a permanent magnet machine is analysed in this work the majority of losses are expected into stationary components and particularly in windings. Using direct liquid cooling options the machine efficiency and density can be significantly improved due to the reduction of temperature dependent resistive losses. Flooding the machine can lead to very high heat transfer coefficients and hence intensive cooling, however for a high speed application this can also lead to very high friction loss and this may negatively affect the overall efficiency; a partially flooded machine, as will be discussed in Chapter 3 can be employed instead.

Several modelling strategies based on analytical and numerical approaches are available for investigating machines thermal behaviour; as each approach presents own pros and cons their combined use can lead to develop accurate thermal models. The lumped parameter thermal network is optimal for initial analysis allowing to quickly investigate different scenarios (e.g. different

materials employed, different losses distribution, different cooling arrangements). The use of CFD instead is needed primarily for fluid flow investigations and prediction of heat transfer coefficients.

# 3 Cooling strategy identification

## 3.1 Introduction

Chapter 2 provided a detailed description of the thermal phenomena related to the electrical machines and the state of the art of the cooling strategies commonly employed in existing applications. This information, together with the project requirements led to the development of a novel cooling design concept for the Synchronous Interior Permanent Magnet Machine selected. The description of the concept and of its main features is object of the following chapter.

## 3.2 Design Criteria

As seen in Chapter 2 several cooling techniques are currently available for the cooling of aircraft starter generators and different coolants may be employed. However, the following aspects should be accounted for when designing an optimised cooling system for a starter generator:

- *Effectiveness*: Intensive cooling can lead to improve the overall machine efficiency by reducing the temperature dependent losses such as copper losses.

- *Reliability:* High temperatures might accelerate the aging of some components, reducing their lifetime; hence operating at low temperatures can increase the overall reliability of the machine. As example, a temperature rise of 10°C can reduce the winding insulation life by around the 50% [4].

- *Reduction of size and weight*: Especially in aerospace applications, size and weight are significantly important factors to be taken into account, having a direct impact on the fuel consumption and hence $CO_2$ emissions.

• *Coolant selection*: The fluid used must lead to the achievement of the goals listed above but also it should not represent an additional load to be carried by the aircraft.

Liquid cooling techniques may generally lead to more compact designs than air cooled machines as described in Chapter 2; project requirements and the availability of oil on board, for engine lubrication purposes [54], suggested a move towards an oil cooling solution.

## 3.3 Design Selection

In the first stage of the machine design, some conventional direct and indirect cooling options described in section 2.5 – 2.6 were considered; this allowed investigating the performance of the existing liquid cooling techniques applied to the starter/generator designed.

As described, direct liquid cooling methods may be very effective due to intensive cooling; however, for high speed applications there are some other considerations. Windage losses are directly proportional to the fluid viscosity and to the cube of the rotational speed; therefore significant viscous heat may be generated in the air-gap increasing the power loss, for instance assuming an airgap 1 mm wide and a rotational speed of 30,000 rpm more than 20 kW of friction loss is generated; for this reason these cooling techniques may be not appropriate. Indeed, in high speed machines, liquid must be avoided in the air-gap at all times.

Therefore having identified that for an effective and intensive cooling, a direct cooling approach was required a practical alternative (Wet Stator) was developed and implemented into the machine. This design could guarantee an intensive direct cooling of the machine but at the same time could prevent any liquid from entering the air gap by introducing a stator sleeve to isolate the stator from the rotor across the air gap as shown in Figure 3.a. This could be possible due to the wide air-gap (2 mm). Once the coolant enters into the stator chamber, it flows through the stator region in two rows of axial ducts created

through the stator laminations, one along the stator inner diameter, the other along the stator outer diameter.

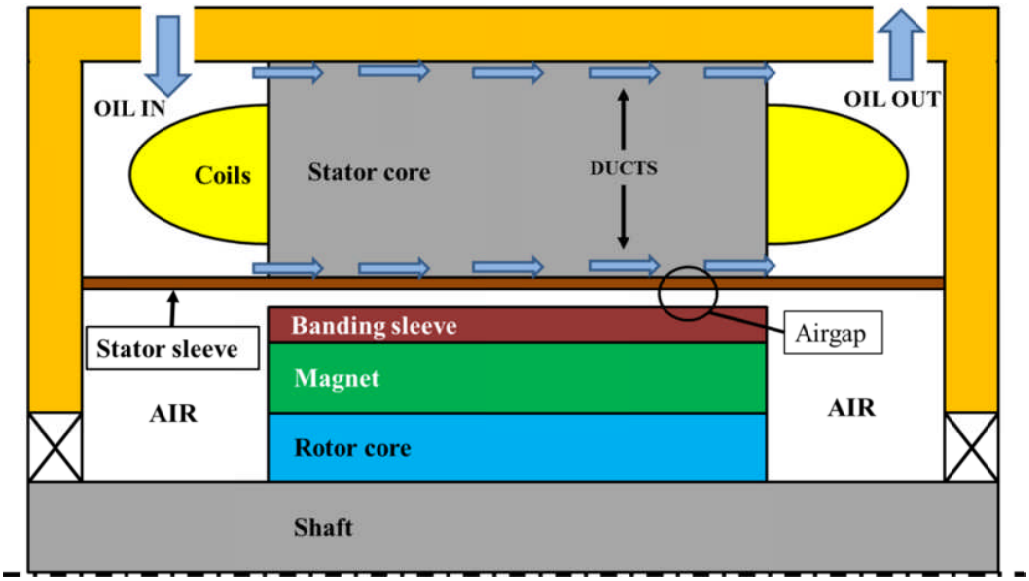



**Figure 3.a: Wet Stator cooling**

The inner ducts are constituted by the spaces between stator teeth. In order to get an even distribution of the coolant both inner and outer layer of ducts were given the same cross sectional area overall; the radial section, in Figure 3.b, shows the ducts arrangement.

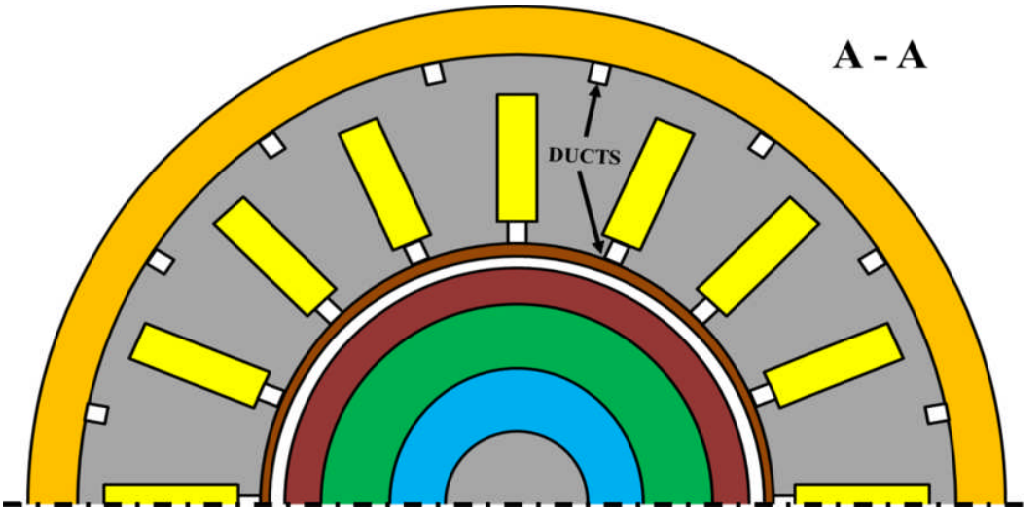



**Figure 3.b: Wet Stator radial section**

Despite no oil entering the rotor region, the lower overall temperatures achievable in the stator may represent a significant benefit for the rotor components in terms of cooling.

As the generator is a permanent magnet machine it is expected that around 80% of losses would occur in the stationary components [55]; flooding the stator can then help to dissipate most of these losses and improve the machine efficiency by reducing the temperature dependent losses.

## 3.4 Design Features

Having identified the concept, as described in the previous section, there were detail design considerations that required development. These were the:

- Stator sleeve
- Oil entry region
- Axial ducts and Flow deflector

and are described in the following sections

### 3.4.1 Stator Sleeve

As mentioned above, the main function of the stator sleeve is to literally separate the machine into two separate chambers so preventing any oil from wetting the rotational components. An electrically non-conductive material was selected in order to avoid further power losses which would be caused by eddy currents induced by the rotating magnets, hence by the variation of the magnetic field. The sleeve is 1 mm thick, the outer diameter is equal to the stator core bore (96 mm) and the total length is 146.5 mm.

The stator sleeve was manufactured to ensure a smooth internal surface; this will help to further reduce the machine losses as a smooth and slotless stator surface can lead to a reduction of the windage up to the 25% [26].

The determination of the sleeve thickness has required a balancing of design needs. First, a thinner sleeve would means the airgap would be wider so the

viscous heat generated is lower; however, a thickness lower than 1mm could not be achieved due to manufacturing limitations. By using a 1 mm thick sleeve the machine initial airgap is reduced from 2 mm to 1mm, this causes an increase of the friction loss by approximately 10%.

In addition the maximum pressure that the stator sleeve is capable of withstanding had to be calculated to ensure there was no failure. The radius of the cylinder (48 mm) more than ten times larger than its thickness (1mm), the case can be analysed as a thin-walled cylinder with closed ends and with uniform external pressure applied. Knowing the geometry and the mechanical properties of the material, the maximum buckling pressure can be estimated using Equation 3.1.

$$-P_e = 0.807\, E\delta^2/lr \sqrt[4]{(1/(1-v^2))^3\, \delta^2/r^2} \qquad 3.1$$

Where $E$ is the Young's modulus, $v$ is the Poisson ratio and $l$. $r$ and $\delta$ are the length, thickness and radius of the sleeve.

The mechanical properties of the fiberglass composites are strongly affected by the composition of their components [56]. The sleeve manufactured has a fibre volume fraction of 58% and 42% of epoxy. Having used material properties of a fibre glass with a volume fraction of 50% it is expected that the sleeve manufactured can withstand at least 4 bar gauge. This pressure was considered sufficient as the oil pressure required was 2 bar gauge as maximum.

The outer surface of the sleeve is in contact with the lamination inner diameter. In order to ease the assembly process one edge of the stator sleeve is glued to the flange at the non-drive end of the machine, whilst the other edge seats on an aluminium ring inserted into a groove made on the flange at the drive end. The sealing is guaranteed by two O-rings; Figure 3.c and Figure 3.d show the connection at the non-drive end and drive end respectively.

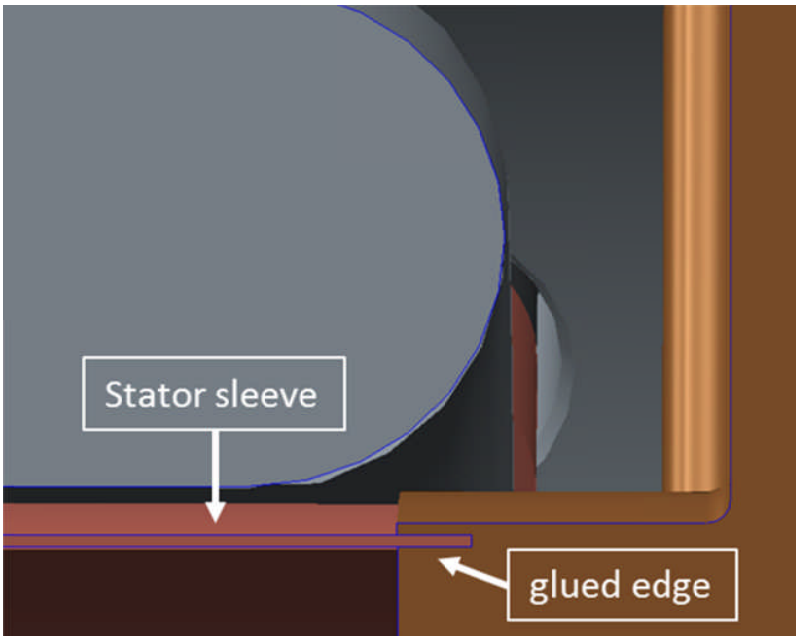



**Figure 3.c: Stator sleeve connection at non-drive end**

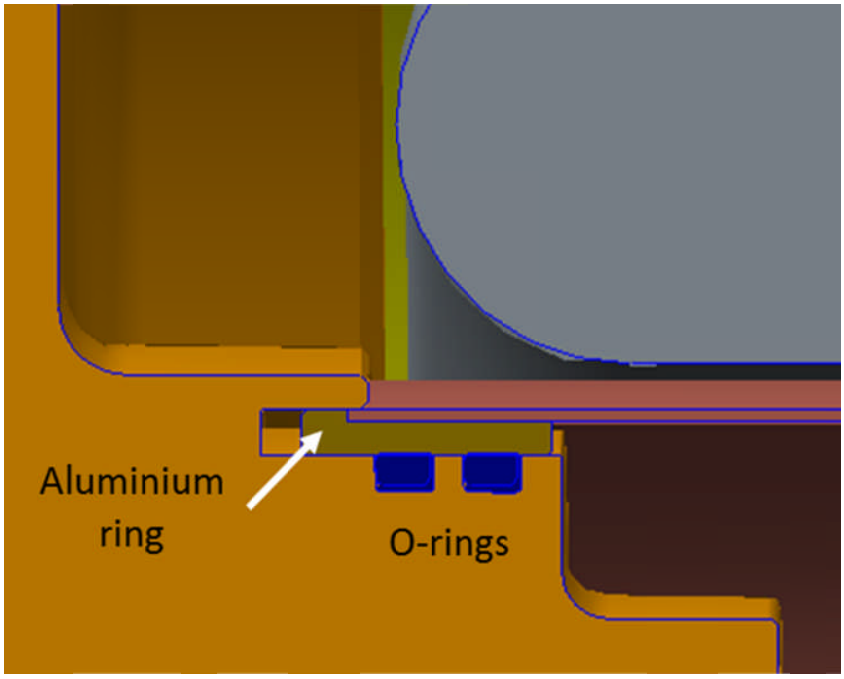



**Figure 3.d: Stator sleeve connection at drive end**

Some gap between the aluminum ring and the flange was also left to accommodate any axial movement which could eventually occur due to thermal expansion and could compromise the stator sleeve integrity.

With this configuration the sleeve can effectively separate the stator from the rotor as shown in Figure 3.e.

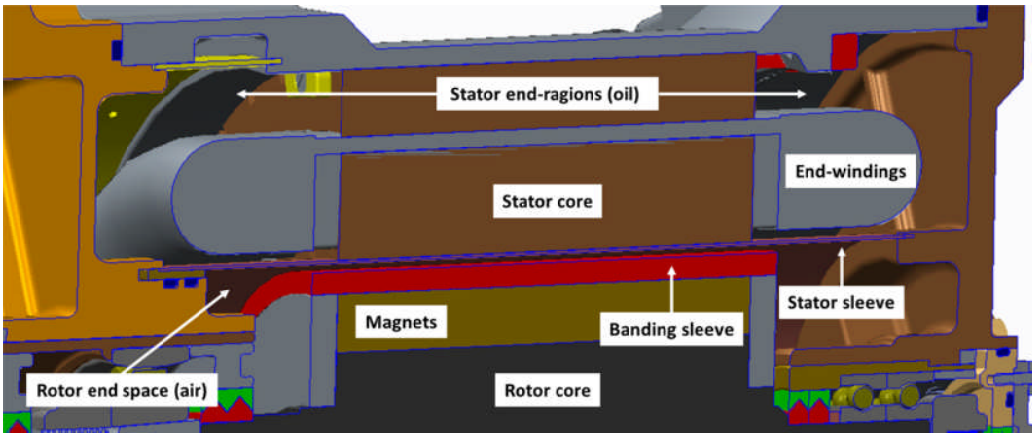



**Figure 3.e: Cross-section highlighting the location of the stator sleeve**

### 3.4.2 Oil Entry Region

Within the stator region an oil inlet was required. The design criteria followed for the entry region were essentially feasibility, reliability and effectiveness; this aimed to identify a simple solution able to maximise the cooling capabilities.

As mentioned previously several direct liquid cooling strategies are commonly available, some employ high pressure nozzles [44] and others rely on the rotation of the shaft for impinging the coolant directly over the end-windings [57].

For this machine the use of high pressure nozzle would firstly lead to a more complicated design, perhaps more importantly as they would require more space leading to a larger and hence heavier design.

According the project specifications from research partner one single oil distribution line needs to be used and this should be connected to the flanged side of the machine, which in this case is the drive end as shown in Figure 3.f.

The flange has an outer diameter of 238 mm and the inlet center is located at a radius of 100 mm from the machine axis and an angle of 45° with the respect of the vertical axis of the flange.

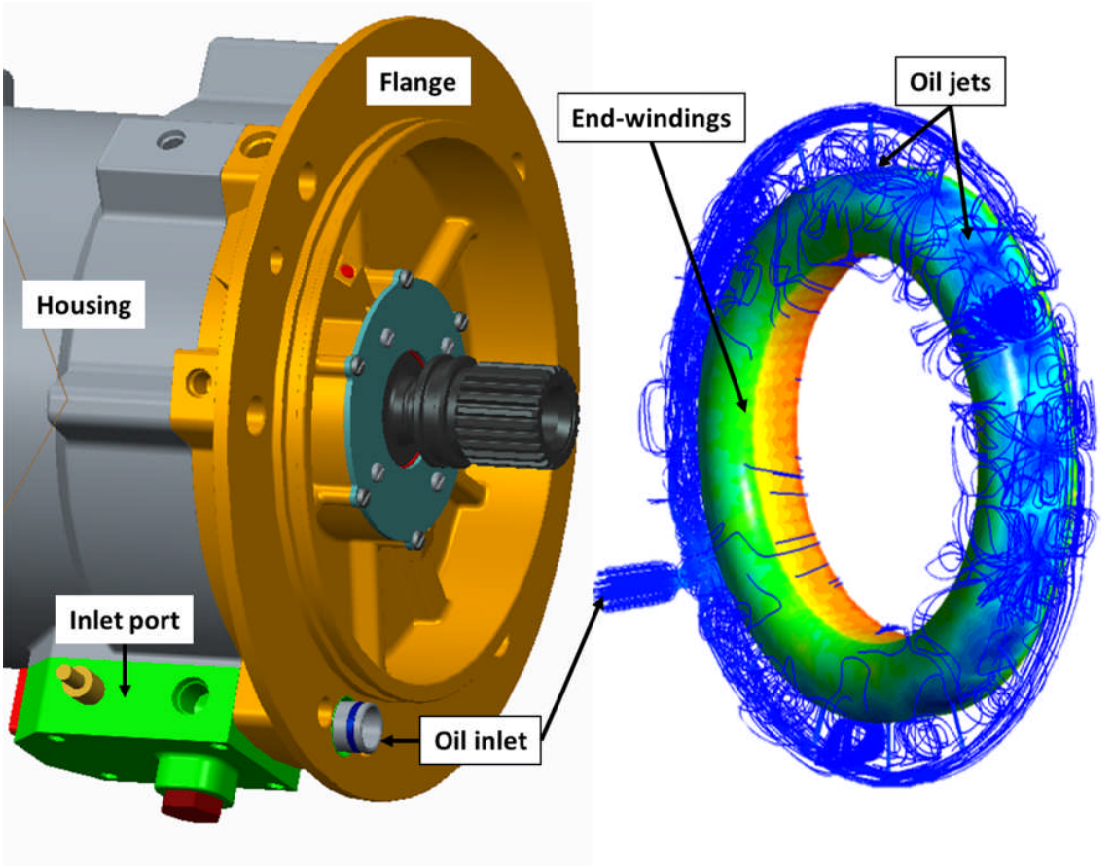



**Figure 3.f: Main oil inlet**

A set of radial openings is used to directly impinge the oil over the end-windings in order to enhance the cooling, hence increasing the heat transfer coefficient over end-windings. The oil coming from the flange flows inside an oil gallery and is then impinged uniformly over the end-windings. The section view in Figure 3.g shows the oil path in the entry region through the inlet port.

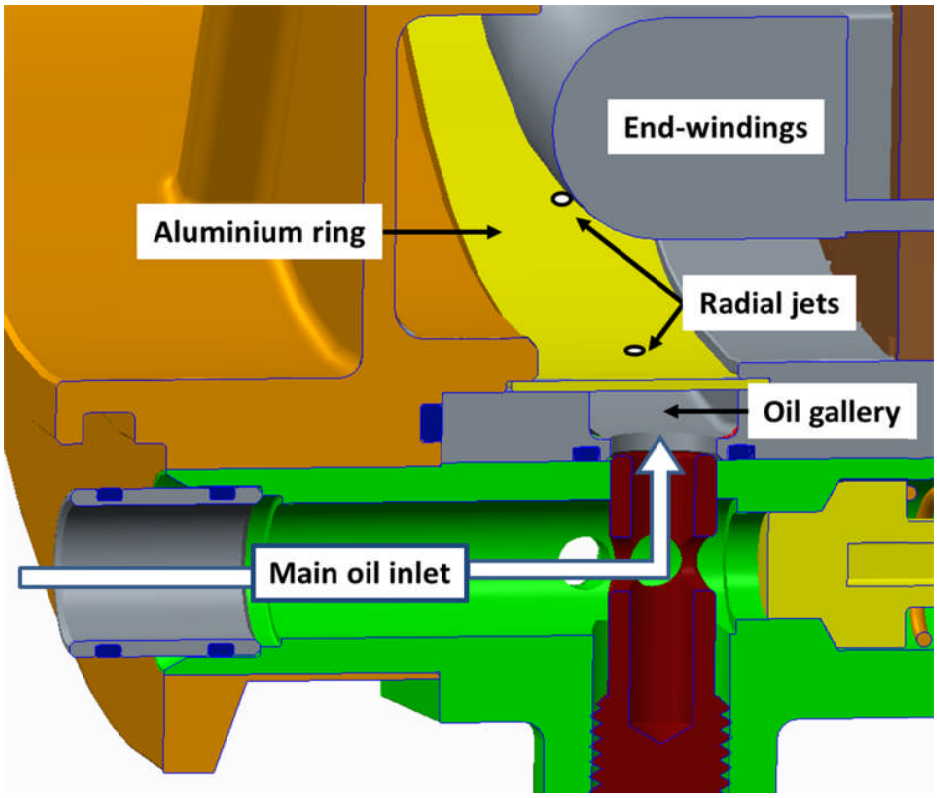



**Figure 3.g: Inlet oil path**

An aluminum alloy short cylinder was drilled with 18 holes of 1.5 mm diameter evenly spaced at intervals of 20° to act as radial openings to let the oil in; the cylinder has a radius of 1 mm thick, has a diameter of 167 mm and a length of 24.5 mm. It is located between the flange and the housing as shown in Figure 3.g. Being easily removable, the ring can be eventually replaced and alternative configurations can be used. The entry region is the object of more detailed numerical study described in Chapter 5.

### 3.4.3 Axial Ducts and Flow Deflector

In the majority of Permanent Magnet Machines 80% of the losses are generated in the stator and particularly in the windings [55]. The presence of some hot of spots within coils can severely damage the windings integrity then leading to major failures; therefore removing the heat out of the slots effectively is a priority.

As a result of the electromagnetic design a stator with 36 slots was selected. The slots are almost entirely filled with coils and insulation, with the remaining space between the teeth resulting in a 2 mm side square slot along the stator inner diameter. For an even temperature distribution an additional row of axial ducts were created through the laminations along the stator outer diameter; also to get an equal distribution of the coolant the number and cross-sectional area of the outer ducts were the same as the inner ducts. Figure 3.h shows the resulting stator design, where the inner and outer ducts rows are highlighted; for more clear visualization end-windings are not shown.

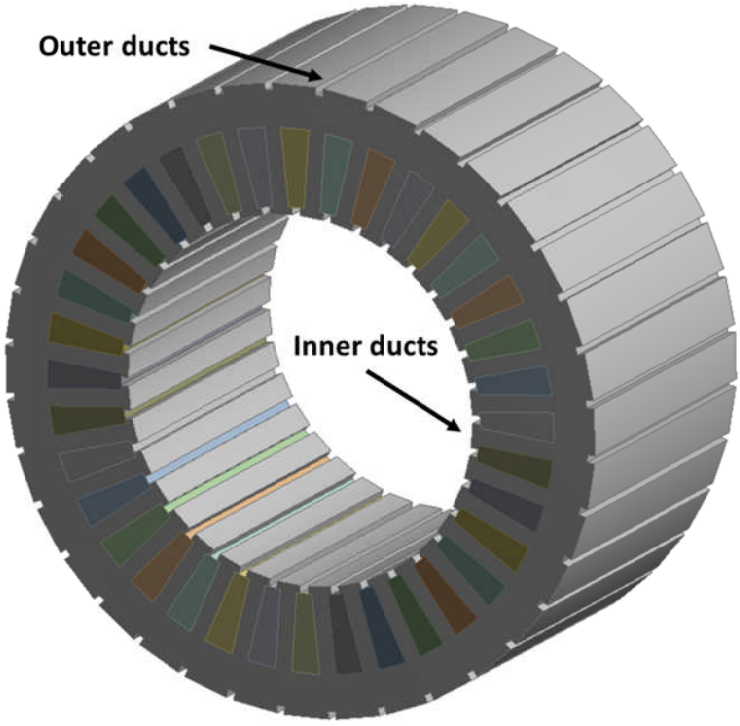



**Figure 3.h: Stator design**

The configuration described was also designed for an enhanced cooling of the end-windings at the non-drive end. A flow deflector located at the exit of the axial ducts directs the coolant over the outer surface of the end-windings as shown in Figure 3.i. Following some numerical investigations, which will be described in Chapter 5, a 5mm radial depth deflector having an angle of about 60° facing the flow was identified as an optimal configuration. In order to

simplify the overall design of the machine the deflector was designed as part of the housing.

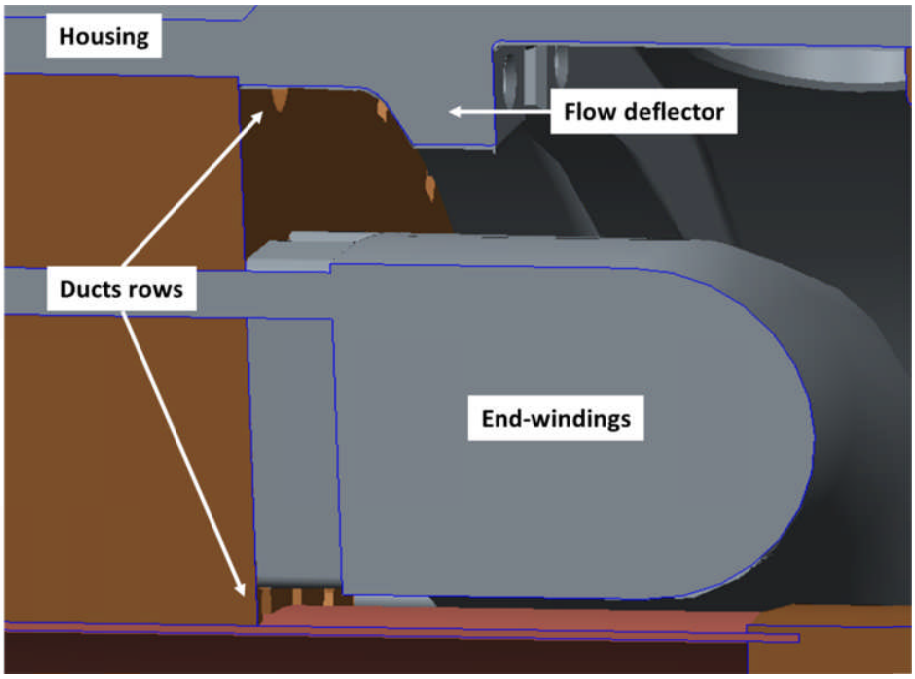



**Figure 3.i: Flow deflector**

According project specification a 15 mm oil outlet was located at the bottom of the housing on the non-drive end side of the machine

## 3.5 Summary

An investigation of existing liquid cooling techniques was conducted. Based on the machine electromagnetic design and requirements an alternative cooling strategy was identified and the main features described embodied as a concept. Thermal management of the machine is achieved by direct oil cooling. The main idea was to flood the stator region by using a retaining stator sleeve. Ducts through the stator core along the stator outer diameter and slots along the inner diameter let the oil flow through the machine. Such an arrangement can provide an even distribution of the coolant. Analytical and numerical analysis are required to investigate the behaviour of the cooling strategy adopted. These are described in Chapters 4 and 5.

# 4 Machine Analytical Thermal Modelling

## 4.1 Introduction

Chapter 3 provided a description of the cooling configuration developed. In order to predict the thermal behaviour of the starter generator and the performance of the cooling strategy adopted, an analytical modelling technique, based on a lumped parameter thermal network was used and is described in this chapter. Information regarding the theory behind this modelling method and the equations used provided in Appendix B.

## 4.2 Design Strategy

The commercial packages employed to analyse the thermal networks were MotorCAD and Simulink. MotorCAD, was used in the early stages of design process to investigate the thermal behaviour of initial machine designs and the performance of cooling strategies already available in that software.

However, the lumped parameters method is not fully capable of predicting all aspects of the fluid flow and the convective phenomena; for this reason, some critical areas of the machine such as the end regions, the axial ducts and the airgap were investigated using CFD. By importing some numerical data into MotorCAD from the CFD models the thermal network could be improved.

Other key areas which required detailed modelling were the bearing chambers. Due to the complexity of these regions, a thermal network was developed by the author using Simulink and the heat transfer phenomena investigated.

Diagram shown in Figure 4.a illustrates the general modelling algorithm followed.

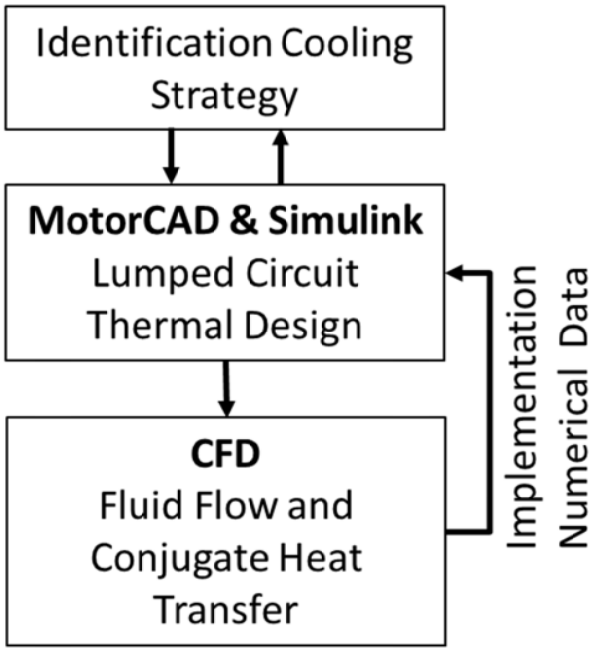



**Figure 4.a: Modelling Flow Diagram**

## 4.3 Machine Thermal Modelling using MotorCAD

MotorCAD is an analytical modelling technique based on the lumped parameters method. In order to obtain the equivalent thermal network of the electrical machine under consideration few key steps need to be followed:

- Machine geometry definition.
- Definition boundary conditions and material properties.
- Cooling method implementation.
- Generation Thermal network.

### 4.3.1 Machine Geometry

A wide range of machine type models is available in the MotorCAD built in library. Once the desired machine type is selected all the axial and radial dimensions are defined by using the 2D modelling panel shown in Figure 4.b and Figure 4.c.

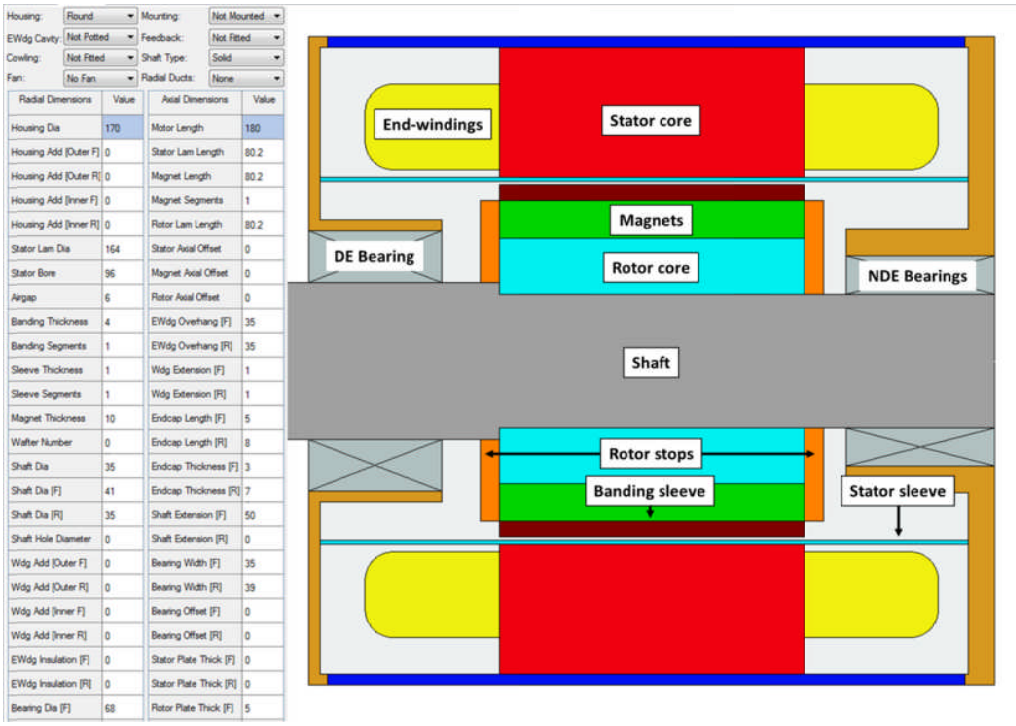



**Figure 4.b: Machine Geometry Creation - Axial Dimensions**

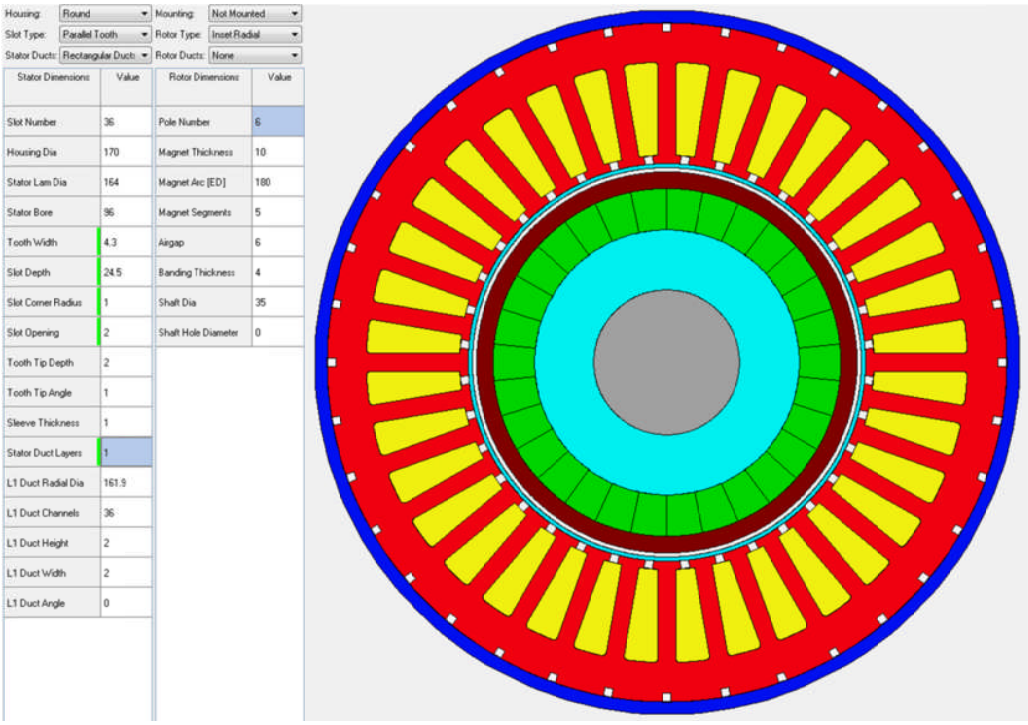



**Figure 4.c: Machine Geometry Creation - Radial dimensions**

An accurate definition of all dimensions is required for the correct estimation of the thermal resistances.

The software also allows the definition of the winding slots; this includes the wires type, wires size and packing factor as can be seen in the panel in Figure 4.d.

As the stator windings are a key component of electrical machines, both from electromagnetic and thermal point of view, a precise model of the slots is required; this allows a more accurate estimation of the temperatures distribution and hence the identification of eventual hot-spots.

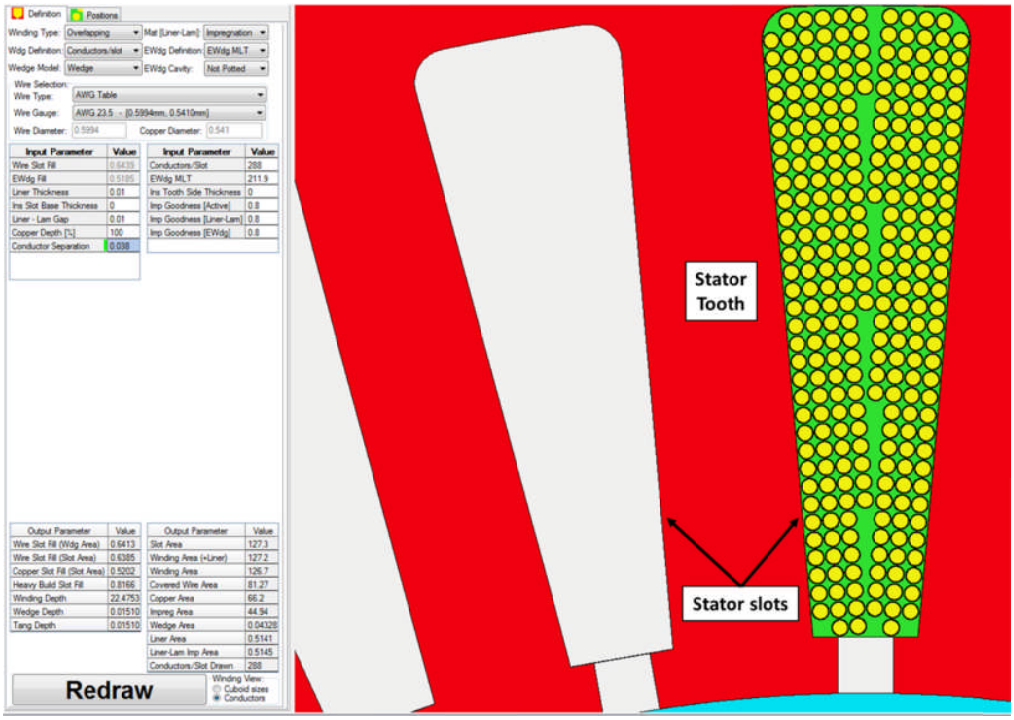



**Figure 4.d: Creation of Stator Windings**

In the actual design litz wires (consisting of many thin wire strands, individually insulated and twisted together) of 0.6 mm diameter were used to create windings, 144 conductors were used per coil and two 2 coils were fitted inside every slot; the remaining air gaps were filled with varnish, a protective hard film.

### 4.3.2 Definition of Boundary Conditions and Materials Properties

Once the geometry is defined, material properties can be assigned to each machine component.

A wide choice of materials can be selected from the software's library, however for an appropriate estimation of the thermal resistances, user defined properties can be implemented.

Due to the non-homogenous nature of some components/areas such as bearings chambers, stator sleeve, and windings the determination of the overall material properties has required further investigations.

The cuboidal model was utilised to determine the thermal conductivity along all directions based on the conductors location, wires size and slot fill used in the design. Other properties such as density and heat capacity were based on experimental data shown in [58] where some winding samples having similar packing factor to the current design were tested.

The thermal conductivity of the fibre glass stator sleeve was provided by the manufacturer, whilst values of density and heat capacity refer to typical data available for laminate with fibre volume fraction of about 60%.

As bearing chambers were constituted by several components overall material properties such as density, heat capacity and thermal conductivity were determined, these are described in details in section 4.4.4.

Therefore the following properties, shown in Table 4.1, were assigned to the machine's components.

| Component | Material | Density, ρ ($kg/m^3$) | Heat capacity, Cp (J/Kg K) | Conductivity, k (W/mK) |
|---|---|---|---|---|
| Case | Aluminium 6160 | 2700 | 1400 | 167 |
| Stator core | Steel JNHF | 7800 | 460 | 19 |
| Windings | Copper and Insulation | 5000 | 1300 | 0.71 (x), 0.71 (y), 229(z), |
| Stator sleeve | Glass fibre | 1900 | 900 | 0.86 |
| Banding sleeve | E-Carbon fibre | 1600 | 750 | 35 |
| Magnets | Samarium Cobalt | 8300 | 1400 | 11.6 |
| Rotor stops | Aluminium 6160 | 2700 | 1400 | 167 |
| Rotor steel | 17-4 PH | 7800 | 460 | 17.9 |
| Shaft steel | 17-4 PH | 7800 | 460 | 17.9 |
| Bearing Drive End | N/A | 2973 | 689 | 3 |
| Bearing Non-Drive End | N/A | 3394 | 613 | 3 |

**Table 4.1: Employed materials**

The next step is to establish the heat inputs representing the electromagnetic and mechanical losses occurring within the electrical machine. Being a thermal package, MotorCad is incapable of automatically computing any power loss related to the electromagnetic functioning of the machines; for that reason these type of losses were provided by the team of electrical designers who estimated them numerically by using the Ansys electromagnetic package (Ansys Maxwell) and were then manually implemented into MotorCad. Mechanical power losses, such as windage and bearings friction were

calculated by using correlations described section 2.3.4 and Appendix B.2 respectively. Throughout the design process, the machine operating condition at which the highest power losses were expected was considered (at 32,000 rpm). Table 4.2 lists the estimated losses.

| **Source** | **Power loss (W)** |
|---|---|
| Windings | 1195 (at 180°C) |
| Stator core | 293 |
| Airgap (windage) | 94 |
| Magnets | 51 |
| Rotor core | 9 |
| Bearing Drive End | 100 |
| Bearings Non-Drive End | 180 |
| **Total** | 1,922 |

**Table 4.2: Machine losses at 32,000 rpm**

As shown rotor losses are significantly lower than those generated into the stationary components, representing the 23% only of the total losses; this confirms the expectation that usually 80% of losses in permanent magnet machines occur in the stationary components, as stated in section 3.3.

### 4.3.3 Cooling Method Implementation

When all material properties and the heat sources are defined, the thermal behaviour of the machine and the cooling capability of the cooling strategy adopted could be investigated.

Wide choice of cooling methods is available in MotorCad. However as a result of the collaboration between the author and the software developer a new cooling configuration was developed, an option called Through Ventilation is adopted. This option can simulate a fluid flowing through the machine particularly through the stator region only.

Once the cooling option was enabled the properties of the operating fluid were defined. The coolant employed is a synthetic lubricating oil MIL-PRF-7808 as recommended by the company sponsoring the project; its properties are listed in Table 4.3

| Parameter | Value |
|---|---|
| Density (kg/m$^3$) | 951 |
| Dynamic viscosity at 40°/100° C (kg/ms) | 0.011/0.003 |
| Heat capacity (J/kgK) | 2,300 |
| Thermal conductivity (W/mK) | 0.13 |

**Table 4.3: Oil properties**

A flow rate of 15 liters per minute was assumed based on the provided specifications. As the maximum expected temperature rise of the oil, was around 5 degrees (if 100% of losses are dissipated by the oil), thermal properties were assumed to be constant.

One of the main weaknesses of the lumped parameters network technique is the prediction of the fluid flow; hence the estimation of convective coefficients relies only on empirical correlations described in appendix B.1. In practice the geometry inside electrical machines may be quite irregular, especially around end-windings, and correlations might not be capable of catching some important aspects of the fluid flow.

A data input editor available in MotorCad allows the manual implementation of the convective heat transfer coefficients over all machine internal surfaces; for this reason CFD numerical investigation of some areas such as end spaces and stator ducts were carried out and data were implemented into MotorCAD. Figure 4.e shows the end-winding surfaces where numerical data were implemented whilst Table 4.4 shows the numerical data imported. This will be discussed in more detail in Chapter 5.

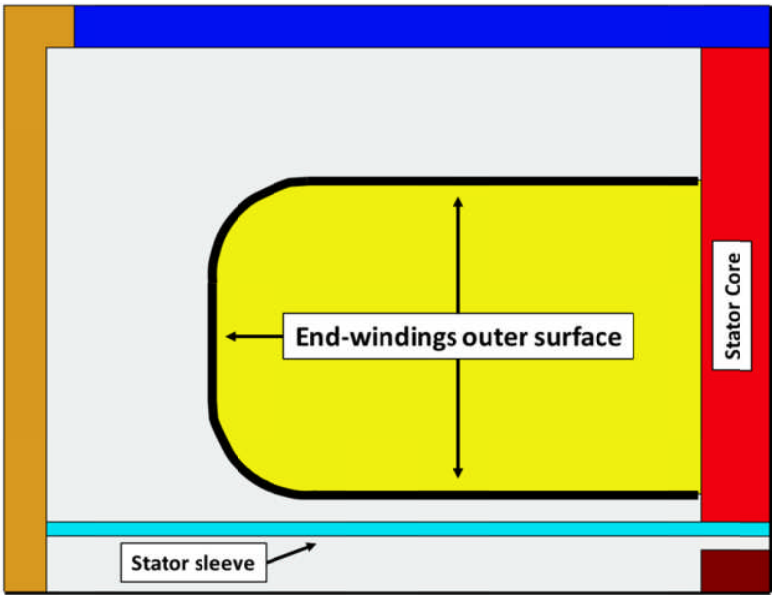



**Figure 4.e: Stator End-Space**

| **Surface** | **Heat transfer coefficient *h* (W/m$^2$K)** |
|---|---|
| Drive End end-windings | 1500 |
| Non-Drive End end-windings | 1200 |
| Stator ducts | 900 |

**Table 4.4: Numerical data implemented**

In order to evaluate the benefit obtained, in terms of efficiency, for adopting the Wet Stator cooling strategy, a conventional spiral Oil Jacket, shown in Figure 2.e cooling was investigated for the same machine design; giving an indication of how the temperature distribution inside the machine differs in the two cases.

The software is also capable of accounting for the copper losses dependency on the temperature by scaling the resistive losses to the operating average winding temperature; this quantifies how the efficiency varies when adopting different cooling strategies. The loss scaling is carried out determining the current in the phases first, according to Equation 2.4 knowing the electrical resistance of the coils and the power loss which was estimated assuming a windings temperature of 180°C is calculated, then the value of the electrical

resistance is scaled using Equation 2.5 and finally, using the same current, the scaled copper losses can be calculated.

### 4.3.4 Generation Machine Thermal Network

Having established all thermal inputs, material properties and boundary conditions it is possible, within MotorCad, to generate a colour coded thermal network where each colour represents a component as shown in Figure 4.c. The network can also provide information about the value of thermal resistances, nodal temperatures and power flowing through the resistances, allowing a clear understanding of the thermal paths and hence of how the heat is dissipated, Figure 4.f shows the resulting thermal network generated by MotorCAD based on the setup described. Table 4.5 lists the input data applied at the nodes.

| **Node** | **Input parameter** |
|---|---|
| TV EWdg (Oil inlet) | 120°C |
| Ambient | 35°C |
| EWdg (End-Windings) | 25% Copper loss (each) |
| Winding | 50% Copper loss |
| Tooth (teeth) | 70% Stator Core loss |
| Stator yoke (back iron) | 30% Stator Core loss |
| Sleeve, Rotor Surface (airgap) | 50% Windage (each) |
| Rotor Lam (rotor core) | 100% Rotor core |
| Magnet | 100% Magnet loss |
| Bearing[F] – Drive End | DE bearing loss deducted of 30W |
| Bearing[R] – Non-Drive End | NDE bearing loss deducted of 90W |

**Table 4.5: Nodes input data**

The power loss deduction applied to the bearings was included to account for the cooling effect of the lubricating oil; this was calculated developing a thermal network of bearing chambers which is described in section 4.4. As bearings are not sufficiently modelled in details in MotorCad a full thermal network of the bearing chambers was developed in Simulink to investigate the heat transfer. This is described in section 4.4.

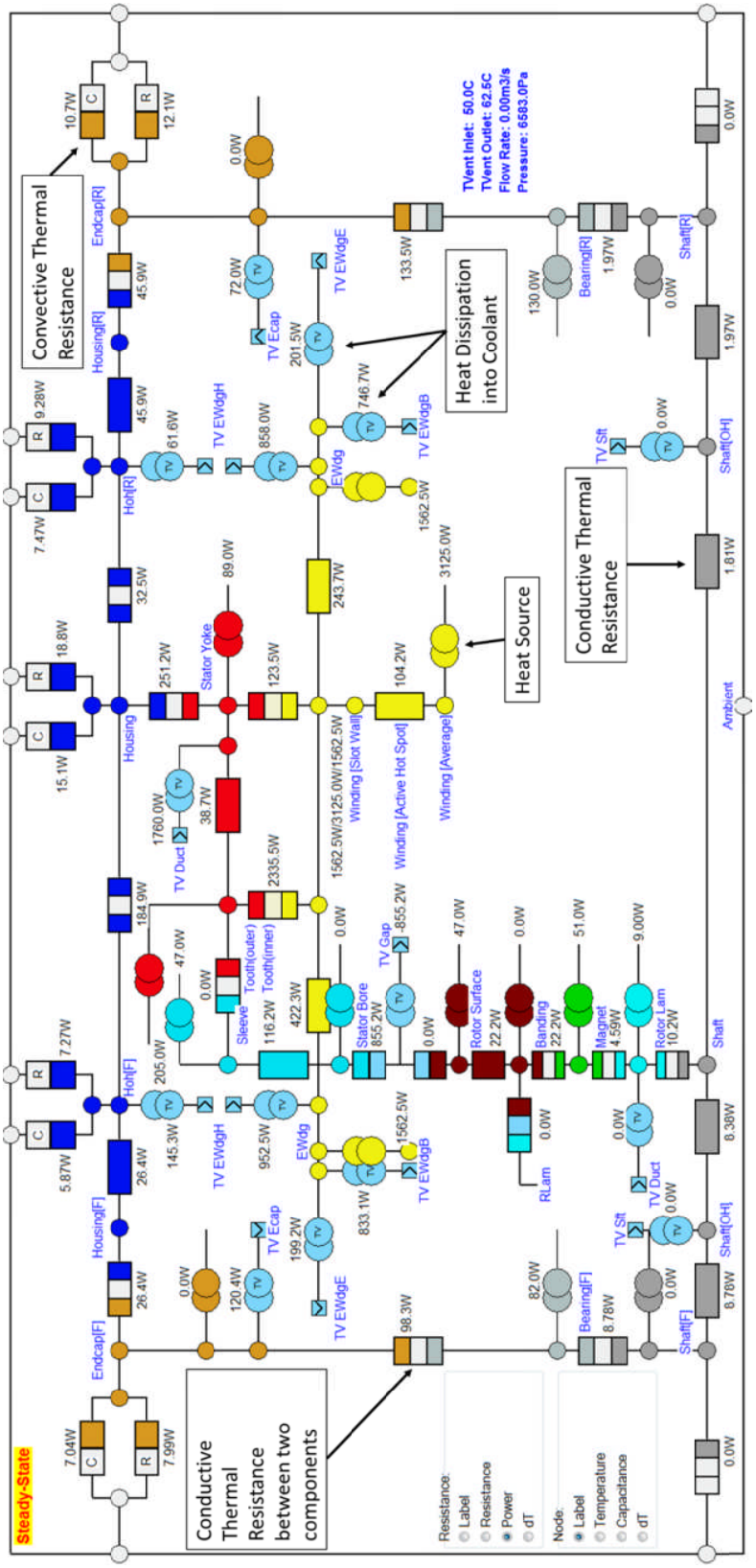



**Figure 4.f: MotorCAD thermal network of machine designed**

## 4.4 Thermal Modelling of Bearing Chambers

In the design process of rotating machinery, especially for high speed applications, a detailed understanding of thermofluidynamics phenomena related to bearings can lead to more reliable and efficient designs. However many factors can affect the performance of bearings; heat generation due to friction of the rotating elements varies significantly with speed, loads, type of lubricant used and amount of lubricant employed [59].

The machine designed employs two different types of bearings manufactured by SKF, a cylindrical roller bearing at the drive end and two paired angular contact ball bearings with back to back configuration at the non-drive end side, Figure 4.g a and b show the bearings used, dimensions are also provided in Table 4.6.

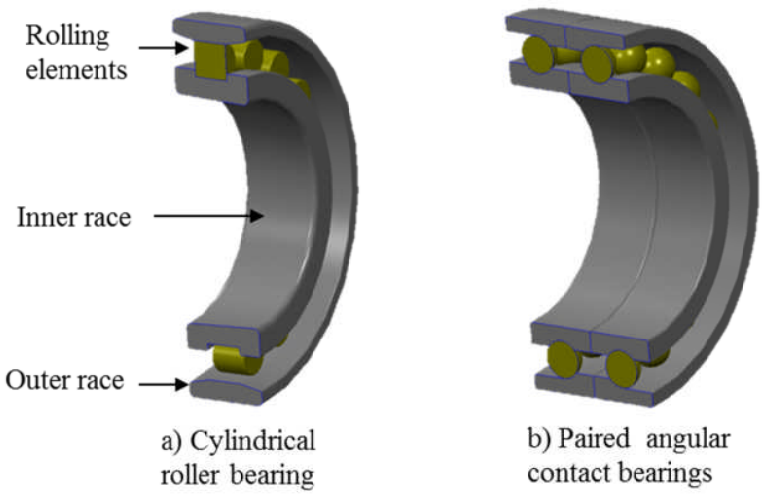



**Figure 4.g: Cross-sectional view of bearings used**

| Bearing type | Code | Inner diameter | Width | Height |
|---|---|---|---|---|
| Cylindrical roller | N1008 KPHA | 40 mm | 15 mm | 14 mm |
| Angular contact | 71906 CD | 30 mm | 9 mm | 8.5 mm |

**Table 4.6: Bearing dimensions**

Bearings are oil lubricated and, in order to prevent the oil from flooding the machine rotor and from leaking out labyrinth seals were used. Additional components are also used for accurately locating the bearings and for applying a preload. As result bearings are enclosed into chambers as shown in Figure 4.h.

Complex geometries and the presence of multiphase flow involving rotation make the thermal modelling of bearing chambers computationally very demanding if a CFD code is used. For this reason a lumped parameters thermal network was developed in MatLab Simulink. The model was built to investigate the heat transfer phenomena within the bearing chambers but also to evaluate their overall thermal conductivity.

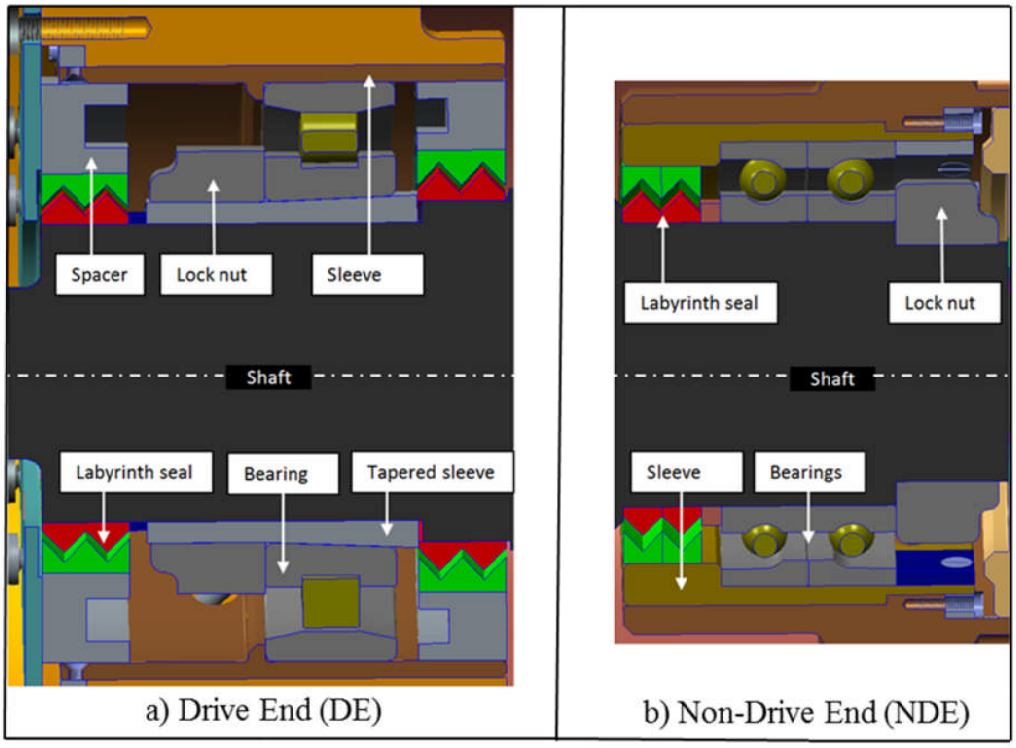



**Figure 4.h: Cross-sectional view of bearing chambers**

Before setting up the model the following were assumed:

- Heat transfer occurs by convection and conduction mainly, radiation was neglected.

- Due to the very tight interference fit, contact resistances for most of the components were not considered.
- Due to the thermal gradients expected, conductive heat transfer occurs along the radial direction only.
- Friction loss is evenly distributed between outer and inner race.
- The heat transferred through the small airgap between the inner and outer ring of the labyrinth seals occurs by conduction only.

The development of a thermal network for both bearing chambers has also required the estimation of critical parameters such as the interface contact resistance between rotating elements and races, the heat transfer coefficient inside the chambers, the bearings' friction losses and the overall material properties of the chamber. These are described from section 4.4.1 to section 4.4.4.

### 4.4.1 Thermal Resistance between Rolling Elements and Races

Whilst most of the conductive thermal resistances could be evaluated by following the general rules described in section B.1.5, the determination of the contact resistance between races and rotating elements has required further investigations.

Generally the thermal contact resistance between the rotating elements and the races depends on the shape and size of the area in contact. The width of this area depends not only on the geometry of the bearing but also on the plastic deformation of the rotating elements due to applied loads, lubricant used and rotational speed; literature shows analytical and experimental studies were conducted to investigate how these factors affect the overall thermal resistance [59-62]. Based on these studies some typical values of conductance were used in the network built; [59] provides values of conductance as function of the preload. The following data shown in Table 4.7 were used.

| Bearing | Preload (N) | Thermal Conductance races/rolling elements (W/K) |
|---|---|---|
| Roller bearing | 0 | 0.15 |
| Angular contact bearing | 100 | 0.2 |

**Table 4.7: Thermal conductance of bearings**

### 4.4.2 Convective Heat Transfer in Bearing Chambers

Due to the complexity of the fluid flow expected inside the bearing chambers, the convective phenomena cannot be approached using ordinary correlations available in text books. Indeed due to rotation the air oil mist is splashed over the internal surfaces of the chambers, the heat dissipated by convection can be significant. Analytical and experimental studies [63, 64] have attempted to weight the impact of several factors such as chambers geometry, air flow rate from labyrinth seals, oil flow rate and rotational speed on the convection heat transfer. These studies led to an empirical correlation (Equation 4.1) for the determination of the heat transfer inside bearing chambers, taking into account all variables involved.

$$Nu = 0.35\, D_h^{1.46}\, Re'^{0.48}_L\, Re'^{0.32}_F\, Re_U^{0.35} \qquad 4.1$$

Where $D_h$ is the hydraulic diameter in m of the chamber, $Re'_L$ is the Reynolds number accounting for the air flowing through the labyrinth seals into the chamber, $Re'_F$ is the Reynolds number function of the oil flow rate used and finally $Re_U$ is the Reynolds number accounting for the effect of the rotation.

In [63] the correlation was validated against experimental data for air flow rates between 5.3 and 20.5 g/s, oil flow rates between 0.4 and 2.8 l/m, speed range between 4,000 and 16,000 rpm and hydraulic diameters between 12 and 34 mm; the maximum discrepancy obtained was ± 20%.

For the machine described in this thesis an oil flow rate between 0.2 and 0.4 l/m was used for the bearings lubrication as recommended by the bearings

manufacturer, an air flow rate of about 5g/s was expected across the labyrinth and the hydraulic diameter of the bearing chambers calculated based on actual dimensions, is in a range between 10 and 12 mm.

The determination of *h* using equation 4.1 requires exact measurements of the mean temperature inside the bearing chambers for the determination of fluids and mixture properties; the lack of this information led the author to use values of heat transfer coefficient *h* reported in [63] and listed in Table 4.8. As values show that *h* increases by around 50% when the rotating speed is doubled; assuming this trend to be valid above 16,000 rpm as well, a convective heat transfer coefficient of 4,000 $W/m^2K$ was assumed for the machine operating point of 32,000 rpm.

| **Speed (rpm)** | **Heat transfer coefficient *h* ($W/m^2K$)** |
|---|---|
| 4,000 | 1000 |
| 8,000 | 1,500 |
| 12,000 | 2000 |
| 16,000 | 2,500 |
| 32,000 | 4,000 |

**Table 4.8: Bearing chambers overall heat transfer coefficients [63]**

### 4.4.3 Bearings Friction Loss

Several approaches are used to estimate the friction loss in bearings and as mentioned in section 2.3.5 several physical variables are involved. In this work two models are presented; the first, the Palmgren's model [65], the second is the model provided by the manufacturer (SKF) [66].

In the Palmgren's model, presented in Equation 4.2 the total friction torque $M_F$ is the sum of the viscous friction torque $M_0$ depending on the lubricant used, its flow rate and it physical properties and the frictional torque component $M_1$ function of the load applied to the bearing.

$$M_F = M_0 + M_1 \quad 4.2$$

The SKF model takes into account more factors; as shown in Equation 4.3.

$$M_F = \phi_{ish}\phi_{rs}M_{rr} + M_{sl} + M_{seal} + M_{drag} \quad 4.3$$

The physical meaning of the first two terms $M_{rr}$ and $M_{sl}$, called rolling frictional moment and sliding frictional moment respectively, is comparable to $M_0$ and $M_1$ of the Palmgren's model; however more terms are included:

- $M_{seal}$ – The **Sealing Frictional Moment** takes into account the friction generated by seals if used; this term is not accounted for in this work as bearings used do not have embedded seals.
- $M_{drag}$ – The **Drag Frictional Moment** term is only used if bearings are partially submerged in oil and it is not accounted for either.
- $\phi_{ish}$ – The **Inlet Shear Heating Reduction Factor** takes into account the viscosity reduction of the lubricant due to shear; this reduces the film thickness and rolling friction.
- $\phi_{rs}$ – The **Kinematic Replenishment/Starvation Reduction Factor** takes into account the "kinematic starvation" effect occurring at high speeds when the lubricant may not have sufficient time to replenish the raceways; the kinematic starvation reduces the thickness of the hydrodynamic film and hence the rolling friction.

All equations and coefficients are tabled for each bearing model in the SKF manual [66].

Table 4.9 shows the power loss due to friction at 32,000 rpm at different oil temperature, 40 °C and 100 °C, calculated using both models. Additionally, losses estimated by using the SKF model without the use of the reduction factors (no ϕs) are also included, in this case losses are quite close to those estimated using the Palmgren model; this is not surprising as the physical

meaning of the main torque terms is comparable as mentioned above. $\phi_{ish}$ and $\phi_{rs}$ play then a significant role when estimating bearing losses, especially when the lubricating oil used is at low temperature.

| | Angular contact bearings | | Cylindrical roller bearing | |
|---|---|---|---|---|
| | 40 °C | 100 °C | 40 °C | 100 °C |
| Palmgren | 414 | 170 | 393 | 163 |
| SKF/ no ϕs | 232 / 433 | 180 / 220 | 123 / 347 | 101 / 151 |

**Table 4.9: Bearings losses in W at 32,000 rpm**

Being the manufacture's model, the use of the losses estimated by using the SKF model was considered more appropriate in this work. All equations used and bearing losses estimated in the range 1,000 – 32,000 rpm are presented in appendix B.2.

### 4.4.4 Overall Chambers Material Properties

Averaged values of density and heat capacity based on the chamber composition were also evaluated using Equations 4.4 and 4.5 instead. The dependency of these two values by the temperature was neglected.

$$\rho_{av} = \frac{\Sigma m_x}{\Sigma V_x} \tag{4.4}$$

$\rho_{av}$ is the average density in kg/m$^3$, $m$ and $V$ are the mass and the volume of each component inside the bearing chamber expressed in kg and m$^3$ respectively.

$$Cp_{av} = \frac{\Sigma Cp_x m_x}{\Sigma m_x} \tag{4.5}$$

$Cp_{av}$ is the average heat capacity of the bearing chamber expressed in J/kgK.

The approach used to determine of the overall chamber thermal conductivity will be described in 4.5.5

### 4.4.5 Thermal Network Developed in MatLab-Simulink

Once the critical parameters were determined the network could be set up. As the full thermal network of the whole bearing chambers, which will be shown later in this section, appear quite complex a detail of the thermal resistances (both conductive and convective) used for the bearing only is shown in Figure 4.i. Conductive resistances between nodes 1-2, 2-3, 3-5 and 5-6 represent the resistances of the races and the contact resistances between races and rotating elements, convective resistances between nodes 2-4, 3-4 and 4-5 are used to model the convective heat transfer of races and rotating elements. The same approach was used for the angular contact bearings.

The cooling effect given by the lubricating oil was modelled by including a thermal resistance between nodes 4 and 7, evaluated using Equation B.7 in Appendix B.

| Node | Description |
|---|---|
| 1 | Shaft |
| 2 | Inner race |
| 3 | Rotating element |
| 4 | Oil |
| 5 | Outer race |
| 6 | Sleeve |
| 7 | Oil in |

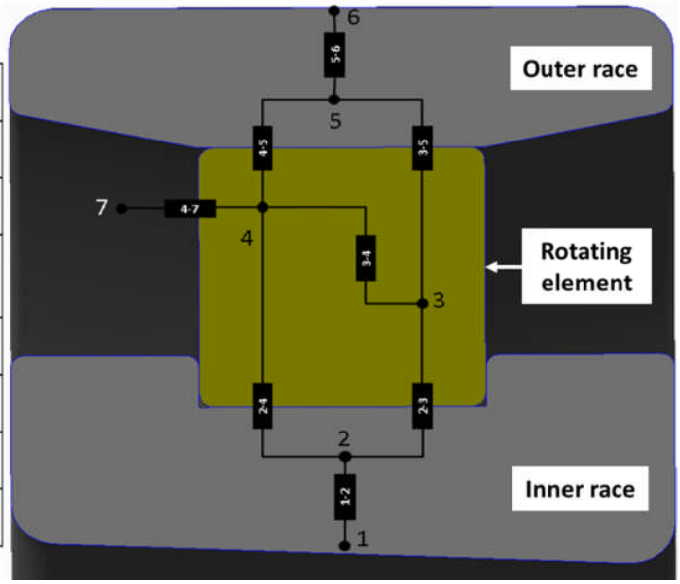



**Figure 4.i: Bearing thermal resistances showing node locations**

The bearing thermal network was developed using MatLab-Simulink thermal module. As literature shows, this modelling tool is also used for thermal

analysis of electrical machines [67, 68]. The following steps were followed for the development of the full thermal network:

- *Bearing chamber conductive path*: a network including conductive resistances only was developed to estimate the overall thermal conductivity of both chambers; these values could then be used as input parameters in MotorCAD and CFD. Figure 4.j shows the conductive thermal network of the non-drive end bearing chamber built using MatLab.

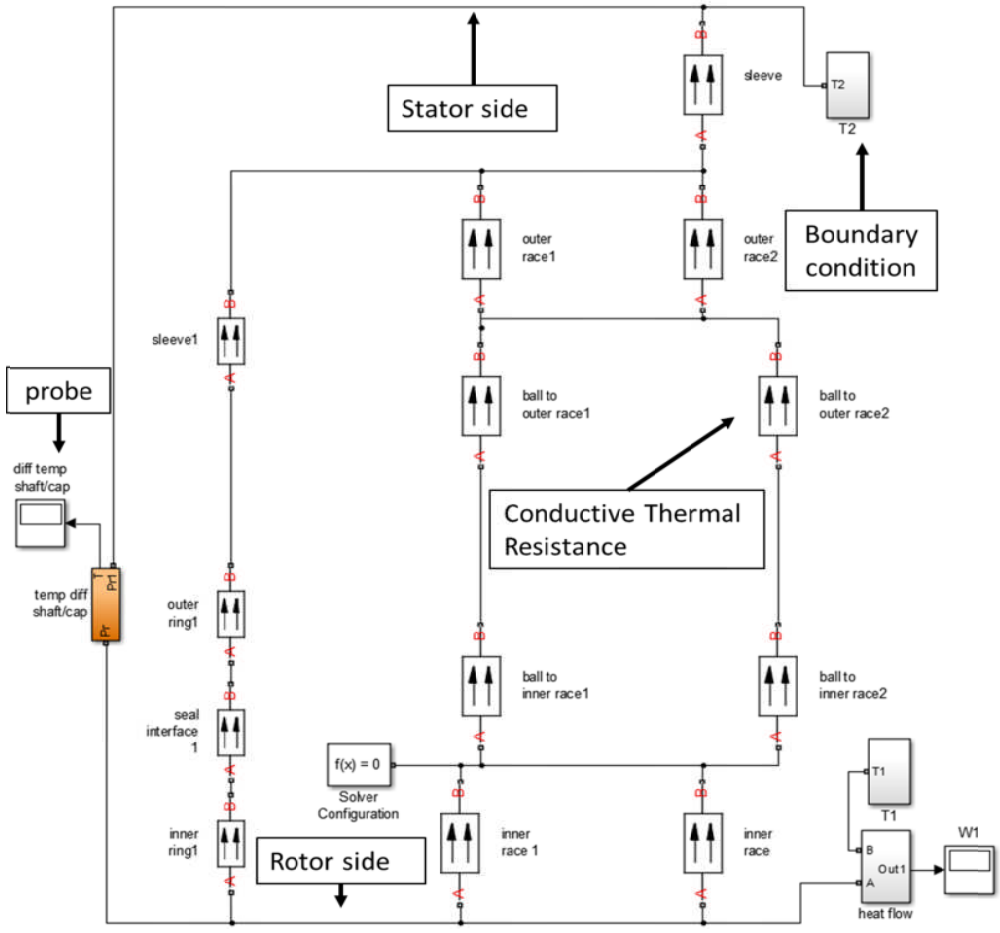



**Figure 4.j: Bearing Chamber Conductive Path**

The determination of the overall chambers thermal conductivity was performed by applying a temperature gradient ΔT between the outer and inner diameter of the chamber, the temperature difference induces a heat flux $\dot{Q}$ allowing the overall conductive thermal resistance to be calculated by using Equation B.2;

assuming the chamber as hollow cylinder which dimensions are known Equation B.2 could be finally used giving the value of the overall chamber thermal conductivity.

- *Full bearing chamber modelling*: convective thermal resistances were included in the previous network to account for convection heat transfer. Convection heat transfer was assumed for all chamber internal surfaces which were expected to be wet by oil. By including the convective thermal resistances the network shown in Figure 4.j. was updated to the following network shown in Figure 4.k.

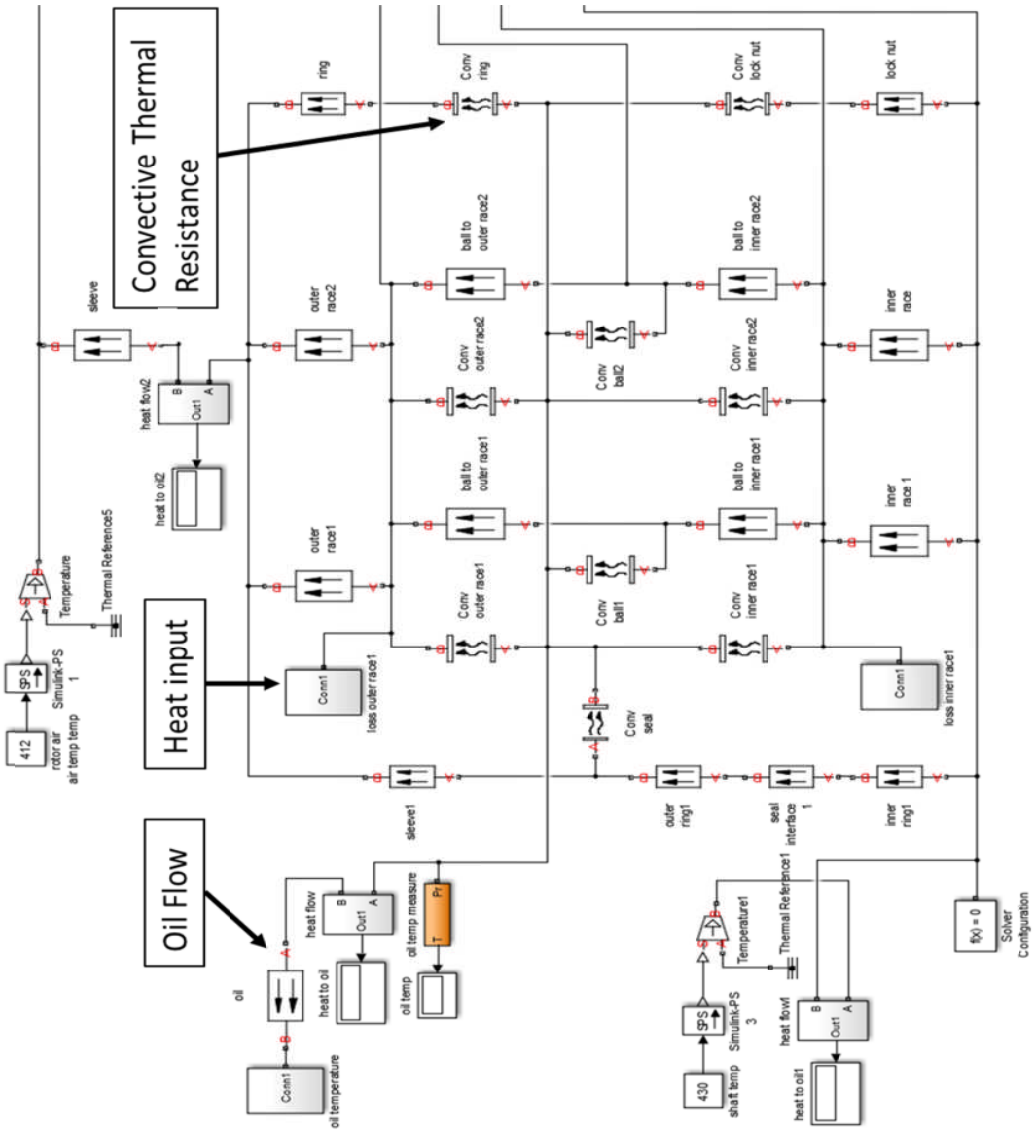



**Figure 4.k: Chamber full thermal network**

- *Rotor modelling*: Combining the two chambers networks by extending the circuit to the whole rotor can provide a better understanding of the heat transfer within the rotor components. For this reason a network including shaft, rotor core, magnets and banding sleeve was built.

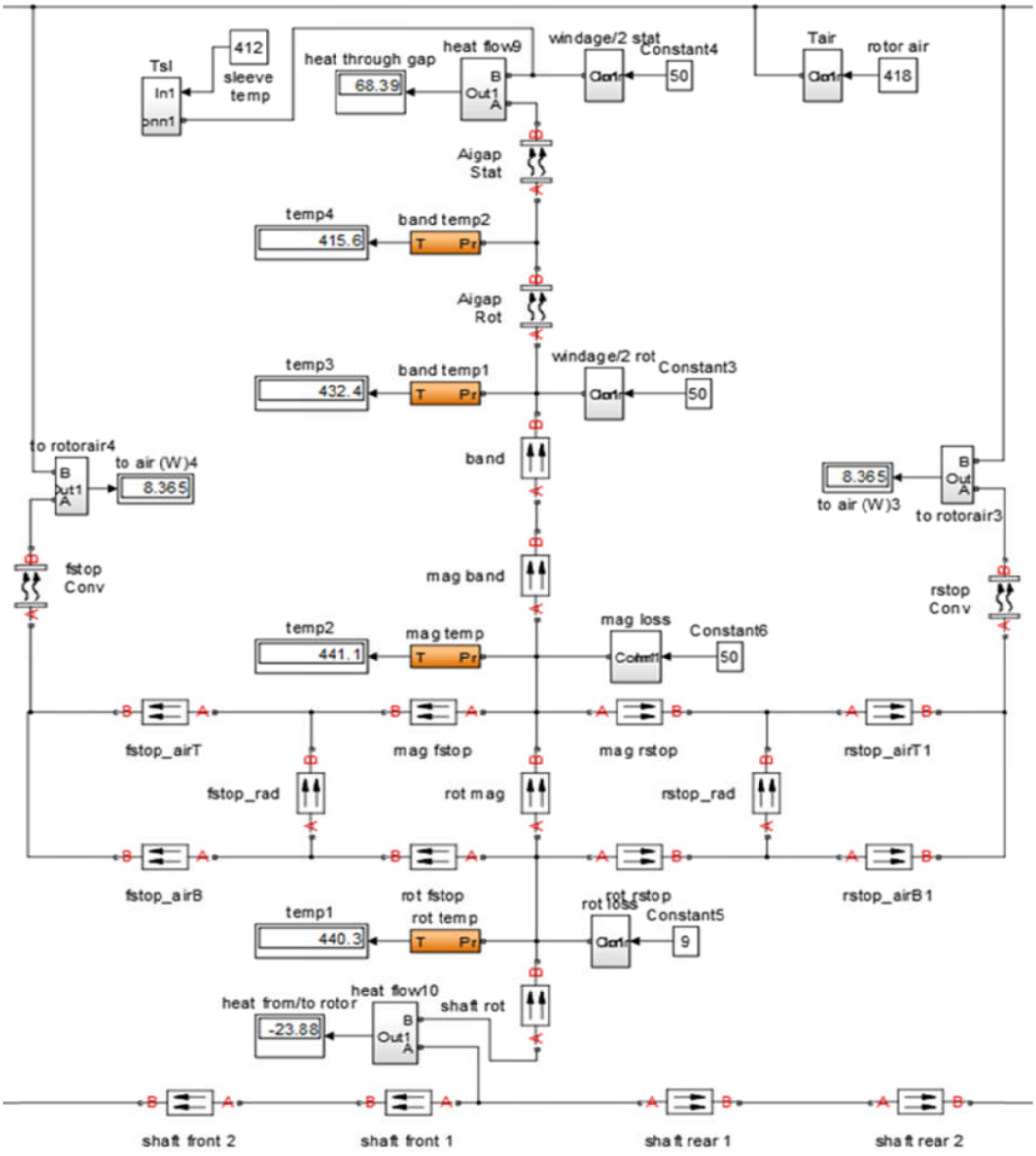



**Figure 4.l: Active Rotor Thermal Network**

For a better understanding Figure 4.m shows a simplified schematic (and only half rotor) of the network presented above.

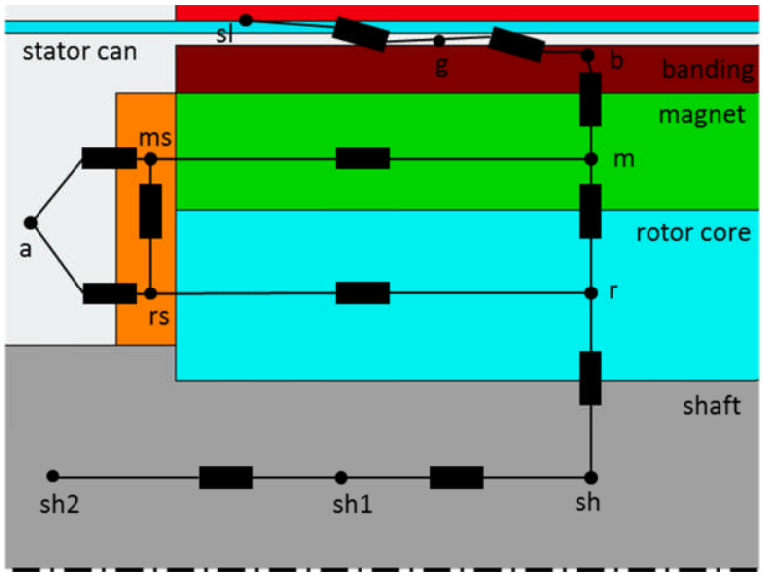



**Figure 4.m: Schematic Active Rotor Thermal Network**

The complete thermal network including all rotor components is shown in section B.2.1; a schematic is shown in Figure 4.n.

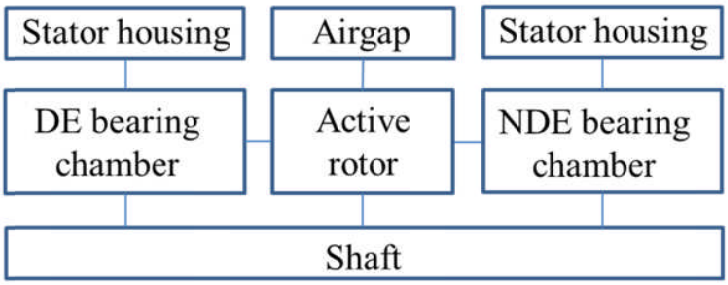



**Figure 4.n: Schematic Full Rotor Thermal Network**

Oil flow rate, oil temperature and power losses seen in Table 4.1 and Table 4.9 were the boundary conditions applied; bearing friction loss was evenly split between bearing inner and outer races. The network has allowed to identify not only the temperature distribution within the rotor but also the amount of heat dissipated into the lubricating oil; this data, shown in Table 4.10, was then used for the machine thermal network as described in section 4.3.4.

| Chamber | Heat removed by lubricant oil (W) |
|---|---|
| Drive End | 30 |
| Non-Drive End | 90 |

**Table 4.10: Heat Removed by Lubricant at 32,000 rpm**

## 4.5 Summary of Analytical Modelling

The lumped parameter network method used for the thermal modelling of electrical machines allows quick analyses of the heat transfer problems with limited computational costs; complex geometries and phenomena can be reduced to relatively simple networks of thermal resistances easy to set up. The rapidity of calculation makes this method a comfortable tool for the investigation of the thermal behaviour of existing machines or new designs. However the limited number of nodes and the inability of predicting some important aspects of the fluid flow represent the major weaknesses of this technique, making it unable of performing accurate conjugate heat transfer analyses.

# 5 Machine Numerical Thermal Modelling

## 5.1 Introduction

This chapter provides a detailed description of the numerical thermal modelling of the whole machine and its critical regions; this includes the description of the domains analysed, meshing approach and solver setup. Discussion over the theory behind Computational Fluid Dynamics (CFD), mainly focusing on the aspects related to the electrical machines and the algorithm used are provided in Appendices C and D.

## 5.2 Overview of CFD Theory

CFD is a technique used to study fluid dynamics by numerically solving the governing equations of fluid flow when the complexity of the problems analysed no longer allows an analytical approach.

The governing equations of fluid flow are commonly known as the Navier-Stokes equations and they consist of coupled non-linear second order partial differential equations.

Depending on the nature of the problem analysed, which might involve multiphase flows, combustion or chemical reactions, several other equations are solved together with the set of Navier-Stokes equations.

The domains analysed are discretised in sub-domains (also known as cells or elements) and all the equations mentioned above are solved simultaneously for each of them, this approach is named the Finite Volume Method (FVM). Depending on the domain extent computed and its complexity this approach can be computationally very expensive and powerful processors may be required. For this reason CFD has become more widely used recently as high power computing became more easily accessible.

## 5.3 Domains Analysed

As described in the previous sections optimal discretisation is the key for accurate solutions. The modelling of electrical machines requires the use of several solid and fluid zones; also, due to the complexity of the physics involved, some regions may need local mesh refinements.

The computational cost when modelling 3D can be significant due to the high mesh count in particular regions. The approach adopted consisted of separately modelling the most relevant and critical regions of the machine in order to locally investigate the fluid flow and heat transfer phenomena but also to find out the optimal mesh configurations to be used later in the full 3D model.

Before setting up the solver the physics of the problem needs to be defined. The mesh exported to the solver is split in several cell zones, as will be described in section 5.3.5, representing the solid bodies and fluid regions.

The first operation is the definition of cell conditions; this consists of assigning the material properties to each solid zone, defining the volumetric heat generation for components where losses occur and including the rotation.

When modelling electrical machines the rotation needs to be included. Two strategies are available for modelling the rotation:

- Multiple Reference Frame (MRF) – is mainly used for steady-state cases or when the rotor-stator interaction is weak. The implementation of this model implies that the fluid domain involved in the rotation needs to be split into a stationary and rotating domains; this will be described in more detail in the following sections. From the numerical point of view using this technique the acceleration of the coordinate system is included in the flow equations and in this way the fluid is steady with respect to the rotating frame.

- Sliding Mesh (SM) – is more suitable for transient simulations or if the rotor-stator interaction is strong such as switched reluctance machines where

big gaps exist between rotor poles. When this technique is used the fluid domain physically rotates; this can lead to much higher computational cost.

Due to the steady-state nature of the cases considered within this thesis and the low interaction between rotor and stator the MRF was preferred in this project, as in previous works [15, 69, 70].

In order to let sub-domains communicate to each other the walls at the interfaces should be manually paired as "coupled wall" if a non-conformal mesh is created between them; when a conformal mesh is created instead sub domains are automatically paired getting an interior interface.

Another important step is the definition of boundary conditions. This operation consists on implementing data which are already known, such as inlet/outlet conditions, flow rates, wall temperature or heat fluxes. Additionally, if only a limited part of domain is modelled, symmetry or periodic boundary conditions should be also included.

All domains considered are generated using Ansys Design Modeller and they are listed below, more details will be provided in the following sections.

- Airgap.
- Stator End Regions (Drive End, Non-Drive End).
- Stator Axial Ducts.
- 20 Degrees Machine Sector.
- Full Machine Model.

### 5.3.1 Airgap Domain

In the machine design considered the airgap consists of a slotless annular gap whose boundary walls, stationary (Stator sleeve) and rotational (rotor), can be considered effectively smooth. The airgap width is 1mm and inner and outer diameters are 92 mm and 94 mm respectively; the axial length (90 mm) is slightly longer than the stator stack length (80.2 mm) due to the aluminium sheet used (rotor stops) to prevent any axial movement of the magnets.

Due to the rotational symmetry of the geometry analysed, a 20 degrees sector of the whole domain was considered as shown in Figure 5.a. The domain was divided into a stationary and a rotational zone, as required to simulate the rotation by using the MRF model described in section 5.3. As no axial flow was imposed in this case, front and rear sides were assigned as symmetry planes; lateral surfaces instead were assigned as periodic boundaries given the periodicity of the domain.

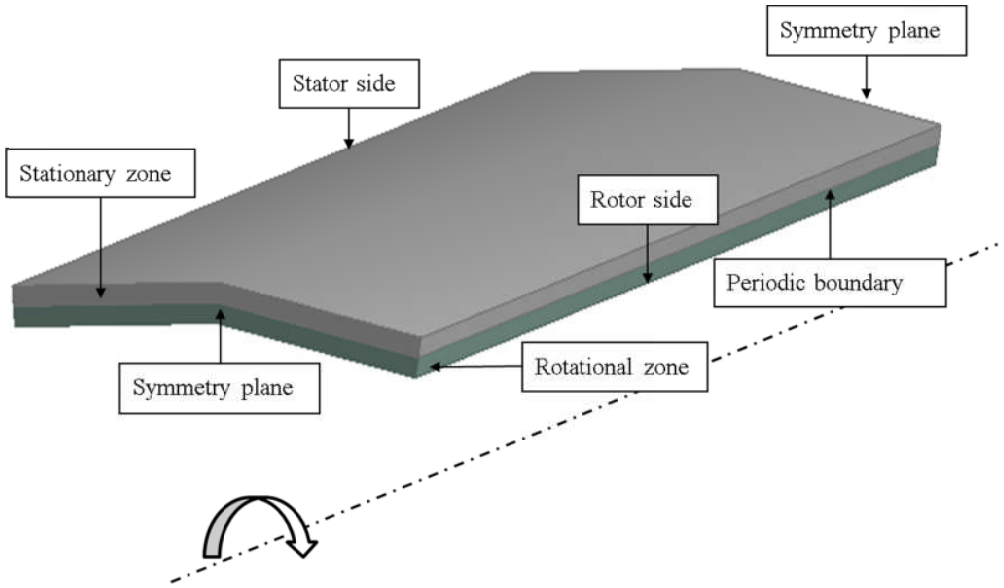



**Figure 5.a: Airgap Domain (lack of circulariy due to graphics issue)**

In order to achieve a higher numerical accuracy and a reduced mesh count the domain was discretised using hexa elements only. The number of cells across the airgap is a critical parameter as near wall phenomena need to be resolved. Previous work in the area [69] recommends the use of at least 10 divisions; however this may vary when high speeds are involved, as in the case of this work. The mesh was then refined until reasonable velocity profiles were achieved; the final mesh count is about 329,000 elements for the whole airgap domain and 26 divisions along the radial direction were assigned. 90 equal divisions were assigned along the axial direction and an aspect ratio of 50 was achieved. As there is no axial flow imposed, the high aspect ratio achieved can be considered acceptable.

The use of Enhanced Wall Treatment requires a $y^+ \approx 1$, this is imposed by accurately assigning the height of the first cell in the proximity of the wall; at 32,000 rpm the thickness of this cell was 8 µm. Figure 5.b shows the mesh generated. As turbulent flow regime was expected, the Realisable k-ε turbulence model was used.

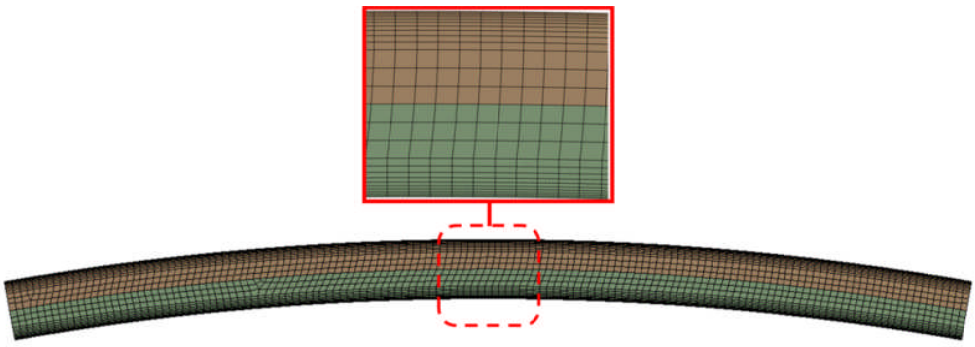


**Figure 5.b: Airgap Mesh**

Several other cases, at lower rotational speeds, were also considered; this has required a slight adjustment of the height of the first cell in order to keep the same value of $y^+$, Table 5.1 shows the thickness assigned at different operating speeds.

| Speed ($10^3$ rpm) | 32 | 30 | 28 | 26 | 24 | 22 | 20 | 18 | 16 |
|---|---|---|---|---|---|---|---|---|---|
| Cell height (µm) | 8 | 8 | 8 | 9 | 9 | 10 | 11 | 11.5 | 12 |

**Table 5.1: First cell heights**

In order to investigate the accuracy of the solution, the tangential velocity profile obtained at different operating speeds was plotted along a line created in the middle of the airgap. The trend of the normalised velocity profiles obtained and shown in Figure 5.c agrees with a typical case of turbulent tangential flow [26]. The viscous friction loss occurring due to the rotation was also investigated and compared to the values obtained analytically as discussed in section 4.4.3; Figure 5.d indeed shows a good match between the two models with a maximum difference within the 10%. The torque component given by the pressure drop was negligible and it wasn't accounted for.

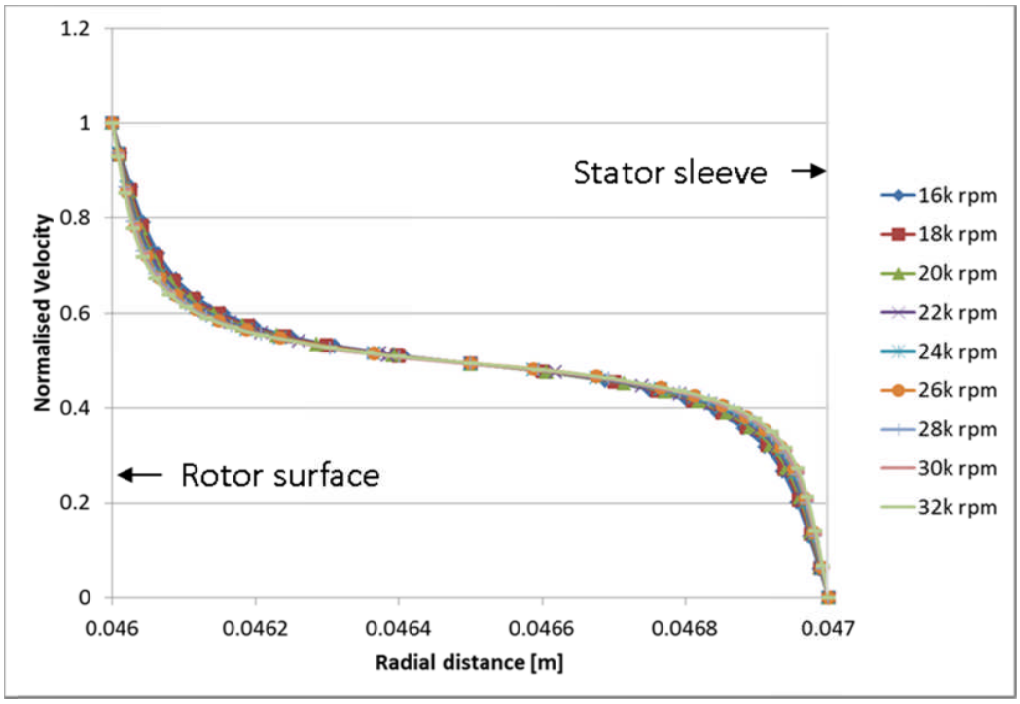



**Figure 5.c: Normalised velocity profiles across airgap**

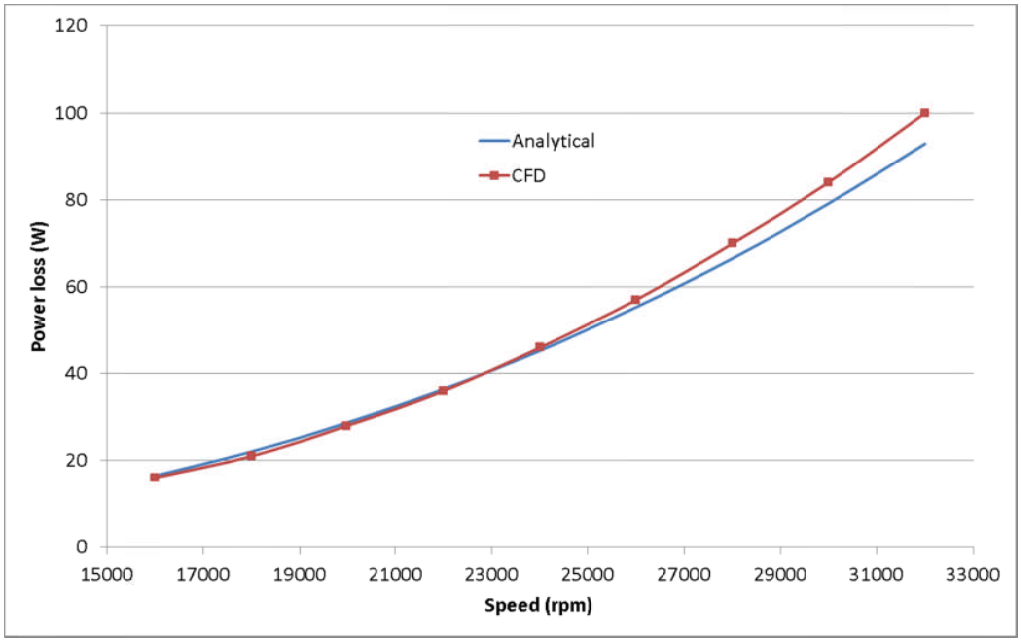



**Figure 5.d: Windage loss**

Data presented shows that the model developed is consistent with expected behaviour according to analytical calculations, being capable of resolving the

fluid flow. The same mesh setup was later used in the machine model which will be described in section 5.4.5.

Another important parameter which was investigated was the heat transfer coefficient on the rotor surface in the airgap. Constant temperatures were set at the rotor and stator side as boundary conditions and a gradient of 40°C was set.

Within Fluent, the heat transfer coefficient is calculated using Equation 5.1 where the heat flux $Q^{"}$ and the wall temperature $T_w$ are computed or assigned as boundary condition, the reference temperature $T_{ref}$ instead is set manually by the user.

$$h = \frac{Q^{"}}{T_w - T_{ref}} \qquad 5.1$$

The selection of the reference temperature is a critical step, in [69] the airgap midstream temperature is taken whilst in [71] the stator bore temperature is used; Figure 5.e shows the comparison between the heat transfer coefficient computed numerically and analytically, as can be seen by picking the stator bore temperature as reference a very good agreement is achieved.

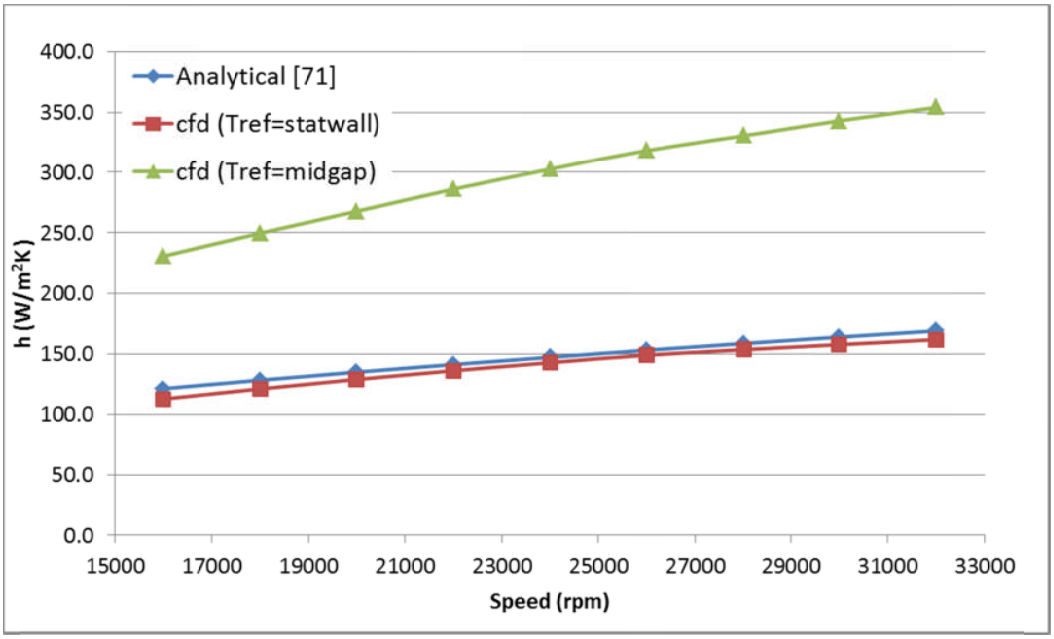



**Figure 5.e: Airgap Heat Transfer Coefficient**

### 5.3.2 Drive End (DE) Region

Direct oil impingement over end-windings in the Drive End region shown in Figure 3.g was used to maximise the heat transfer coefficients and cooling effectiveness.

In order to achieve a more accurate estimation of the heat transfer coefficients on the end-windings a domain including the oil entry region only was analysed. The domain considered consisted of a 20 degrees sector of the oil in the entry region and end-windings as shown in Figure 5.f; the mesh created was made of tetra elements only with an average cell size of 2 mm, the final mesh count was about 300,000.

The main simplification regards the design of the end-windings; it was assumed that they could be represented with a simplified shape and a smooth external surface rather than to describe each individual wire. Actual end-windings were shown in Figure 2.a.

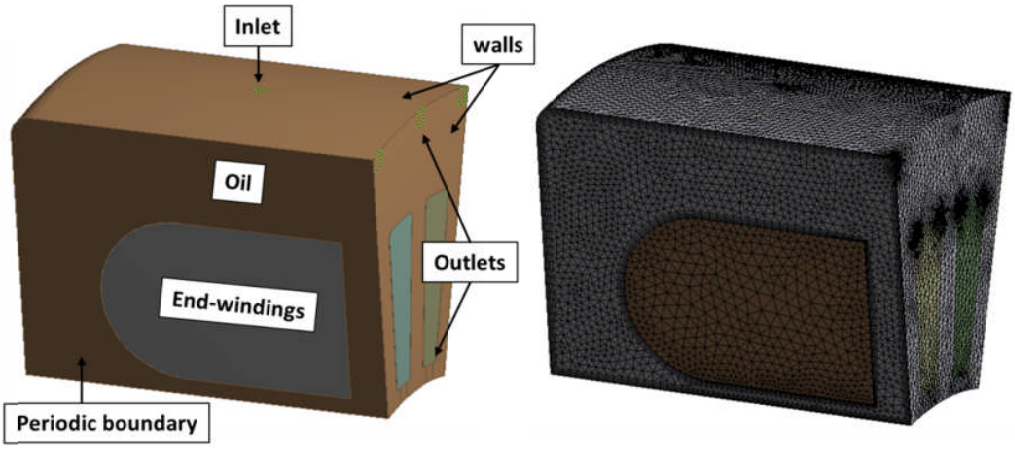



**Figure 5.f: Drive End Region Domain**

After periodic boundary conditions were assigned and external domain's walls were assumed adiabatic, heat inputs were defined. In this machine design both end-windings represent roughly the 50% of the total windings length given that the active length is 80 mm, whilst each end-winding was expected to be at least 35 mm. Therefore this led to the assumption that 25 % of the total copper losses (Table 4.2) occurring in each end-winding. Losses were implemented

into Fluent by enabling the volumetric heat generation option. Winding material properties used are described in section 4.4.2.

A velocity inlet was set for the oil and velocity was calculated assuming that the total flow rate (15 lt/m) used for the machine was split evenly between the 18 radial jets with a diameter of 1.5 mm each, it follows that velocity of 8.86 m/s was set. The oil inlet temperature set was 120°C.

A sensitivity analysis was also carried out to investigate the quality of the model developed. The results of the 20 degrees sector were compared to a full 360 degrees domain having the same design and boundary conditions (Table 5.2). Both cases were run using four cores in parallel; as expected the computational cost of the 360 degrees model was significantly higher requiring between five and six hours to achieve the convergence, whilst the 20 degrees sector only requires up to forty minutes allowing carrying out parametric studies. Table 5.2 shows the average heat transfer coefficient computed on the end-windings surface and the average end-windings temperature in the two cases considered. In both DE and NDE End Region models the reference temperature used was the oil average temperature inside the end region.

The reasonably small difference between the two cases shows that the simplification initially made can lead to consistent solutions

| | 20 degrees | 360 degrees | % difference |
|---|---|---|---|
| $\bar{h}$ end-windings ($W/m^2K$) | 1545 | 1645 | 6 |
| $\bar{T}$ end-windings (K) | 402.7 | 402.4 | 0.01 |

**Table 5.2: 20 degrees sector versus 360 degrees domain**

The End Region was also analysed using the fluid domain only and assuming different boundary conditions at the end-winding wall, such as constant temperature (140°C) and constant heat flux (1000 $W/m^2$) as shown in Table 5.3. Results show that further simplifications to the model can be made without significantly affecting the solution.

| | Volumetric heat generation ($W/m^3$) | Constant surface temperature (K) | Constant surface heat flux ($W/m^2$) | Max. % difference |
|---|---|---|---|---|
| $\bar{h}$ end-windings ($W/m^2K$) | 1545 | 1565 | 1588 | 3 |

**Table 5.3: Drive End Region boundary conditions**

### 5.3.3 Non-Drive End (NDE) Region

One of the features of the cooling adopted, described in Chapter 3, consists of a flow deflector located in the stator end region at the non-drive end side of the machine. This deflector aims to induce turbulence over the end windings in order to enhance the heat transfer.

As similarly described for the DE end region, in the previous, section, a 20 degree sector was considered with the same mesh density as shown in Figure 5.g. Same oil flow rate was assumed and heat inputs were used as boundary conditions.

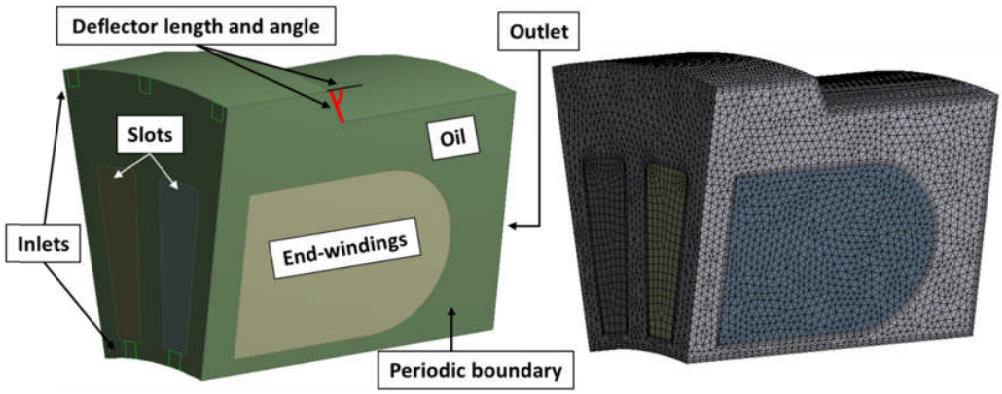



**Figure 5.g: Non Drive End Region Domain**

A parametric study was conducted in order to identify the optimal deflector design capable of maximising the heat transfer coefficient over the end-winding surface. A case without a deflector was initially considered; in the cases where a deflector was included, parameters such as deflector length and angle were changed, Table 5.4 summarises the cases considered.

| | Case 1 | Case 2 | Case 3 | Case 4 | Case 5 |
|---|---|---|---|---|---|
| | No deflector | 5 mm/ 30° | 5 mm/ 45° | 5 mm/ 60° | 8 mm/60° |
| $\bar{h}$ end-windings ($W/m^2K$) | 1145 | +0.5% | +5% | +9.5% | +10% |

**Table 5.4: Non Drive End Region Parametric study**

Although Case 5 gives the highest value of heat transfer coefficient, Case 4 was identified as optimal; this is because an excessive length of the deflector can cause the housing to get in contact with the end-windings outer surface and this could potentially affect negatively the cooling of that area but also represent a risk. However an increase of about 10% of the heat transfer coefficient can be achieved.

### 5.3.4 Stator Ducts

The fluid flow inside the stator axial ducts was investigated analytically in section B.1.4.

Numerical investigations were also carried out on a 3D model of an axial duct; the domain consists of one square straight pipe, with a side of 2 mm and a length of 80.2 mm (stator stack length). Hexa elements only were used to generate the mesh, leading to more accurate plotting of the velocity profiles within the duct.

In order to resolve the important aspects of the fluid flow quite fine mesh was required. 120 equal axial divisions and 31 divisions orthogonally to the duct axis were assigned, leading to an overall mesh count of about 184,000 cells with a maximum aspect ratio of 20. A coarser mesh was also created to be used in the full machine model in order to reduce the mesh count; this was still capable of predicting the same heat transfer coefficients. Figure 5.h shows a detailed view of the two meshes created; the coarser mesh has 40 divisions along the axial direction $z$ and 12 along $y$ direction, the total mesh count is

4,320 elements with a maximum aspect ratio of 25. Data presented in this section were computed using mesh *a*.

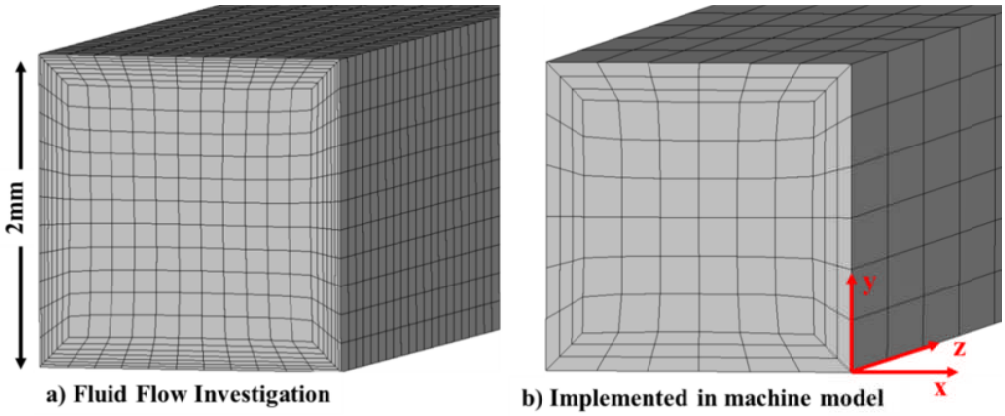



**Figure 5.h: Discretisations duct domain**

An oil flow rate of 3.4 $10^{-6}$ $m^3/s$ was set having assumed an even distribution of the coolant among the 72 ducts and constant wall heat fluxes (1,000 and 10,000 $W/m^2$) were assumed at the duct's walls, representing an heat dissipation of 50 W and 500 W. Laminar flow was expected (Re=540 as shown in section 4.3.1.3) so the fluid domain could be set as a laminar zone within Fluent. Outflow was set at the outlet. No-slip condition, introducing zero velocity at the wall set at the duct wall.

The flow across multiple axially spaced lines was investigated in order to observe the evolution of the fluid flow; these were located at 1 mm from the duct edge along the *x* direction. As shown in Figure 5.i the flow becomes fully developed after about 60 mm confirming the analytical prediction of 55 mm, described in section B.1.4.

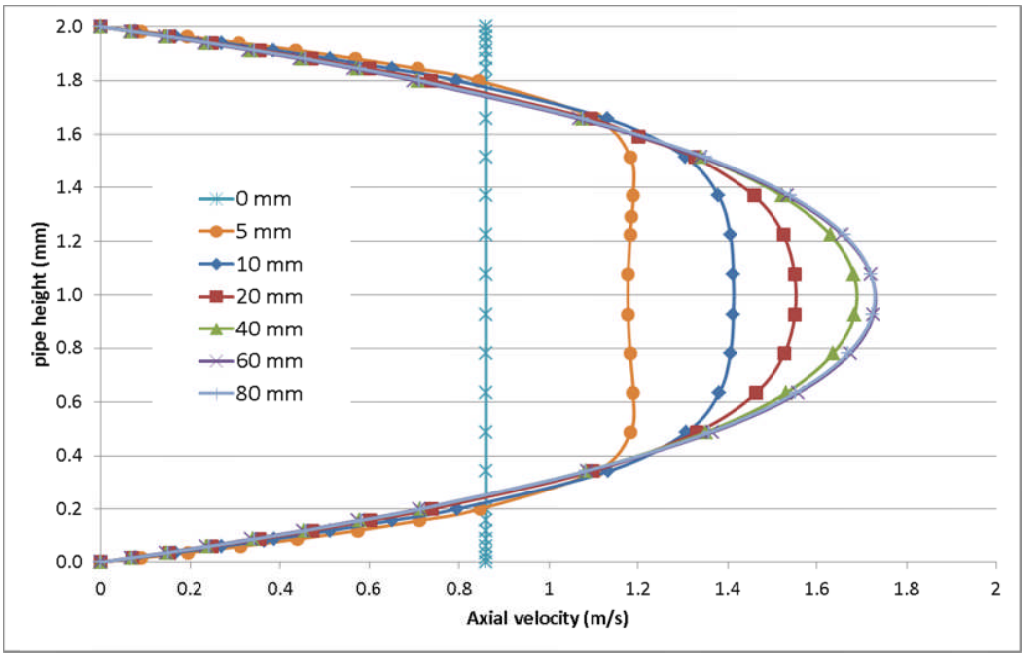



**Figure 5.i: Velocity profiles inside stator ducts**

In this case the reference temperature used for the calculation of the heat transfer coefficient was the mean centreline temperature; this led to a difference of maximum +15% with analytical predictions (865 and 975 $W/m^2K$). Less than 1% difference between the fine and the coarse mesh was achieved instead.

### 5.3.5 20 Degrees Machine Sector

Once the most critical areas of the machine were analysed separately, a model including all the components was built. Building a full machine model is quite expensive from the computational point of view as several million elements might be required; for this reason a 20 degrees sector only was considered initially as shown in Figure 5.j.

The domain was entirely created within Ansys Design Modeler; this has allowed the original design geometry to be significantly simplified making it suitable for a CFD simulation. Several features such as small surfaces in the order 1 mm, small grooves and chamfered corners were removed being judged not relevant for the simulation purposes; this has a direct impact on the mesh quality, mesh density and hence reduced calculation time.

Components like the stator winding and bearing chambers were modelled as bulk solids and overall thermal properties, presented in Chapter 4, were assigned.

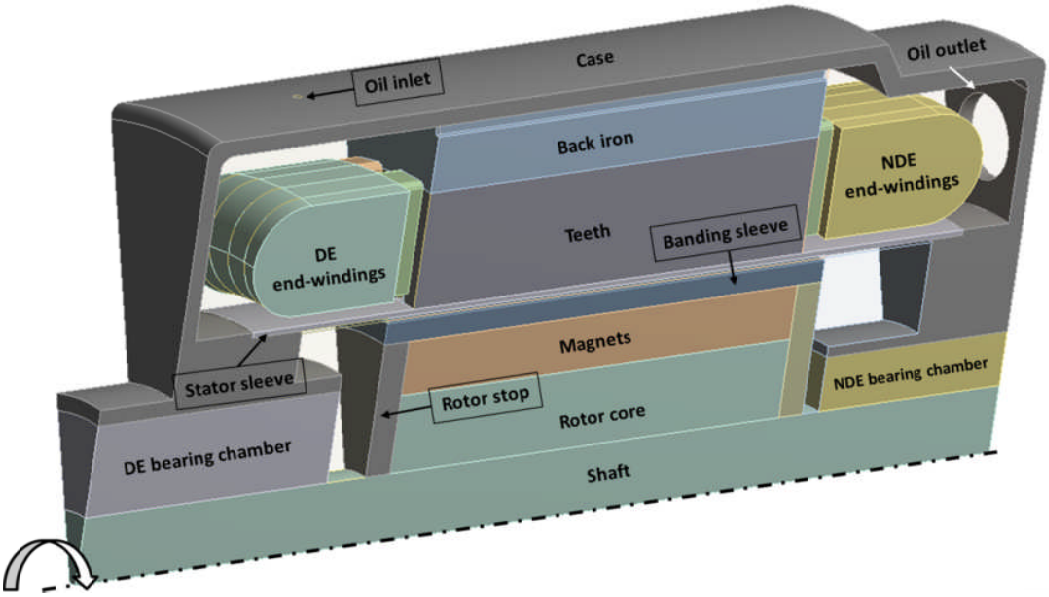



**Figure 5.j: 20 degrees machine domain**

The complexity of the multi-body model also required several zones to be split, in this way higher quality meshes could be achieved. The oil domain was split into DE oil, axial ducts and NDE oil as shown in Figure 5.k, allowing replication of the optimised meshes described in the previous sections. Figure 5.k and Figure 5.l can be considered the inverse of Figure 5.j where solid parts have been removed and only fluid domains are highlighted.

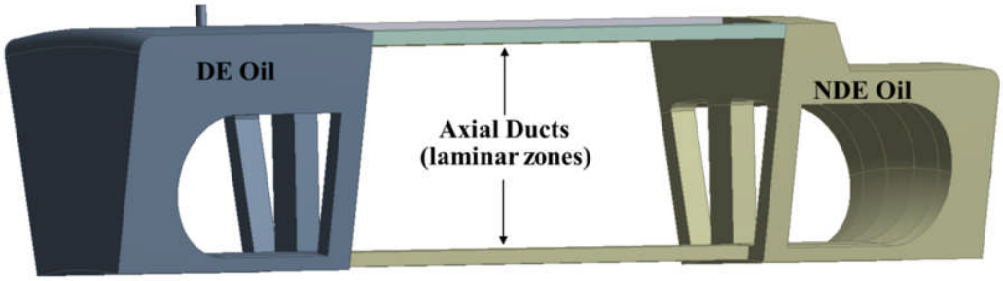



**Figure 5.k: Oil Domain**

Similarly the air domain in the rotor region, where the air domain was split into Drive End Air (DE Air), Non Drive End Air (NDE Air) and Airgap; furthermore the domains were also split into stationary and moving domain in

order to implement the rotation, as described in section 5.4.1. The air domain is shown in Figure 5.l.

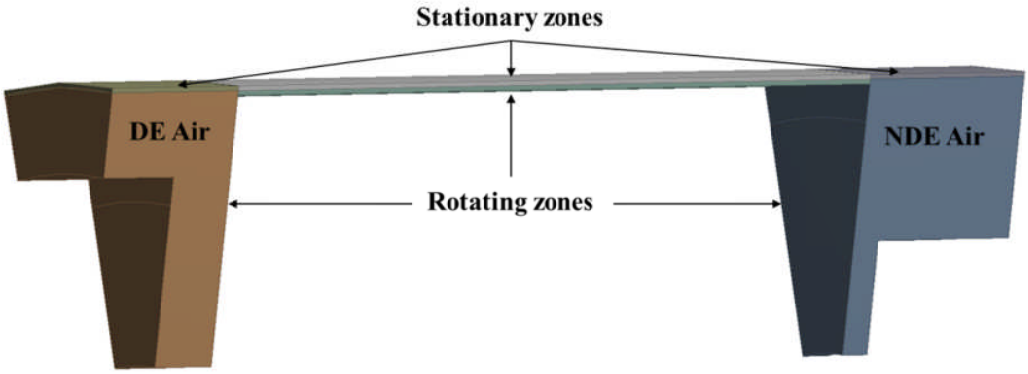



**Figure 5.l: Air Domain**

Other bodies, such as stator lamination and winding were also split to assign more realistic losses distribution.

Being a multi-body domain several meshing techniques available within Ansys Mesher were used to achieve an optimised mesh. For a higher numerical accuracy conformal interfaces were created between most of the bodies; this led to slightly more dense mesh as the software adapts the interfaces automatically to get a perfect match. The final mesh, shown in Figure 5.m, is made of about 1.5 million elements with both hexa and tetra element types used. In order to avoid high skewed cells at the axis, the vertex was removed.

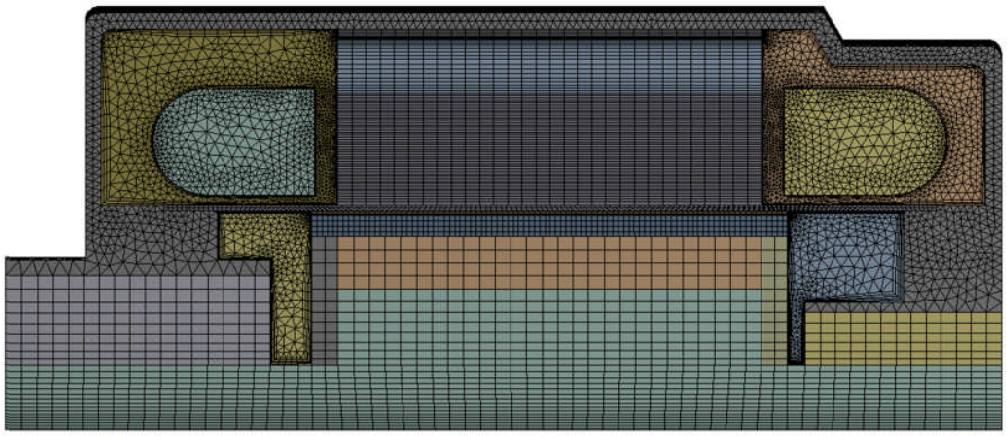


**Figure 5.m: 2D axisymmetric slice of 20° sector of full machine**

Table 5.5 provides mesh details for each sub-domain modelled.

| Zone | Elements number | Elements type |
|---|---|---|
| Oil | 513,888 | Tetra - Hexa |
| Airgap | 328,983 | Hexa |
| Coils | 232,120 | Hexa-Tetra |
| Air | 191,553 | Hexa-Tetra |
| Housing | 42,173 | Tetra |
| Stator lamination | 79,600 | Hexa |
| Banding sleeve | 125,100 | Hexa |
| Stator sleeve | 10,080 | Hexa |
| Rotor stops | 240 | Hexa |
| Magnet | 540 | Hexa |
| Shaft | 5,200 | Hexa |
| Bearings | 1,155 | Hexa |
| Rotor core | 1,080 | Hexa |
| **Total** | **1,531,712** | |

**Table 5.5: Mesh Details 20° Machine Sector**

Periodic boundary conditions were assigned to account for the 20° periodicity of the model. The same boundary conditions used for the thermal network and shown in Table 4.5 were used, power losses were implemented as volumetric heat source and all material properties were assigned for each zone.

As windings are made of a non-isotropic material the orthotropic function was enabled for assigning different values of thermal conductivity along radial, axial and tangential directions. The same values were assigned for the end-windings but assuming the highest value of thermal conductivity along the tangential direction rather than in the axial as for the windings in the slots. However the highly anisotropic thermal conductivity assigned causes the solution to diverge; as suggested in [69] the issue was solved by implementing the following codes into the Text User Interface (TUI) in Fluent:

- (rpsetvar ‘temperature/explicit-relax? #t)
- (rpsetvar ‘temperature/secondary-gradient? #f)

The first code uses explicit relaxation of temperature whilst the second disable secondary gradient of temperature.

Constant properties were assumed for the oil as the temperature rise expected was not significant. However temperature dependent viscosity and density were assumed for the air.

The Realizable k-ε model was used as turbulence model, however as the flow regime in axial ducts was expected to be laminar the laminar zone function was enabled for this part of oil domain.

An oil flow rate of 0.83 lt/min, which is a $1/18^{th}$ of 15 lt/min, was set at the inlet and an initial temperature of 120°C was assumed. Natural convection (h= 5 $W/m^2K$) and an ambient temperature of 35°C were assumed at the housing and bearing chambers outer walls.

The case was run using four cores in parallel and the convergence of energy and flow equations was reached after about 500 iterations; however 500 more iterations were required to reach torque convergence, monitored as described in Appendix D.5. A total calculation time of about 3 hours was required.

The contour and vector plots in Figure 5.n show how heat transfer and fluid flow were simultaneously resolved.

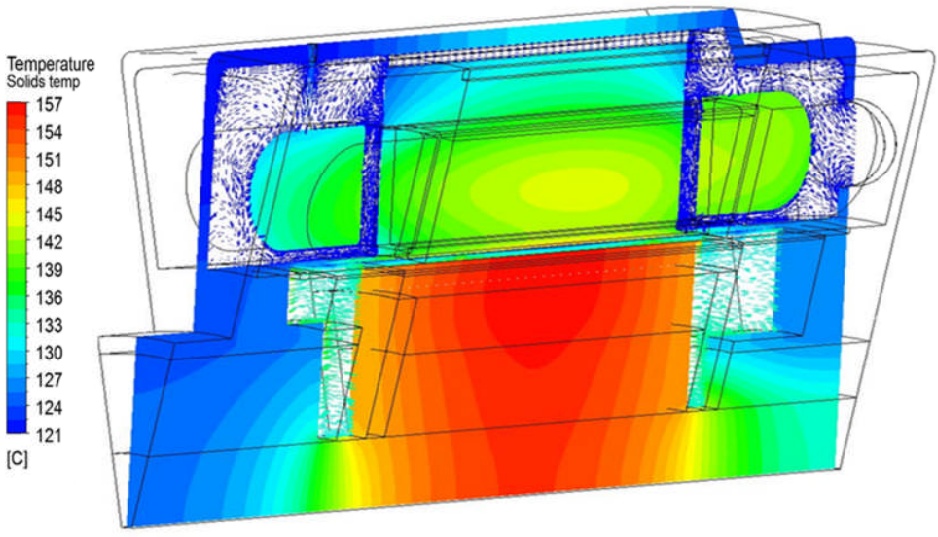



**Figure 5.n: Results of the conjugate heat transfer analysis**

### 5.3.6 Full Machine Domain

As described above, several simplifications to reduce the computational cost of the numerical investigations were implemented; nevertheless developing a full 360° model of an electrical machine, including both fluid flow and heat transfer, still requires significant effort.

A full model of the machine was developed at the later stage of design in order to check the consistency of the simpler models earlier presented (20° sector). As shown in the section view in Figure 5.o the domain includes all the machine components.

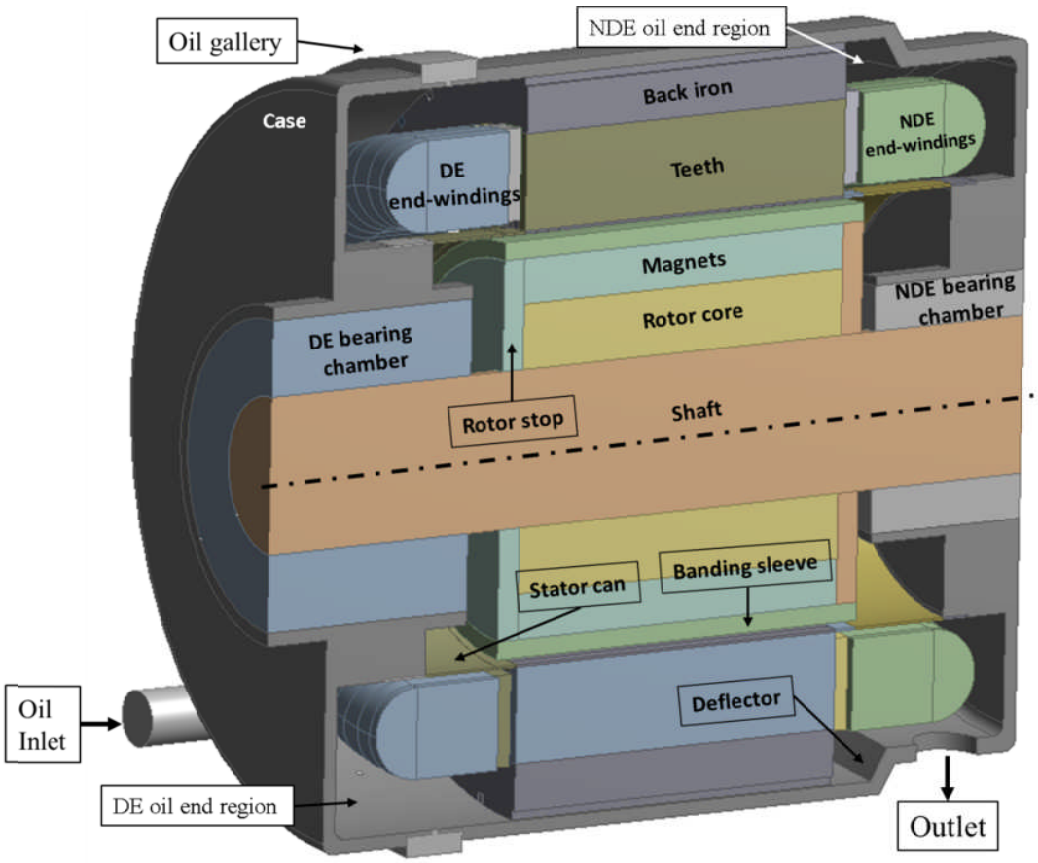



**Figure 5.o: Section view Full 360° Machine Model**

The oil inlet port was modelled in order to investigate the pressure drop occurring between the main inlet and the oil gallery. Figure 5.p shows in **b** the 3D model built for the CFD analysis and in **a** the actual design; as can be seen,

the fluid domain only was modelled to avoid including unnecessary geometrical features.

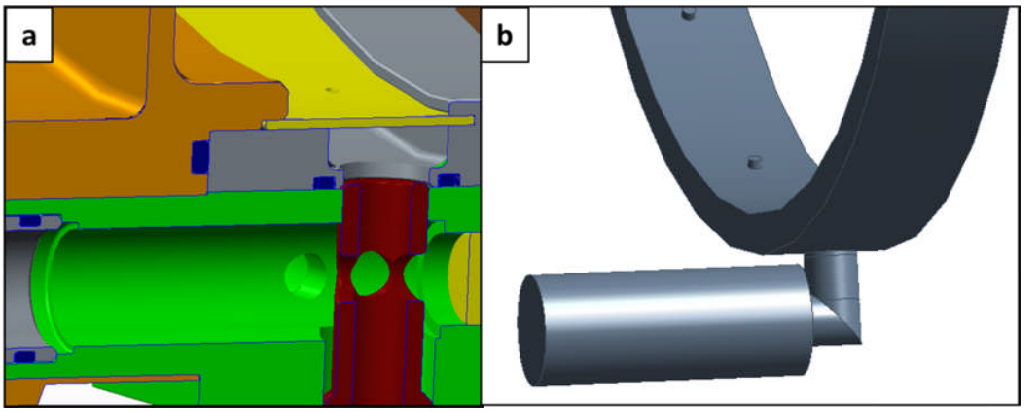



**Figure 5.p: Oil Inlet port domain**

Following the geometry creation, discretisation of the domain was carried out. When dealing with large and complex domains like this, the meshing procedure needs to be performed with great care in order to achieve high quality and computationally efficient meshes.

The 20° machine sector consisted of about 1.5 million elements; by replicating the same mesh in the 360° model a final mesh count of about 27 million elements would be achieved, going beyond the calculation capabilities of the PC used. Further geometrical simplifications were therefore required; some zones such as the oil domain, coils and stator sleeve were split into several zones.

Both hexa and tetra elements were used and conformal interfaces were created between the main components in the stator and in the rotor regions. Also in this case several meshing techniques were used simultaneously and, in order to achieve a high quality mesh, all components were discretised following a very specific order. The optimal setup was achieved based on previous meshing experience and several attempts. The final mesh, shown in Figure 5.q consisted of about 19 million elements; detailed information about the mesh created for each zone is also provided in Table 5.6

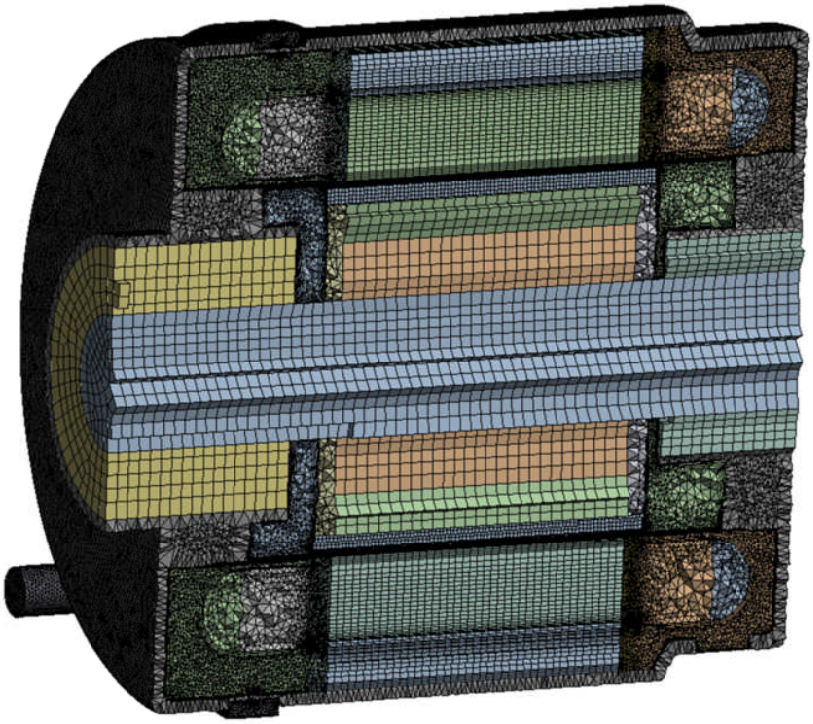


**Figure 5.q: Mesh of 360° Machine Model**

| Zone | Elements number | Elements type |
|---|---|---|
| Oil | 9,998,306 | Tetra - Hexa |
| Airgap | 3,140,370 | Hexa |
| Coils | 2,322,118 | Hexa-Tetra |
| Air | 1,934,930 | Hexa-Tetra |
| Housing | 702,407 | Tetra |
| Stator lamination | 542,800 | Hexa |
| Banding sleeve | 103,640 | Hexa |
| Stator sleeve | 101,520 | Hexa |
| Rotor stops | 36,960 | Tetra |
| Magnet | 9,423 | Hexa |
| Shaft | 8,385 | Hexa |
| Bearings | 7,520 | Hexa |
| Rotor core | 6,480 | Hexa |
| **Total** | **18,914,859** | |

**Table 5.6: Mesh details of 360° Model**

Material properties and boundary conditions used were exactly the same as those used in the 20° model. Four cores in parallel were used to compute the solution, leading to a calculation time of about 20 hours.

Once the solution was obtained, key machine components temperatures computed using the 20° and 360° models were compared. As shown in in Table 5.7, the results obtained using the two models are very close and a maximum difference of about 2% is achieved.

| | 20° | 360° |
|---|---|---|
| Component | Average / Maximum [°C] | Average / Maximum [°C] |
| End-windings DE | 135 / 141 | 134 / 139 |
| End-windings NDE | 142 / 145 | 141 / 144 |
| Windings | 144 / 150 | 142 / 147 |
| Stator teeth | 140 / 144 | 140 / 143 |
| Magnets | 156 / 158 | 156 / 158 |

**Table 5.7: Comparison Machine key temperatures**

The good agreement between the two models leads to the conclusion that the 20° model is sufficient for carrying out the thermal characterisation of the starter generator examined.

## 5.4 Summary of Numerical Modelling

Computational Fluid Dynamics is a very powerful calculation tool capable of resolving very complex fluid flow and heat transfer problem simultaneously. However the complex analysis steps, starting with the domain creation and ending with the post-processing, make this technique very time consuming and very expensive from the computational point of view.

Although the numerical modelling of an entire electrical machine can require significant effort, the cost of the simulations can be largely reduced by performing local investigations in the most critical areas or considering only limited sectors of the whole machine. This allows the determination of critical parameters such as temperatures, heat transfer coefficients and pressure drops with reasonably low computational costs.

Numerical data, such as convective heat transfer coefficients, can be also used to improve the thermal network described in Chapter 4. The integration of the two models, numerical and analytical, is the strategy adopted within this work primarily for the analysis of the performance of the cooling strategy employed but also for the identification of further solutions aimed to improve the thermal efficiency of the machine examined.

# 6 Experimental Facility

## 6.1 Introduction

Experimental tests were undertaken to validate the thermal models described in Chapters 4 and 5. The starter/generator was tested using a high speed rig with speed maximum rating of 35,000 rpm. The high speed rig consisted of a drive motor (induction machine) connected to the machine under test through a gearbox and using a flexible connection with a splined coupling; Figure 6.a shows a schematic of the test rig, the starter/generator is attached to the test chair using a flanged connection.

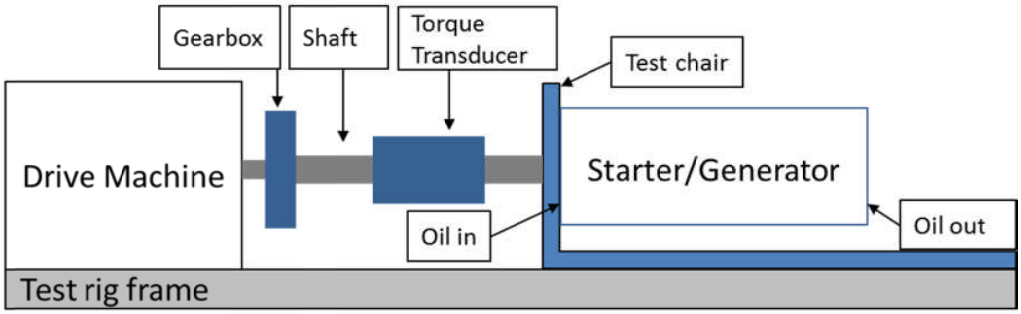



**Figure 6.a: Schematic of Test Rig**

Temperatures, pressures, flow rates and torque were the quantities acquired throughout the tests and used for validating the models. A hydraulic circuit for the cooling and lubrication of the machine was designed and commissioned. A detailed description of the oil circuit and its components will be provided in the following sections.

## 6.2 Oil Circuit

The schematic presented in Figure 6.b represents the design of the oil circuit designed for the testing of the machine to monitor the most relevant parameters; as shown three separate lines were created, two for the lubrication of the bearing chambers and one for the cooling of the machine. Each line was provided with a flow meter, flow controller and temperature and pressure sensors.

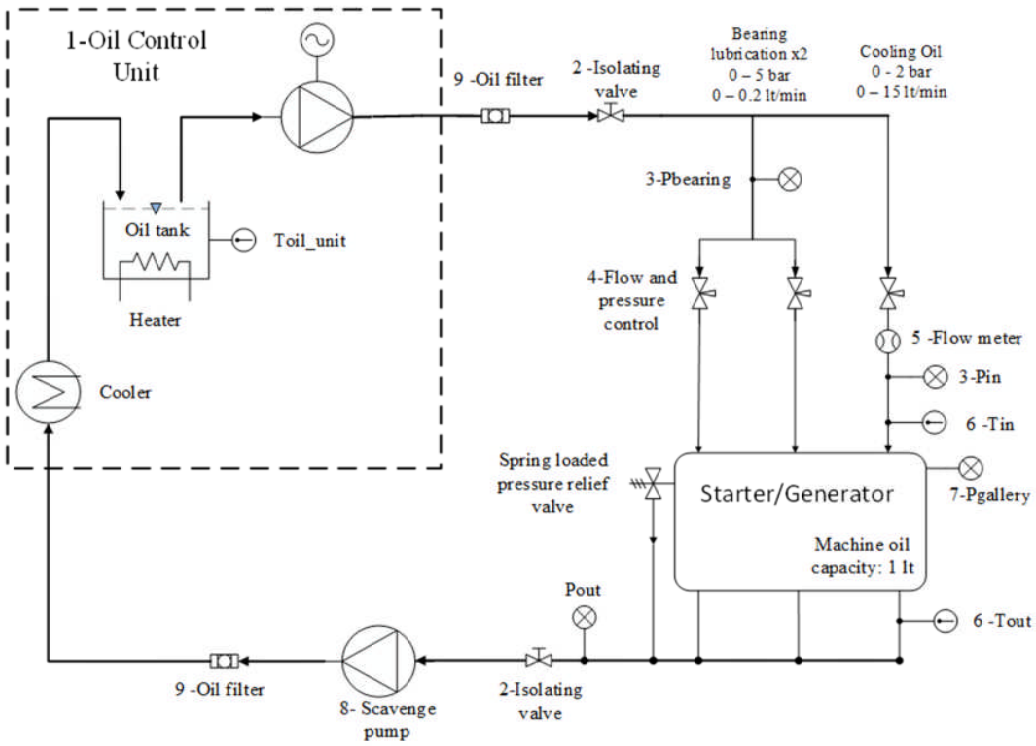



**Figure 6.b: Oil Circuit**

Figure 6.c shows the main machine connections. The main oil inlet is located on the flange as previously shown in Figure 3.f. From the inlet port most of the oil flows into the stator and a minimal part flows into the bearing lines, sight glasses are used to monitor the condition of the oil and the amount of it flowing through the bearing chambers. The oil by-pass line is only used if the oil inlet pressure exceeds 4 bar. All the return lines are connected to a manifold and finally the oil goes to the scavenge pump through the hose.

Figure 6.d also shows the system used to regulate the flow rate and pressure of the oil coming from the control unit. The oil temperature is set manually in the control unit.

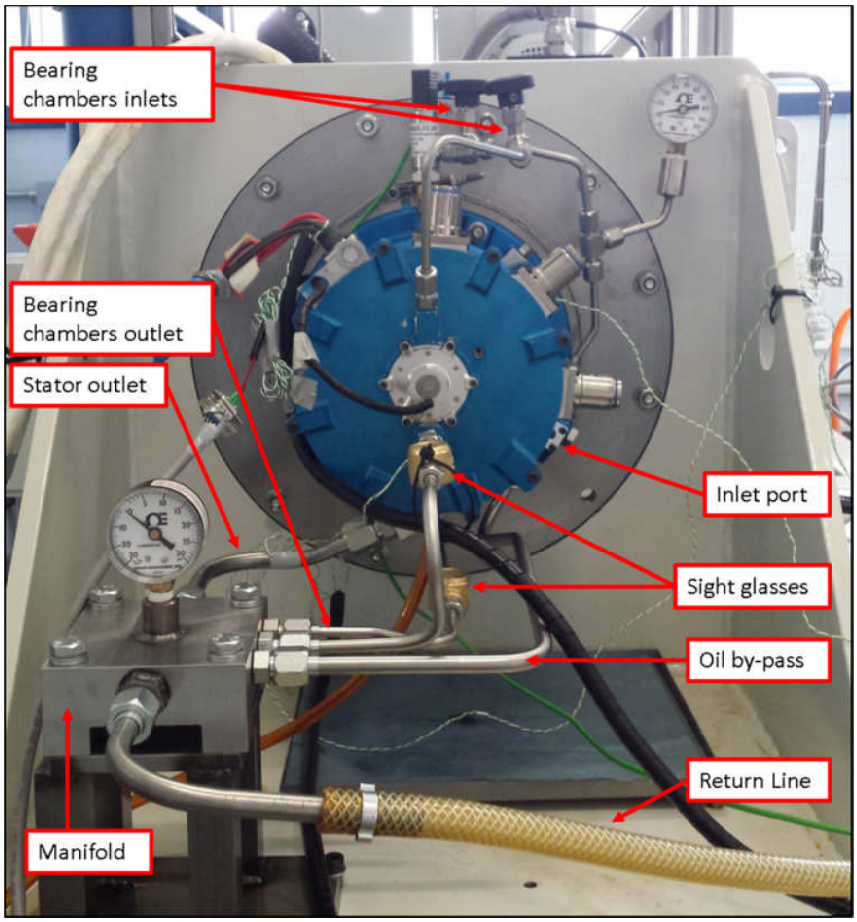



**Figure 6.c: Hydraulic machine connections**

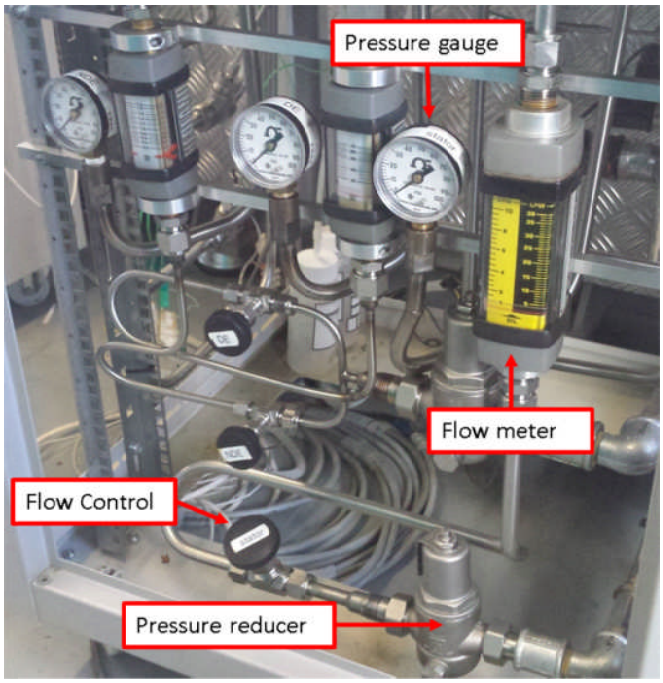



**Figure 6.d: Control Main Oil Line**

Stainless steel pipes were used for most of the lines; hoses were used instead for the main inlet and out lines. Compression fittings were used to prevent any leakage.

The system includes the following main components:

- *1 - Oil Control Unit*: Temperature controlled unit TT-248 by *Tool Temp* capable of supplying an oil flow rate of 15 lt/min with a maximum pressure of 4.5 bar.
- *2 - Isolating valves*: On-Off valve to isolate the circuit from the unit if required.
- *3 - Pressure gauge*: monitoring the pressure of the oil fed to the bearing and stator chamber and measuring the pressure drop across the machine
- *4 - Pressure Regulator*: Pressure reducing valve for regulating the oil inlet pressure: valve series 481 by *Goetze Armature*
- *4 - Oil flow regulator*: Stainless steel needle valves regulating the oil flow rate for the two bearing chambers and stator chamber.
- *5 - Flow meter:* variable area flow meter for monitoring the oil flow rate, described in section 6.2.2.
- *6 - Thermocouples*: measuring the temperature at the inlet and outlet of the stator chamber.
- *7 - Pressure transducer*: measuring the oil pressure inside the gallery before being impinged over windings.
- *8 - Scavenge pump*: generating up to 0.3 bar negative pressure for an effective suction of the oil from the machine: suction unit including a filter and pump capable of removing up to 25 lt/min.

- *9- Oil filter*: 10 µm filter eliminating any particle which might cause blockages.

### 6.2.1 Thermal Measurement

Temperature measurements were required both to validate the thermal models developed but also to investigate the performance of the cooling system adopted.

As shown in Figure 6.b thermocouples were used to measure the inlet and outlet oil temperature; by knowing the oil flow rate, these readings allow calculation of the amount of heat dissipated into the coolant. Some more thermocouples were located inside the machine, bulkhead connectors were used to take the thermocouple wires out of the machine avoiding any oil leak. Three thermocouples were used; these were located in the middle of the stator slots along the radial and axial directions as shown in Figure 6.e in order to measure the highest likely temperatures.

No thermal measurements could be taken into bearing chambers due to impossibility of safely introducing any sensor.

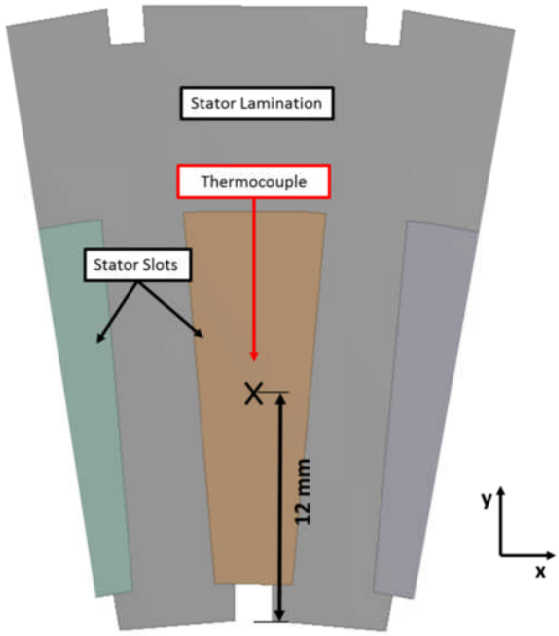



**Figure 6.e: Thermocouple location**

To guarantee a good contact with the conductors and avoid any damage a thermal paste was used at the thermocouple junction when this was inserted into the slot. K-Type thermocouples with an accuracy of ±2.5 °C (according IEC-584-2 standard) were used. Thermocouples were inserted during the winding process.

### 6.2.2 Flow rate Measurement

A flow meter was used to monitor the amount of oil flowing inside the machine; this, as mentioned above in section 6.2, is also needed to calculate the heat absorbed by the oil. An in-line variable area flow meter by *Hedland* shown in Figure 6.f was used.

A petroleum-based meter was selected being suitable for oils and a wide range of viscosity (4 to 108 cSt). The model used has a range 0-30 lt/min with an accuracy of ±2% FS, meaning an accuracy of ±4% can be achieved when working with 15 lt/min (± 0.36 lt/min).




**Figure 6.f: Oil flow meter**

For an accurate reading a correction factor $C_{FM}$, depending on the oil used, need to be applied as recommended by the manufacturer; this is calculated as in equation 6.1.

$$C_{FM} = \sqrt{\frac{0.879}{oil\ specific\ gravity}} \qquad 6.1$$

### 6.2.3 Pressure Measurement

Pressure was measured at three locations; two pressure gauges were used in the main inlet and outlet lines as described in section 6.2; with a pressure transducer, shown in Figure 6.g, used to measure the pressure inside the oil gallery, described in section 3.4.2.

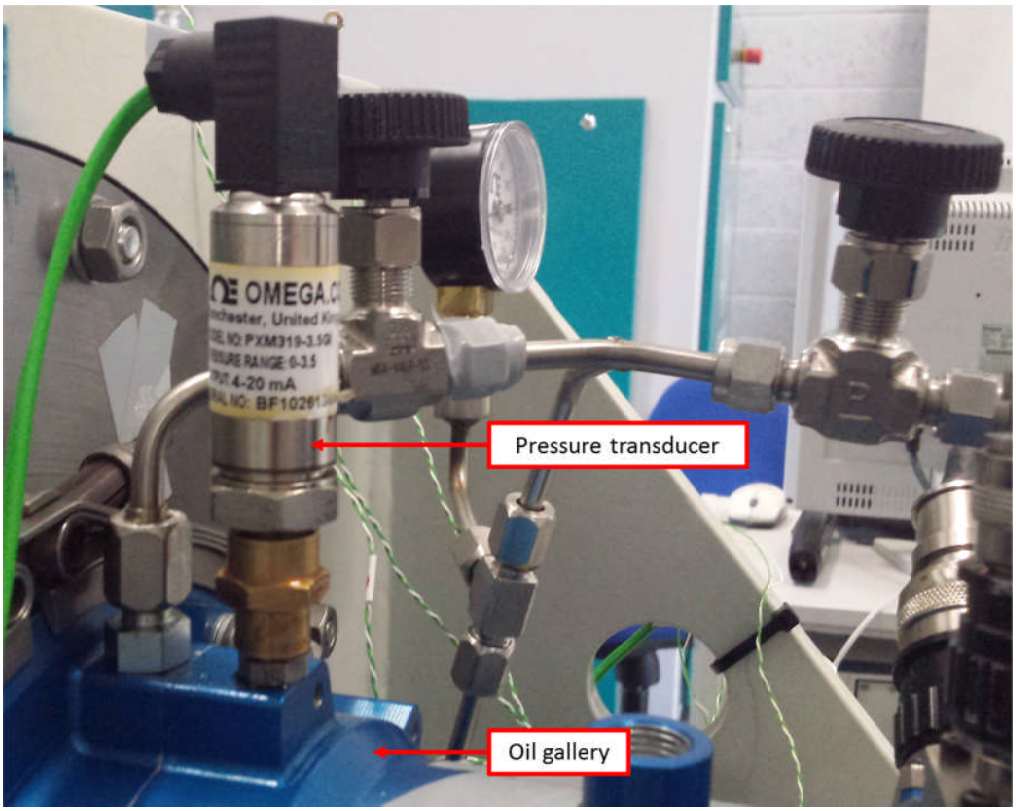



**Figure 6.g: Pressure transducer**

Data logging can only provide information about the pressure drop across the machine and across the inlet port only; this can be compared to the numerical model.

The pressure transducer used (PXM309 by *Omega*) has a measuring range 0 to 3.5 bar and an accuracy of ±0.25% on the full scale. Pressure gauges (PGC series by *Omega*) at the inlet and outlet can measure ranges 0 to 7 bar and -1 to 1 bar respectively with an accuracy of 2%. All measured pressures were gauge pressures.

### 6.2.4 Torque and Speed Measurement

Torque and speed measurements were required to identify the mechanical losses at different operating speeds; these data can be then compared to the windage and bearing losses estimated analytically as shown in Chapter 4.

A torque transducer, ET-1303 by *Torquemeters*, was used; this is connected to the starter generator using a flexible coupling and a splined connector.

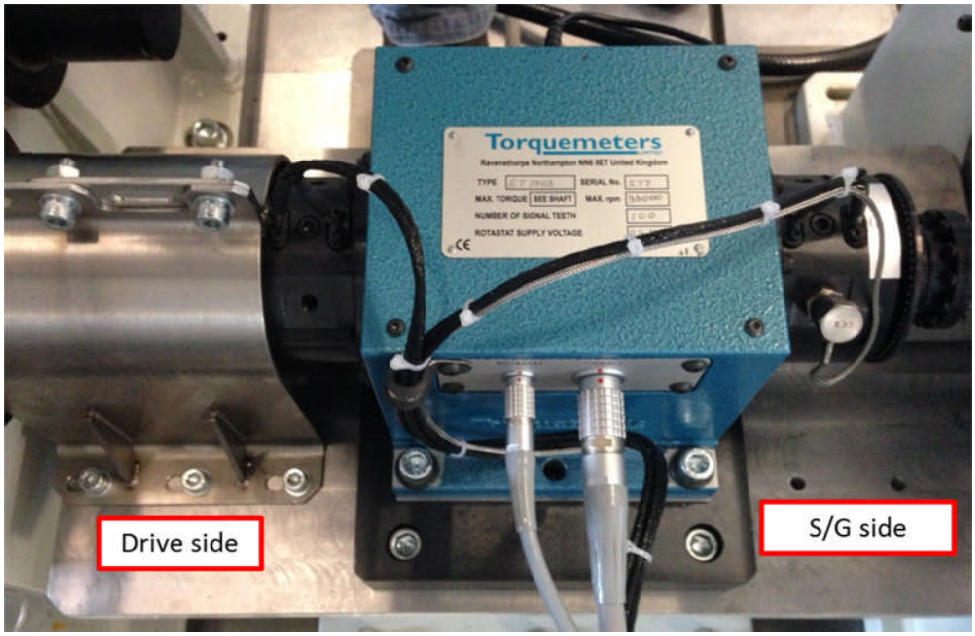



**Figure 6.h: Torque transducer**

Data from the transducer are directly sent to the rig control unit where data can be displayed.

Throughout testing torque measurements were taken when steady state condition was achieved.

### 6.2.5 Data acquisition system

Two terminal modules, TB-4353 and SCB-68 by *National Instruments*, were used to connect thermocouples and pressure transducers to the data logger PXIe-1073. A serial port was used to interface the data logger to a PC where data could be displayed and stored using the NI Signal Express software.

### 6.2.6 Uncertainty Analysis

All experimental data are affected by errors introduced by the equipment used; indeed as described above, every measuring device used has its own level of accuracy usually stated by the manufacturers as an uncertainty range.

Uncertainty must be then taken into account when analysing experimental data, furthermore if some quantities are obtained as function of several variables all or partially experimentally determined an uncertainty analysis must be carried out.

The Kline&McClintock method [72] combines the uncertainties introduced by all instrument and provide the overall uncertainty of the result obtained. Given a quantity $\Re$ function of variables $x_i$ having uncertainties $\nu_i$, the uncertainty in the quantity $\nu_\Re$ can be calculated as shown in Equation 6.2 below:

$$\nu_\Re = \sqrt{\left(\frac{\partial \Re}{\partial x_1}\nu_1\right)^2 + \left(\frac{\partial \Re}{\partial x_2}\nu_2\right)^2 + \cdots \left(\frac{\partial \Re}{\partial x_n}\nu_n\right)^2} \qquad 6.2$$

## 6.3 Summary

An experimental test facility was developed to investigate the thermal behaviour of the starter/generator and to test the performance of the cooling arrangement used. Experimental data are crucial for the validation of the analytical and numerical models developed during the design process so several tests were carried out. In the following chapter all results will be analysed and compared.

# 7 Results and Validation

## 7.1 Introduction

Chapters 4 and 5 provided a detailed description of the modelling approaches used to investigate the performance of the cooling arrangement presented in Chapter 3 and to analyse the thermal behaviour of the machine design. The following chapter will initially present the results obtained from the analytical and numerical modelling; these will be then validated experimentally to investigate the accuracy of the thermal models developed.

## 7.2 Wet Stator Cooling Performance

Throughout the design process, due to the absence of experimental data, the performance of the cooling system was evaluated by analysing and comparing the results obtained from the analytical and numerical thermal models developed.

Information regarding the machine temperature distributions were used to establish whether the cooling strategy adopted was capable of letting the machine run safely when running at full power. Therefore key machine components, such as windings and magnets, have to operate within acceptable temperature limits.

The performance of the Wet Stator option was compared to a conventional Oil Jacket configuration.

### 7.2.1 Machine Temperature Rise

Both the thermal models developed and described in Chapters 4 and 5 provided detailed temperature distributions within the machine. Although the thermal network can only provide temperatures at a few locations compared to the numerical CFD model, key temperatures could still be identified. Figure 7.a *a* and *b* show a temperature plot of the machine cross section computed using the two modelling techniques.

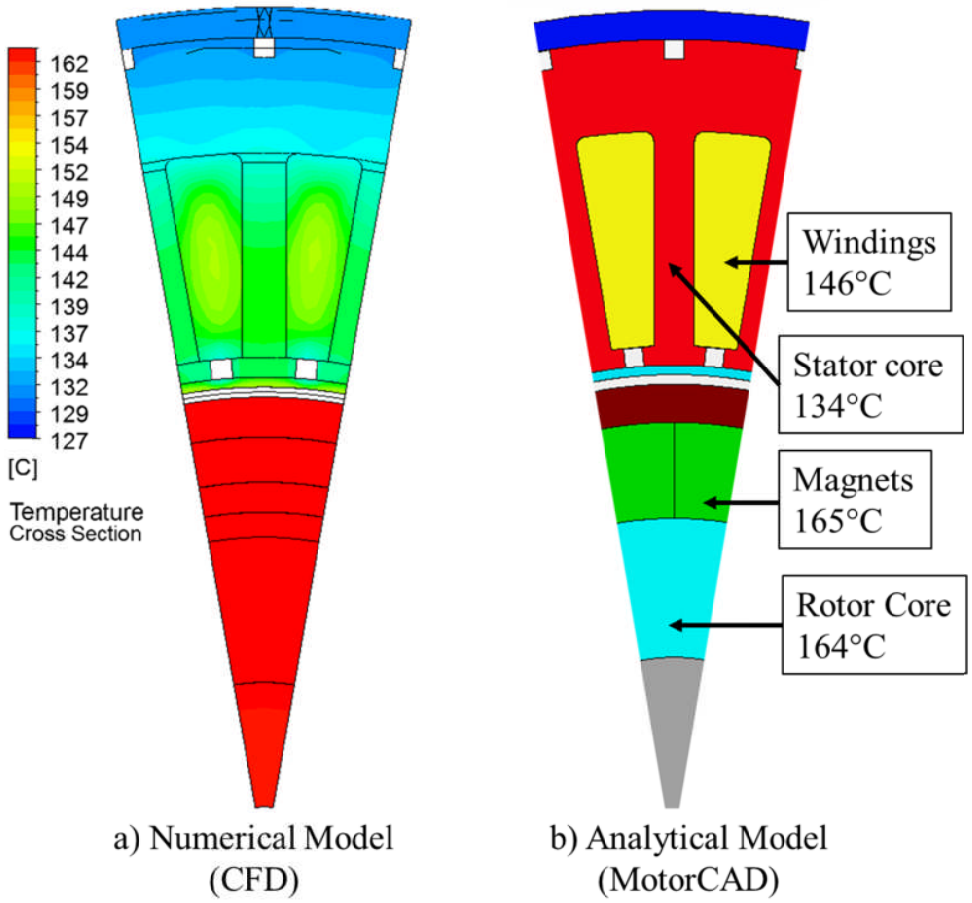



**Figure 7.a: Temperature Plot Cross-Sectional View – Oil inlet at 120°C**

The temperatures predicted show that in key machine components, such as windings and magnets the maximum differences within 5°C are achieved. Figure 7.b shows the maximum temperature rise predicted in main machine components. As can be seen the most significant differences can be observed in end-windings and bearings where the discrepancy between the maximum temperatures predicted is between 6% and 15%. As described in Chapters 4 and 5 the major limitation of the lumped parameters network is the modelling of the fluid flow; although some numerical data were implemented to overcome this deficiency, the difference shown in end-winding temperatures highlights the issue. The significantly lower bearing temperatures predicted using custom thermal network developed in Simulink can be attributed to the fact that the very detailed model can account for the heat dissipated into the oil which splash inside all internal surface of the chamber.

Overall the results of the simulations show that the configuration selected is capable of maintaining the machine temperatures well below acceptable limits (200°C for windings and 220°C for magnets), leaving a sufficient safety margin in case higher losses should occur. The assumption of the oil inlet temperature of 120°C was done only to consider the worst case scenario; during normal operation the starter/generator is fed with oil at much lower temperature meaning that the safety margin will be greater.

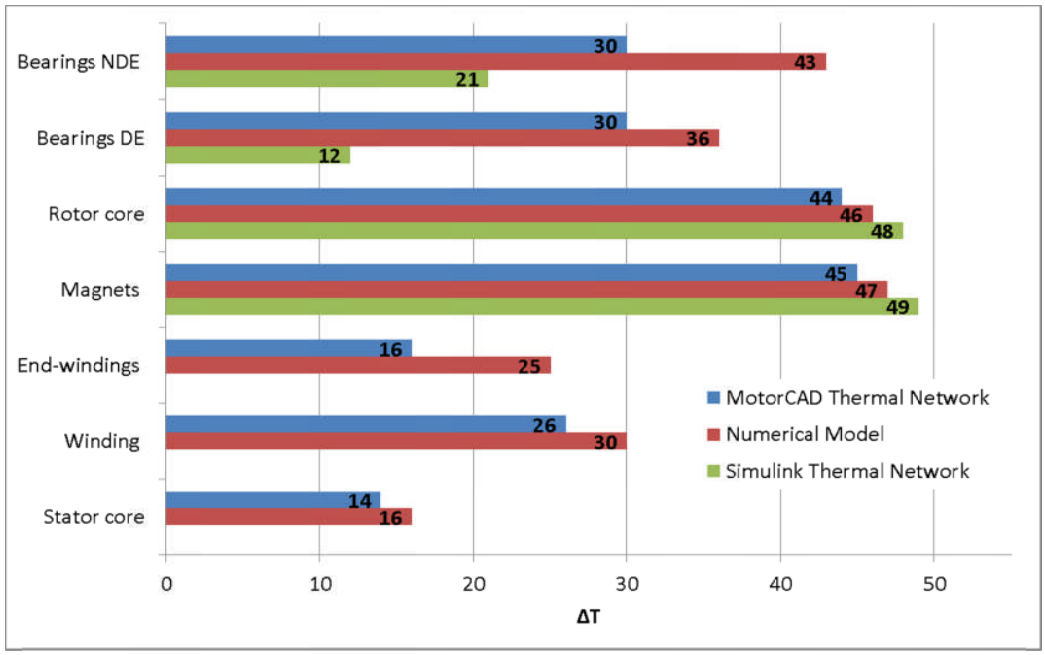



**Figure 7.b: Predicted maximum Temperature Rises at Full Power (rise above inlet oil temperature of 120°C)**

Another quantity which was analysed to investigate the performance of the cooling adopted is the amount of heat dissipated by the coolant. Based on the predicted oil temperature rise the estimated percentage of heat dissipated is 1652 W in MotorCAD and 1750 W in CFD, representing the 86 % and the 91% respectively. The rest of the heat is assumed to be dissipated into the ambient through the casing.

As described in section 4.3.2 MotorCAD is capable of scaling the copper losses depending on the local operating average winding temperatures estimated. However for carrying out the comparison between the analytical and

numerical models that function was initially disabled. By including the copper loss temperature dependency as well, a reduction of about 10% of the copper loss initially implemented (which was estimated assuming windings at 180°C) was calculated, leading to a reduction of the maximum windings temperature rise of only 2%. Although a significant change is not achieved, this function can be used to compare the performance of different cooling strategies as will be described in section 7.2.2.

### 7.2.2 Wet Stator vs Oil Jacket Cooling

As discussed in Chapter 3 the thermal management of the starter generator aims not only to keep components within acceptable temperature limits, but also to maximise the overall machine efficiency by limiting the temperature dependant losses.

The loss scaling option, available in MotorCAD, described in section 4.3.3 and recalled in section 7.2.1, allowed the estimation of the resistive losses at different operating temperatures and different cooling configurations.

A jacket cooling option, described in section 2.5, was implemented into the existing machine thermal model described in Chapter 4, replacing the direct cooling option. The same boundary conditions such as oil flow rate and heat inputs were used, this allowed a comparison of the performance of the two cooling techniques. Figure 7.c shows a comparison between the temperature rises obtained using the Wet Stator and Oil Jacket cooling options.

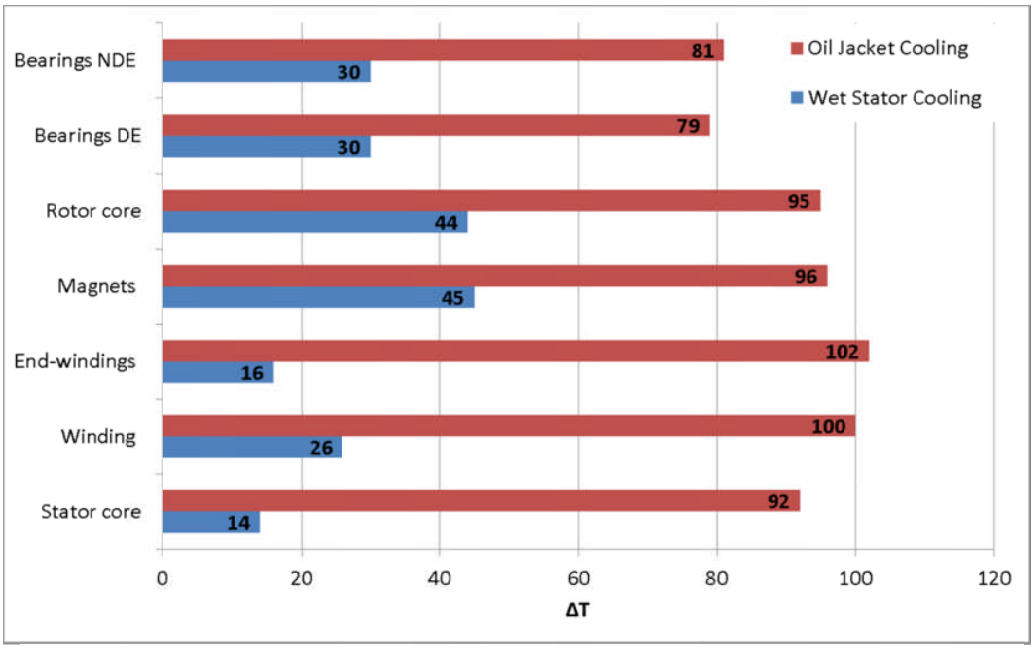



**Figure 7.c: Predicted Temperature Rises Using Different Cooling Options Using MotorCAD Thermal Network (oil inlet temperature: 120 °C)**

Results show that a significant temperature increase is obtained using the Oil Jacket cooling option, which doesn't leave sufficient safety margin. Furthermore if a jacket cooling option is used the oil inlet temperature should not exceed 100°C, whilst if the direct cooling option is used machine components can run well below acceptable limits even if the oil inlet temperature is at the maximum of 120°C.

Higher temperatures in the stator windings also mean high resistive losses, hence lower machine efficiency. By scaling copper losses at the operating mean windings temperature it was estimated that the Oil Jacket configuration leads to an increased power loss of approximately 20%.

Another important aspect is that the Oil Jacket configuration requires a thicker housing in the machine active part to enable the machining of grooves. Using the direct cooling the thickness of the aluminium case is 3 mm, assuming a thickness of at least 6 mm for the Oil Jacket an increase of the mass of about 0.6 kg is necessary; given that two starter generators are used in the aircraft, the overall mass increase is about 1.2 kg.

## 7.3 Testing and Validation

Although the starter generator was designed to run up to 32,000 rpm, the first prototype commissioned was only required to run up to 20,000 rpm. It followed that the machine could not be tested at the operating point used for the design (full power at 32,000 rpm). Several tests were then carried out to validate the thermal and mechanical performance of the machine; these will be described in the following sections.

Before conducting any test, the machine was aligned to the test rig in order to avoid any misalignment between the machine and driving shafts which could lead to excessive vibrations and hence inaccuracies on torque measurements.

### 7.3.1 Validation Machine Thermal Performance

Validation of the machine thermal performance was investigated by carrying out a Short Circuit Test (SC Test). This test consists of short circuiting the machine electrical terminals and spinning the machine using the drive motor; the variation of the magnetic flux induced by the magnets due to the rotation induces a current in the stator windings so it is expected that almost all power losses are due to resistive losses in the windings. The total power loss was calculated by measuring the torque at each operating speed tested; once the estimated mechanical losses (described in Chapters 2 and 4) were deducted from the total power loss, the remaining power was assumed to be generated into the stator (94% copper and 6% stator iron) as advised by the team of electrical designers; finally the stator iron power loss was assumed to be occurring 70% in the teeth and 30 % in the back iron. No rotor losses were assumed for this test. Tests were performed in a speed range between 400 and 12,000 rpm so no high mechanical losses were expected. Table 7.1 lists the machine losses at each operating speed.

| Data collected | | | Losses (W) | | | | | |
|---|---|---|---|---|---|---|---|---|
| **Speed (rpm)** | **Torque (Nm)** | **Total loss (W)** | **Friction** | **Total Stator** | **Copper** | **Total Iron** | **Teeth** | **Back iron** |
| 400 | 22.98 | 962 ±3.4 | 1 | 961 | 904 | 58 | 40 | 17 |
| 800 | 20.31 | 1701 ±6.10 | 1 | 1700 | 1598 | 102 | 71 | 31 |
| 1200 | 16.19 | 2033 ±7.30 | 2 | 2031 | 1910 | 122 | 85 | 37 |
| 1600 | 13.18 | 2208 ±7.90 | 4 | 2204 | 2072 | 132 | 93 | 40 |
| 2000 | 11.14 | 2332 ±8.40 | 5 | 2327 | 2187 | 140 | 98 | 42 |
| 2500 | 9.38 | 2455 ±8.84 | 7 | 2448 | 2302 | 147 | 103 | 44 |
| 3000 | 7.97 | 2502 ±9.01 | 10 | 2492 | 2342 | 149 | 105 | 45 |
| 4000 | 6.29 | 2634 ±9.48 | 15 | 2619 | 2462 | 157 | 110 | 47 |
| 5000 | 5.32 | 2786 ±10.01 | 21 | 2765 | 2599 | 166 | 116 | 50 |
| 8000 | 3.65 | 3060 ±11.00 | 44 | 3016 | 2835 | 181 | 127 | 54 |
| 10000 | 3.05 | 3188 ±11.49 | 63 | 3125 | 2938 | 188 | 131 | 56 |
| 12000 | 2.75 | 3449 ±12.44 | 84 | 3365 | 3163 | 202 | 141 | 61 |

**Table 7.1: Machine Losses Short Circuit Test**

In order to evaluate the performance of the final design other measurements were taken; as described in 6.2.1 temperature measurements were taken in the middle of the coils inside the stator slots in order to identify the winding highest temperature and in the inlet and outlet oil lines, the oil flow rate was also measured. These measurements also allowed the calculation of the oil temperature rise (ΔT) and the heat removed by the oil. All data presented refers to steady state condition. Table 7.2 shows the thermal measurements taken during the test. As can be seen, as power losses increase the oil inlet temperature also increases; this is due to the fact that the oil unit used was not capable of maintaining a constant inlet temperature of 55°C.

| Speed (rpm) | $T_{winding}$ max (°C) ±2.5 | Oil in (°C) ±2.5 | Oil out (°C) ±2.5 | ΔT ±3.5 | Oil flow rate (lt/min) | Heat removed (W) ±1.7k | Total loss measured (W) |
|---|---|---|---|---|---|---|---|
| 400 | 73 | 55.24 | 57.12 | 1.88 | 13.44 ±0.6 | 922 | 962 ±3.4 |
| 800 | 94 | 61.05 | 64.45 | 3.4 | | 1667 | 1701 ±6.10 |
| 1200 | 104 | 64.94 | 69 | 4.06 | | 1990 | 2033 ±7.30 |
| 1600 | 108.5 | 66.65 | 71.04 | 4.39 | | 2151 | 2208 ±7.90 |
| 2000 | 111 | 67.99 | 72.67 | 4.68 | | 2292 | 2332 ±8.40 |
| 2500 | 113.5 | 68.66 | 73.47 | 4.81 | | 2353 | 2455 ±8.84 |
| 3000 | 115.5 | 69.29 | 74.26 | 4.97 | | 2437 | 2502 ±9.01 |
| 4000 | 118 | 69.92 | 75.13 | 5.21 | | 2549 | 2634 ±9.48 |
| 5000 | 119.7 | 70.56 | 75.91 | 5.35 | | 2620 | 2786 ±10.01 |
| 8000 | 125 | 71.8 | 77.6 | 5.8 | | 2841 | 3060 ±11.00 |
| 10000 | 133 | 74.71 | 81.11 | 6.4 | | 3133 | 3188 ±11.49 |
| 12000 | 140 | 77.02 | 84.03 | 7.01 | | 3431 | 3449 ±12.44 |

**Table 7.2: Thermal Measurements Short Circuit Test**

Machine losses, oil inlet temperature and oil flow rate were used as boundary conditions for the thermal models developed. A comparison between the maximum winding temperatures rise recorded experimentally and those obtained analytically and numerically are shown in Figure 7.d. As the data show, a good agreement is achieved. Data are also presented in Table 7.3. Due to the time required by each simulation, only four CFD cases, evenly spread between the lowest and the highest operating speed were run; As a consistent difference between the numerical and analytical model was recorded, these points were considered sufficient.

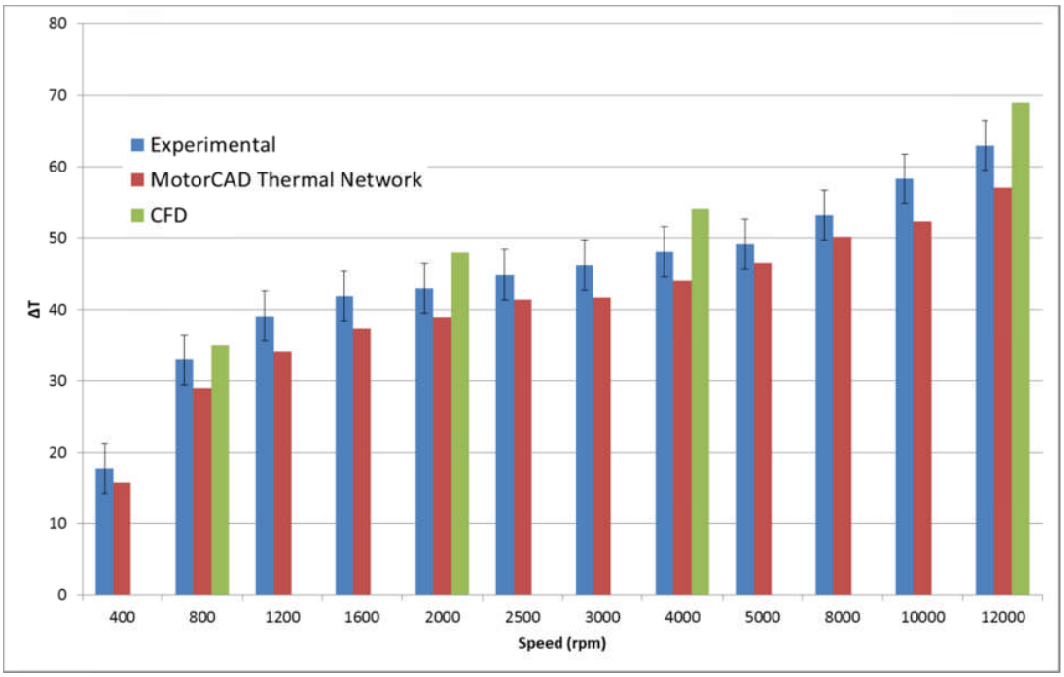



**Figure 7.d: Maximum Windings Temperature rise Short Circuit Test**

| | Maximum Winding Temperature (°C) | | |
|---|---|---|---|
| **Speed (rpm)** | **Measured (±2.5 °C)** | **MotorCAD Thermal Network** | **Numerical Model** |
| 400 | 73 | 71 | |
| 800 | 94 | 90 | 96 |
| 1200 | 104 | 99 | |
| 1600 | 108.5 | 104 | |
| 2000 | 111 | 107 | 116 |
| 2500 | 113.5 | 110 | |
| 3000 | 115.5 | 111 | |
| 4000 | 118 | 114 | 124 |
| 5000 | 119.7 | 117 | |
| 8000 | 125 | 122 | |
| 10000 | 133 | 127 | |
| 12000 | 140 | 134 | 146 |

**Table 7.3: Short Circuit Test Temperatures Comparison**

The performance of the cooling system used was calculated by the percentage of heat removed by the oil; this was based on the oil temperature rise $\Delta T$ and flow rate measured. Overall, according to the experimental data, the oil was capable of dissipating over 95% of the total power loss.

Although in other operating conditions (motoring and generation) the loss distribution will be different it is expected that due to the nature of machine (permanent magnets) most of the power losses will still occur in the stationary components as in the case analysed here; it follows that similar performance are expected.

It can be noted that losses occurring in the stationary components at the design operating point at 32,000 rpm (copper + iron = 1,488 W) are comparable to the 800 rpm operating point of the SC Test (1,700 W). In that case the maximum temperature rise recorded in the windings was about +33 °C; the predictions of the thermal models were between +26 and +30 °C, it follows that predictions can then be considered consistent with experimental data.

### 7.3.2 Validation Mechanical Losses

The prediction of machine mechanical power losses such as bearings friction and windage is a crucial step of the design process. The estimation of the mechanical losses was carried out analytically as described in sections 2.3.4 and 4.4.3.

A No-Load Test was carried out in a sufficiently wide speed range (1,000 – 20,000) validating the analytical predictions. The test consists on driving the starter/generator at different operating speeds by using the drive motor and leaving the test machine terminals in open circuit condition; the torque measured allows the calculation of the total power loss given by mechanical and electromagnetic contributes. Although a good match between experimental and analytical data is shown, it is important to notice that the torque transducer used had an accuracy of 0.12% at the full scale (±300 Nm), meaning ±0.36 Nm. Torques measured during the No-Load Test were in the range 0.1 – 0.6

Nm, in this range the manufacturer could not specify an accuracy; it follows that the author cannot provide a specific degree of accuracy for these measurements. Further investigations are then needed to fully validate the analytical models.

Table 7.4 shows the total power loss calculated based on the torque measured and the loss components estimated. Whilst all mechanical losses were predicted analytically by the author, the electromagnetic component was numerically estimated by electrical team members involved in the project. As can be seen a better agreement between the total estimated loss and the experimental measurements is achieved at operating speeds above 10,000 rpm where the maximum difference achieved is 12% as shown in Table 7.4; as machine designed is targeted for high speed application, predictions can be considered satisfactory. Figure 7.e shows a comparison of the trend of the total power loss measured and estimated.

| | **Power Losses (W)** | | | | | | |
|---|---|---|---|---|---|---|---|
| | **Measured** | **Estimated** | | | | | |
| **Speed (rpm)** | **Total** | **Electro-magnetic** | **DE bearing** | **NDE bearings** | **Windage** | **Total** | **% diff.** |
| 1000 | 13 | 6 | 1 | 0 | 0 | 7 | 46 |
| 2000 | 31 | 15 | 4 | 1 | 0 | 20 | 36 |
| 3000 | 50 | 25 | 7 | 2 | 0 | 35 | 30 |
| 4000 | 68 | 38 | 11 | 4 | 0 | 53 | 22 |
| 5000 | 93 | 52 | 16 | 6 | 0 | 74 | 21 |
| 6000 | 118 | 67 | 20 | 8 | 1 | 96 | 18 |
| 7000 | 141 | 84 | 25 | 10 | 1 | 121 | 14 |
| 8000 | 174 | 102 | 30 | 13 | 2 | 147 | 16 |
| 9000 | 210 | 122 | 35 | 16 | 2 | 175 | 17 |
| 10000 | 250 | 143 | 40 | 20 | 3 | 206 | 18 |
| 11000 | 240 | 165 | 45 | 24 | 4 | 238 | 1 |
| 12000 | 268 | 188 | 51 | 28 | 5 | 272 | 2 |
| 13000 | 315 | 212 | 56 | 33 | 7 | 308 | 2 |

| | | | | | | | |
|---|---|---|---|---|---|---|---|
| 14000 | 385 | 238 | 61 | 39 | 9 | 346 | 10 |
| 15000 | 422 | 265 | 65 | 45 | 11 | 386 | 8 |
| 16000 | 483 | 293 | 70 | 51 | 13 | 428 | 12 |
| 17000 | 508 | 322 | 75 | 58 | 16 | 471 | 7 |
| 18000 | 551 | 353 | 79 | 66 | 19 | 517 | 6 |
| 19000 | 608 | 384 | 84 | 74 | 22 | 564 | 7 |
| 20000 | 652 | 417 | 88 | 83 | 25 | 613 | 6 |

**Table 7.4: Power Losses No-Load Test**

The test was carried out using lubricating oil at a constant temperature of 55°C so it follows that bearings friction losses were calculated at that temperature. Each operating point was run until no variations were identified in the torque readings.

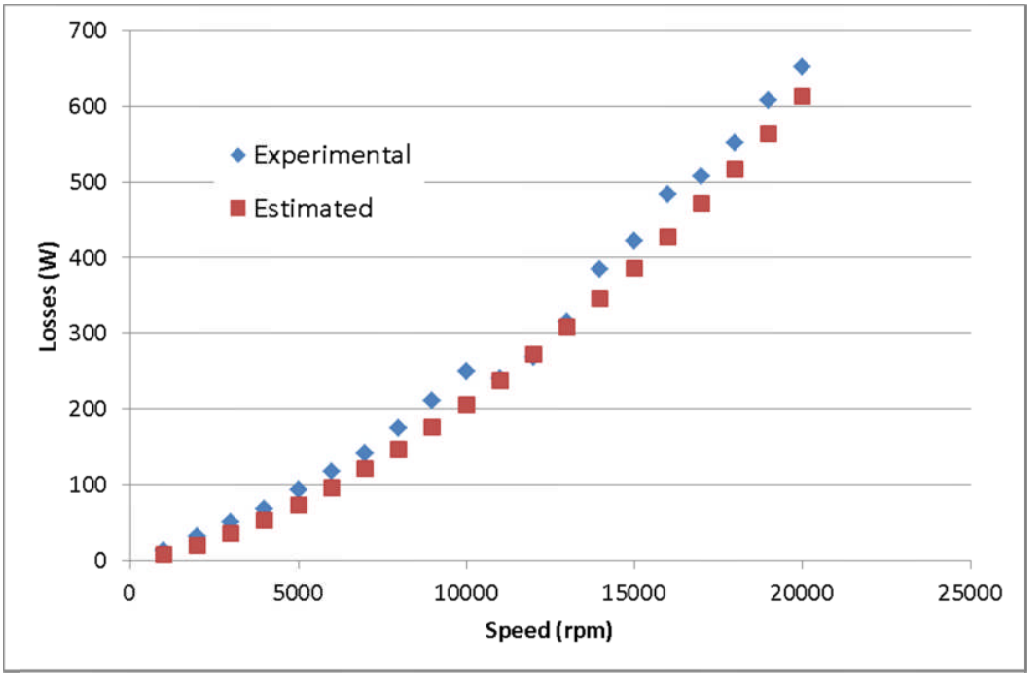



**Figure 7.e: No-Load Losses Trend**

### 7.3.3 Fluid Flow Validation

In order to fully investigate the performance of the cooling configuration the fluid flow and pressure drops across the machine, estimated numerically, were also validated.

As described in the schematic in Chapter 6, pressure measurements were taken at three locations: at the machine oil inlet, machine oil gallery and machine outlet as shown in Figure 6.c and Figure 6.g. Once an oil inlet temperature of 55°C and an oil flow rate of 13.44 ±0.6 lt/min were set the following pressure readings, shown in Table 7.5 were taken.

| **Location** | **Pressure Reading (kPa)** |
|---|---|
| Inlet | 137 ± 2.74 |
| Oil Gallery | 42.3 ± 0.875 |
| Outlet | 0 ± 0.02 |

**Table 7.5: Pressure Readings**

In order to validate the pressure and flow measurements two different cases were studied. The first used a pressure inlet and the second a mass flow rate as boundary conditions

The inlet pressure experimentally measured was used as boundary condition at the main machine inlet in order to investigate the pressure inside the oil gallery and the pressure drop occurring between the inlet and radial jets outlet; as the pressure at the jets outlet was not known an outflow boundary condition was set. Figure 7.f shows the pressure contours computed; as can be seen the pressure drop computed between the inlet and jets outlet is approximately 110 kPa, whilst the pressure inside the gallery, computed on a surface created in the middle of the gallery, was 56 kPa; it follows that the pressure drop across the inlet port was 81 kPa and an oil flow rate of 11.9 lt/min was also computed.

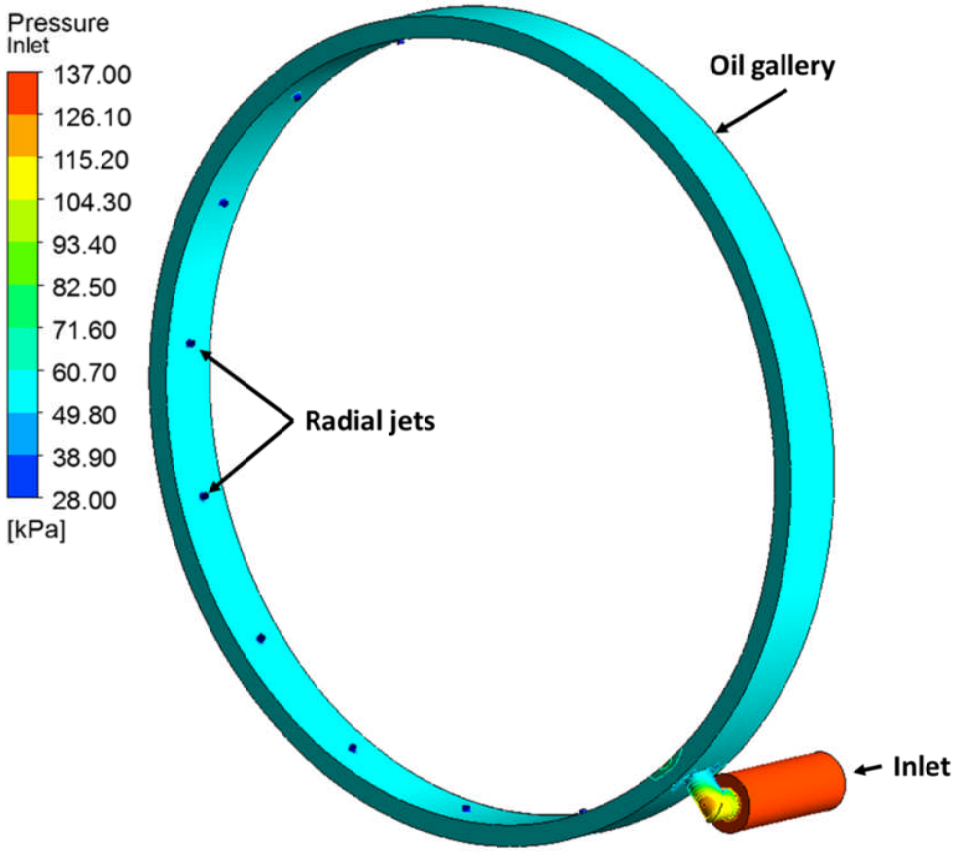



**Figure 7.f: Pressure Contour Inlet Region**

The second case imposed the measured flow rate of 13.44 lt/min as inlet boundary condition rather than pressure, outflow boundary condition was set at the jets outlet. Table 7.6 summarise the input and output data regarding the inlet region domain only; highlighted cells represent data measured experimentally.

| **Boundary condition** | **Pin (kPa)** | **ΔP inlet/gallery (kPa)** | **ΔP inlet/jets outlet (kPa)** | **Flow rate (lt/min)** |
|---|---|---|---|---|
| Pressure | 137 | 81 | 110 | 11.9 |
| Mass flow rate | 165 | 101 | 131 | 13.44 |

**Table 7.6: Inlet Region Data**

The oil pressure drop across the machine stator region was also computed using the 20° machine domain described in section 5.3.5; a mass flow rate

(13.44/18 lt/min) was set as inlet boundary condition. As shown in Figure 7.g a pressure drop of 11 kPa was computed.

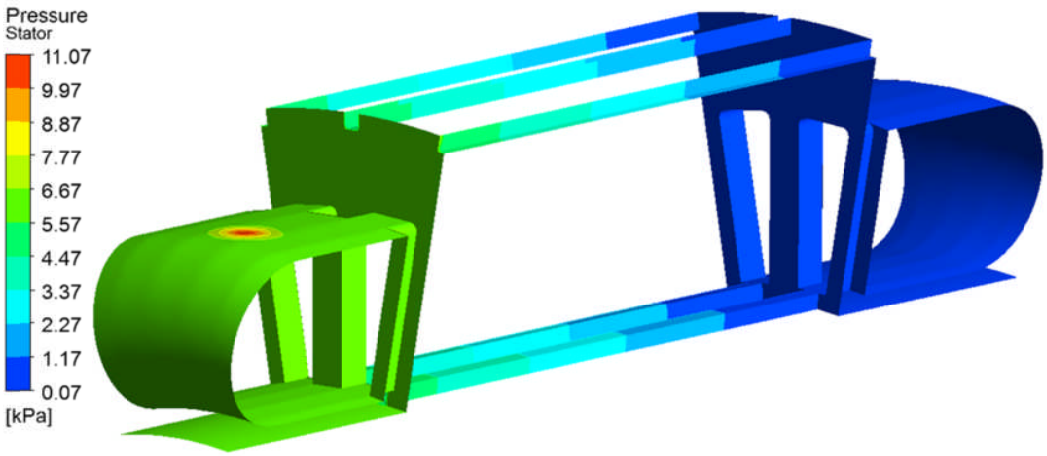



**Figure 7.g: Pressure Contour Stator Region**

By summing the pressure drops between main oil inlet and radial jets outlet computed in the two cases (110 kPa and 131 kPa respectively), with the pressure drop between machine drive-end and outlet (11 kPa) the machine total pressure drop could be calculated; this led to values of 121 kPa and 142 kPa in the first and second case respectively. As the pressure drop measured across the machine was about 137 kPa it can be noted that models built are also capable of resolving the fluid flow and the pressure field with a maximum error of 13%.

## 7.4 Summary

Analytical and numerical simulations allowed the prediction of the performance of the cooling strategy employed by performing conjugate heat transfer analyses and fluid flow analyses. The thermal behaviour of the starter generator was investigated experimentally and data collected used to validate models built. Although full thermal characterisation could not be achieved due limited availability of measuring points and tests performed, data collected were sufficient for identifying the most crucial parameters in the machine such as maximum windings temperature, mechanical friction losses and fluid flow.

Results comparison showed a good agreement between experimental data and predictions. Temperature rise of key components such as stator windings had differences within 10%, friction losses below 10% at speeds above 10,000 rpm and pressure drops were predicted with a maximum difference of 13 %.

The high power density starter/generator was successfully tested up to sufficiently high speeds confirming the effectiveness of the Stator sleeve used for maintaining friction losses within acceptable limits. Tests conducted independently by the customer also confirmed the performance.

# 8 Thermal Modelling and Design Advancements

## 8.1 Introduction

Following the model validation described in Chapter 7 further investigations of alternative configurations to improve the cooling capability of the machine were conducted. As stationary components proved to be the most significant source of heat, attention was focused on these areas, as described in section 8.2. However some consideration on improving the cooling of the rotor was also required and this is described in section 8.3.

Further studies focusing on the simplification of the machine thermal network (described in section 4.3.4), were carried out and these are described in section 8.4.

## 8.2 Enhanced Stator Cooling

As described in Chapter 4 for the first machine prototype small conductors were evenly distributed inside the stator slots. It is expected that for subsequent prototypes eight larger rectangular shaped conductors, shown in Figure 8.a, made of very small copper wires pressed together surrounded by two layers of insulation and a thin layer of aluminium in between them will be used. Eight rectangular conductors will be placed into each slot.

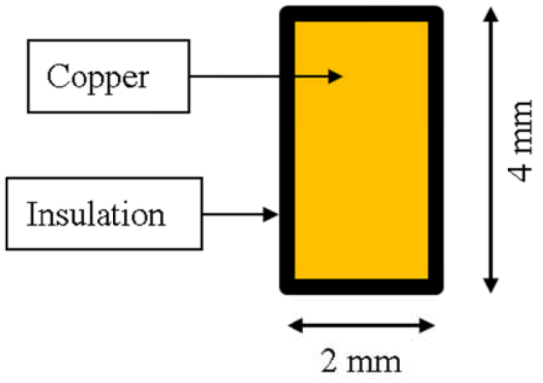



**Figure 8.a: Cross-Section of Rectangular Coils for future Machines**

The placement of rectangular conductors inside the stator slot is no longer straightforward, as when several small round wires are used. As the space

inside the slot is optimised due to the tight winding placement a significant gap inside the slot of about 3 mm by 4.5 mm is left unused as shown in Figure 8.b.

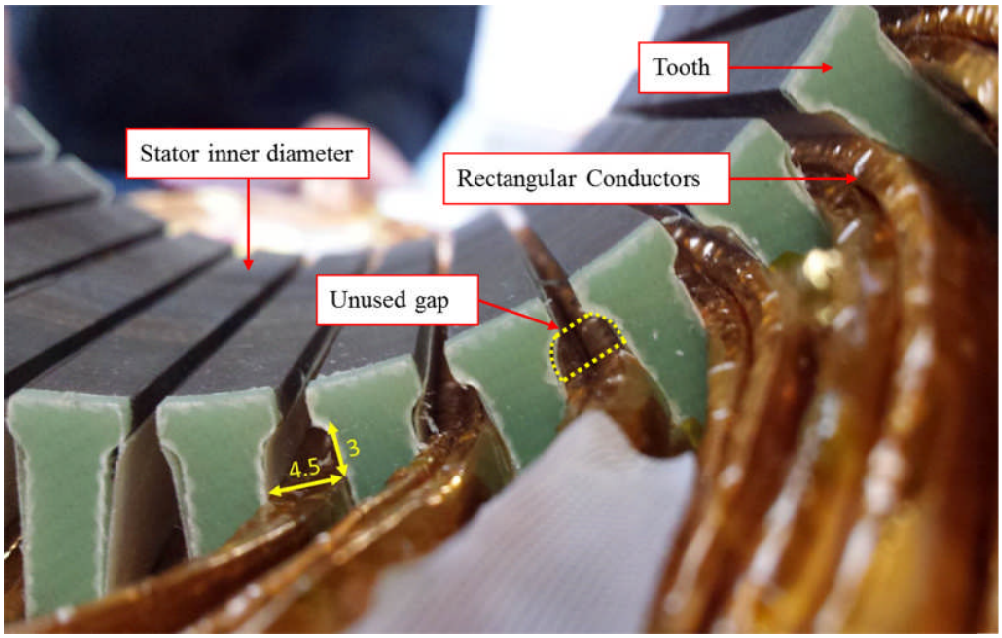



**Figure 8.b: Detail of New Stator Winding (Rectangular Conductors)**

A study was conducted to enhance the cooling of the stator by utilising this gap in different ways. Three different configurations were investigated and these are shown in Figure 8.c.

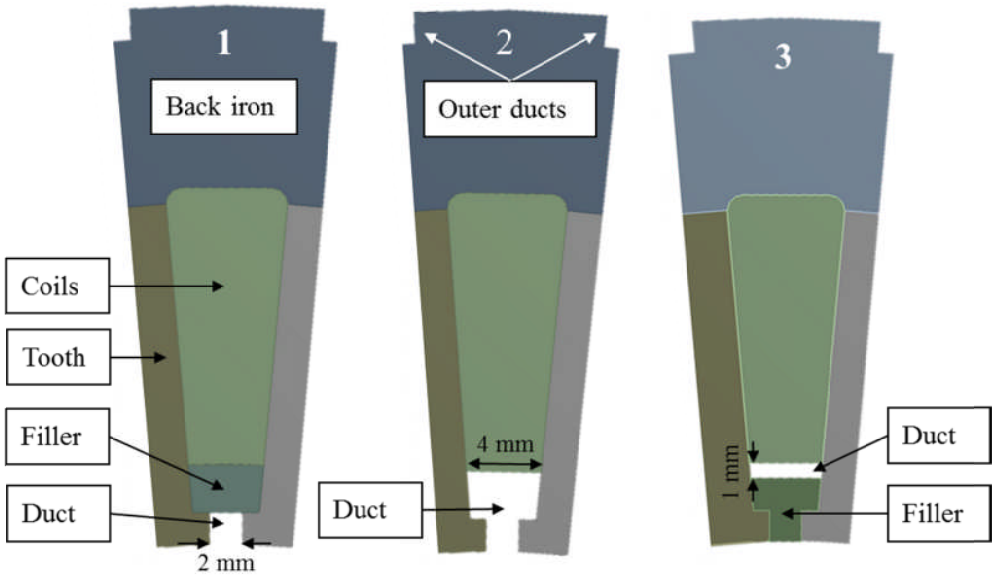



**Figure 8.c: Slot Configurations for stator with rectangular coils**

In option 1 the gap is filled using a filling material such as an insulating resin, in option 2 the whole gap is left open in addition to the duct to let the coolant flow through and finally in option 3 a narrow duct at the bottom of the coils is left and a filler is inserted into the remaining gap.

The performance of each configuration was investigated numerically by using a simplified domain consisting only of the stator lamination and coils inside the slots as shown in Figure 8.d and no fluid region was modelled

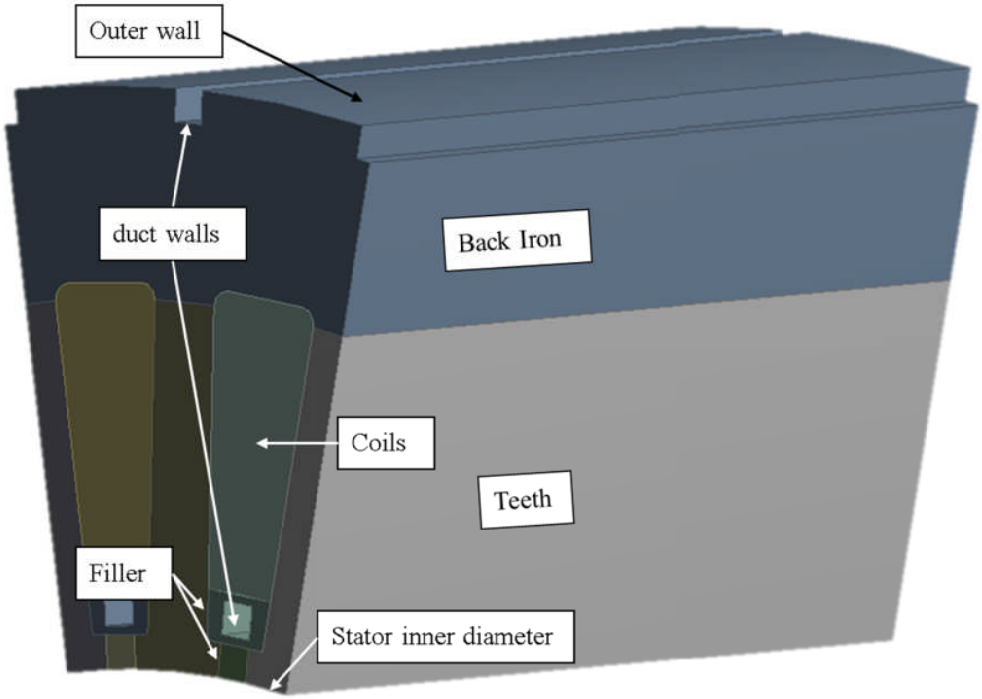



**Figure 8.d: Simplified Stator Model**

The same boundary conditions were assumed for all configurations; ducts walls were given a fixed temperature of 120°C, natural convection was assumed at the outer wall (5 $W/m^2K$ and ambient temperature of 35°C), end walls were assumed adiabatic, 150 W were assumed coming from the stator inner dimeter and finally volumetric heat inputs as described in Chapter 5 were assigned to solid bodies, these are listed in Table 8.1 below. Mesh density, solver setup and level of convergence were kept the same in all cases analysed.

| | Volumetric Heat Input ($W/m^3$) |
|---|---|
| Back Iron | 198,196 |
| Teeth | 703,360 |
| Coils | 1,513,807 |

**Table 8.1: Volumetric Heat Input**

For cases 1 and 3 low conductivity material (0.2 W/mK) such as a typical epoxy used in electrical machines was assumed as filler.

As windings temperatures are a crucial parameters for electrical machines, the assessment of effectiveness of the three cases was based on the maximum and average winding temperatures achieved. Table 8.2 shows the comparison between the three cases analysed.

| | Winding Mean Temperature (°C) | |
|---|---|---|
| | Maximum | Average |
| Case 1 | 145 | 139 |
| Case 2 | 141 | 134 |
| Case 3 | 141 | 134 |

**Table 8.2: Cases Comparison**

Temperature contours are also shown in Figure 8.e.

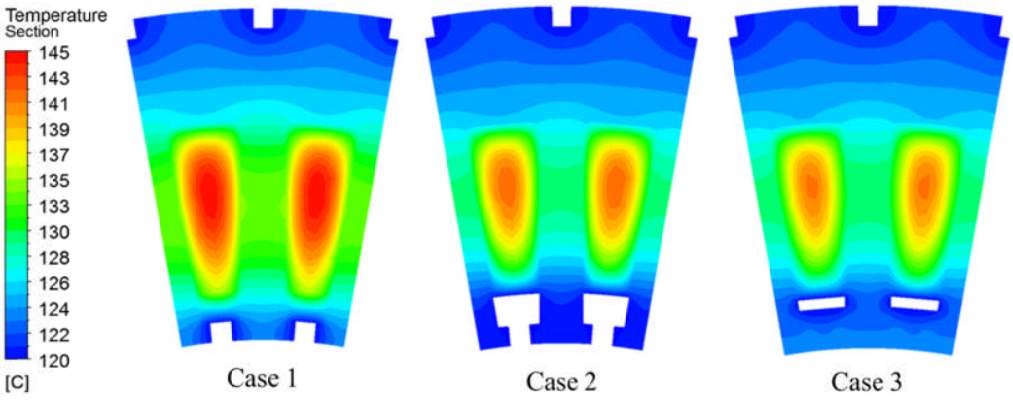



**Figure 8.e: Temperature Contours of Cases Analysed**

Although case 2 provides the same performance as case 3 and also represents the simplest solution from the manufacturing point of view, it should be noted

that the considerably larger inner ducts in case 2 may potentially lead to flow unbalance meaning that no flow or very little amount of oil will flow through the outer ducts. Indeed, assuming no flow through outer ducts the maximum and average windings temperature reached are 160°C and 147°C respectively as shown in Figure 8.f ; which would have a significant impact on the overall machine performance due to higher resistive losses.

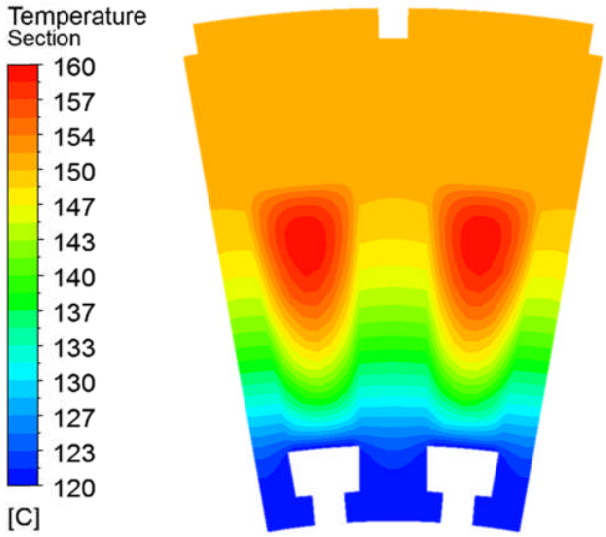



**Figure 8.f: Temperature Contour Case 2 without flow in outer ducts**

Inner ducts created in case 3 have the same cross sectional area of the outer ducts; this will avoid the issue seen in case 2 and at the same time will keep windings at lower temperatures. Case 3 was therefore identified as the optimal configuration.

## 8.3 Considerations on Enhancing Rotor Cooling

As described in Chapter 4 for this machine the design rotor losses represent nearly 20% of the total power loss (2 kW), meaning around 400 W and only 15% of these rotor losses are expected to occur in the rotor active components (magnets, rotor core).

Although losses are not significantly high, keeping magnets operating at temperatures well below their limits is essential to reduce the risk of demagnetisation.

The impossibility of directly cooling the rotor externally by using liquid coolant required further options to be considered.

The first option considered was using fins attached to the inner surfaces of the two end flanges or the inner surface of the stator sleeve in order to increase the heat transfer contact area as shown in Figure 8.g. However due to the compact design insufficient room is available in the rotor end regions for implementing further cooling features; furthermore the presence of more electrically conductive stationary components in the proximity of the magnets can lead to additional power losses due to the eddy currents generated by the magnetic flux variation.

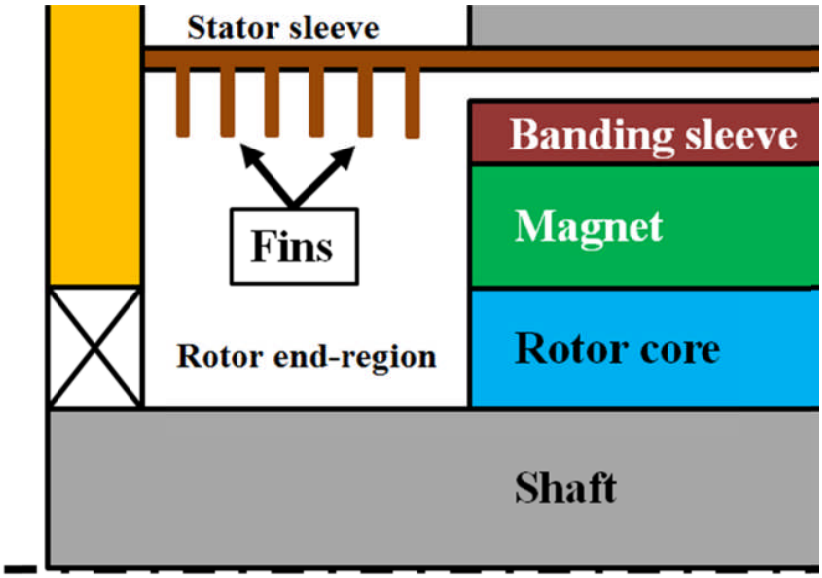



**Figure 8.g: Potential Rotor cooling enhancement**

Further options included cooling the shaft internally; this can be achieved by designing a hollow shaft. The coolant can then flow through the rotor as done in [73] removing most of the heat generated in rotating component. However the main issue related to this solution is the sealing of the shaft rotating at high speeds. An alternative solution of introducing a heat pipe inside the shaft instead of a coolant flowing through has been investigated by numerical and experimental studies in [74], this showed a rotor temperature reduction of

about 15%. As literature shows high speed rotating heat pipes, reaching speeds well above 30,000 rpm are commonly available [75-78].

Shaft cooling can be considered the most promising option; however it is opinion of the author that the introduction of further and significant complexities to the existing design would reduce the overall reliability of the starter generator. As the actual cooling configuration designed was shown to be capable of keeping the rotor well below critical temperatures, in part due to the low heat generated, further improvements may not be required.

## 8.4 Reduced Node Thermal Network

The machine thermal network generated by the author as described in Chapter 4 consisted of about 120 thermal resistances and 66 nodes. For many engineering applications where several thermal networks are integrated together for simulating whole systems, such complex networks may not be suitable and simplifications are required.

Although the complexity of the design requires several thermal resistances for modelling all features a smaller and simpler thermal network can be generated. An integrated function available in MotorCAD allows the simplification of the thermal network initially generated; this is achieved by removing all thermal resistances representing minor thermal paths and keeping all the nodes where heat inputs are applied and a few nodes representing the coolant flow. Figure 8.h shows the simplified thermal network generated, the network consists of 41 thermal resistances and 22 nodes.

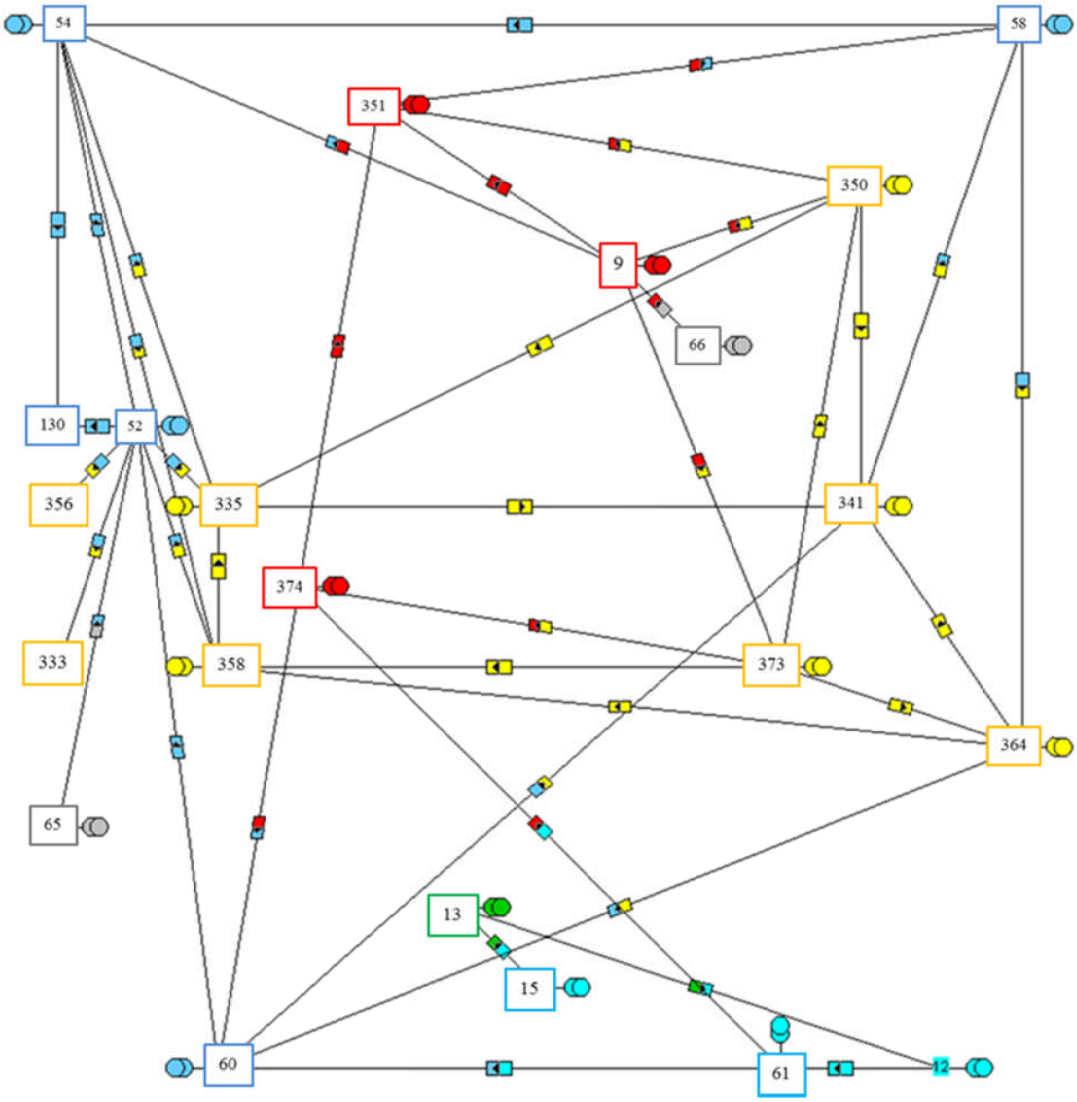



**Figure 8.h: Reduced Thermal Network**

Table 8.3 provides a description of the nodes used and the boundary condition assigned.

| Node | Description | Input parameter |
|---|---|---|
| 130 | Oil inlet | Temperature |
| 335,358,341,364 | End-Windings | 1/6$^{th}$ Copper loss |
| 350, 373 | Windings | 1/4$^{th}$ Copper loss |
| 351, 374 | ½ Stator teeth | 17.5% Stator Core loss (each) |

| | | |
|---|---|---|
| 9 | Stator back iron | 30% Stator Core loss |
| 61, 12 | Airgap | 50% Windage (each) |
| 65 | Drive End (DE) bearing | DE bearing loss deducted of 30W |
| 66 | Non Drive End (NDE) bearing | NDE bearing loss deducted of 90W |
| 13 | Magnet | Magnet loss |
| 15 | Rotor core | Rotor core loss |
| 60 | Axial stator ducts | N/A |
| 58 | Oil outlet | N/A |
| 333, 356 | End-Windings outer surface | N/A |
| 54, 52 | Fluid flow | N/A |

**Table 8.3 Nodes List**

The list of the thermal resistances used and their value is shown in Table 8.4; subscripts represent the nodes the resistances are linked to.

| **Resistance** | **Value [°K/W]** |
|---|---|
| $R_{54_58}$ | 0.0034 |
| $R_{54_9}$ | 0.51 |
| $R_{54_335}$ | 0.05 |
| $R_{54_358}$ | 0.21 |
| $R_{54_52}$ | 0.71 |
| $R_{54_130}$ | 0.0034 |
| $R_{52_356}$ | 0.12 |
| $R_{52_333}$ | 0.12 |
| $R_{52_65}$ | 0.84 |
| $R_{52_130}$ | 0.0039 |
| $R_{52_60}$ | 0.0039 |
| $R_{52_358}$ | 0.061 |

| | |
|---|---|
| $R_{52_335}$ | 0.43 |
| $R_{335_350}$ | 0.067 |
| $R_{335_341}$ | 0.29 |
| $R_{358_373}$ | 0.067 |
| $R_{358_364}$ | 0.29 |
| $R_{358_335}$ | 0.036 |
| $R_{60_374}$ | 0.11 |
| $R_{60_341}$ | 1.22 |
| $R_{60_364}$ | 0.1 |
| $R_{60_61}$ | 0.21 |
| $R_{58_351}$ | 0.027 |
| $R_{58_66}$ | 0.65 |
| $R_{58_341}$ | 0.061 |
| $R_{58_364}$ | 0.26 |
| $R_{351_350}$ | 0.02 |
| $R_{351_9}$ | 0.014 |
| $R_{351_374}$ | 0.037 |
| $R_{374_373}$ | 0.02 |
| $R_{374_61}$ | 0.11 |
| $R_{350_341}$ | 0.067 |
| $R_{350_9}$ | 0.14 |
| $R_{350_373}$ | 0.22 |
| $R_{364_341}$ | 0.041 |
| $R_{364_373}$ | 0.067 |
| $R_{373_9}$ | 0.68 |
| $R_{66_9}$ | 0.64 |
| $R_{12_61}$ | 0.24 |
| $R_{12_13}$ | 0.2 |
| $R_{13_15}$ | 0.02 |

**Table 8.4: List of Thermal Resistances**

The accuracy of the reduced thermal network was analysed by comparing machine temperatures rise predicted, as shown in Figure 8.i. The results show that the reduced thermal network is in a good agreement with the prediction of the temperatures of stationary components whilst a more significant difference, up to the 25%, can be noted in the rotational components as very few nodes were used in that region. However in order to fully investigate the accuracy of the model thermal measurements in rotor components would be required.

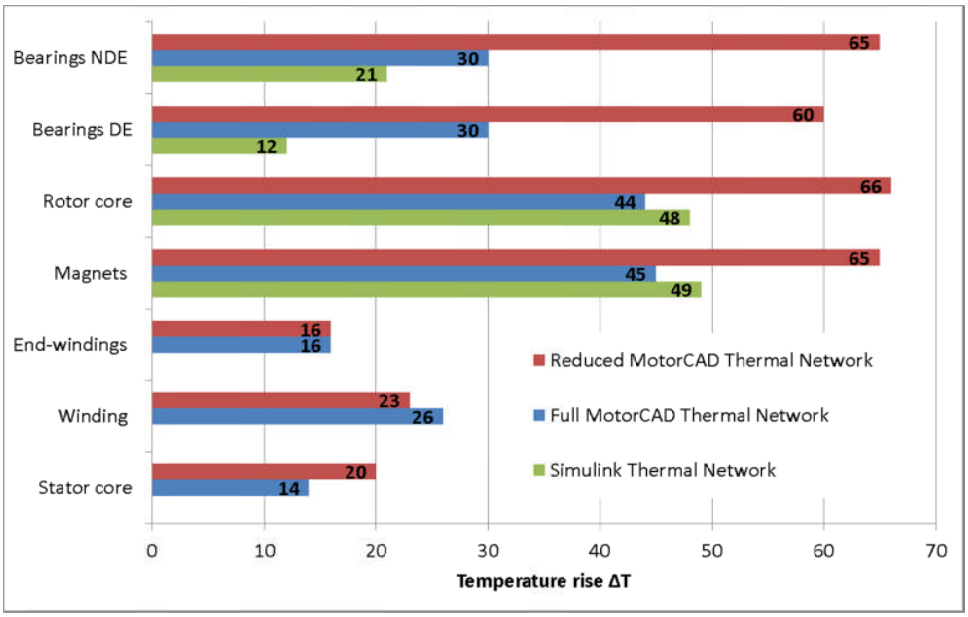



**Figure 8.i: Models comparison**

## 8.5 Summary

The use of a different type of coils in subsequent machine prototypes made necessary the identification of an alternative ducts configuration capable of maximising the effectiveness of the inner layer of ducts. Given the significant airgap available inside the slot several alternative options were considered; the optimal solution identified consisted on a narrow duct located just below the coils. In order to maintain an even flow distribution between outer and inner layer of ducts the cross-sectional area of these new ducts was kept the same as in the original design; this was achieved by filling the remaining gaps with an electrically non-conductive material commonly used in stator slots. Although

equivalent performance can be achieved by using the all available gap for the oil flow, the significantly bigger cross-sectional area of the inner ducts can potentially lead to flow unbalance so no oil would flow in the outer ducts; as numerical predictions shown this can cause the coil temperatures to be 10% higher and thus the overall machine performance can be negatively affected.

The high speed of the application and the complexity of the design did not allow any direct cooling of rotational surfaces; for these reasons some alternative cooling options were discussed in this chapter. The options considered require the use of an internally cooled shaft; this can be achieved by using a hollow shaft where the coolant can flow or by using heat pipes inside the shaft. The use of a hollow shaft would introduce further and significant complexities on the design as the sealing should be effective up to very high speeds; it follows that the use of heat pipes, consisting of a totally enclosed system can be optimal for this application.

Although the thermal network developed for the starter/generator can provide detailed information about the temperature field, the large amount of thermal elements such as nodes and resistances make the network unsuitable for system integration. In this chapter a reduced thermal network, based on the initial full network, was created; thermal resistances were reduced from 120 to 41 whilst nodes from 66 to 22. The analysis of the performance showed a good agreement between the two networks especially in stationary components; more significant differences were seen in active rotational components (10%) and bearings chambers (20%).

# 9 Conclusions and Recommendations

The growing demand for small and lightweight high power starting/generation systems for aerospace applications has led to the development of high speed and high power density machine designs.

The necessity for highly reliable and efficient systems requires a careful thermal management capable of maximising the overall machine performance by reducing the temperature dependent losses and preserving the integrity of machine components by keeping operating temperatures within acceptable limits. These aspects make thermal management a crucial step of electrical machines design process.

This work has analysed, designed, commissioned and validated the performance of a novel cooling system for an innovative for a high speed, three-phase synchronous permanent magnet machine designed for an aero-engine starter/generator; this was done by:

1. Critically analysing the nature and distribution of heat sources within the permanent magnet machine used.

2. Investigating existing cooling strategies adopted for electrical machines, particularly for aerospace application.

3. Developing an alternative cooling strategy capable of maximising the overall machine performance.

4. Investigating and optimising the performance of the thermal design developed by using analytical and numerical models.

5. Experimentally validating the thermal models developed.

## 9.1 Cooling Design Conclusions

Geometrical limitations leading to a small machine requires a high power density. Although high efficiencies (typically above 95%) can now be reached

in modern machine designs, due the high power ratings a significant amount of heat is generated.

As conventional air cooled designs require large surfaces for heat dissipation direct liquid cooling is the only cooling option capable of significantly increase the power density and maximise the overall efficiency.

Due to the high speed of the machine designed (up to 32,000 rpm) the use of a liquid coolant over rotating components leads to an excessive power loss; furthermore as 80% of total power loss (~2 kW) takes place in stationary components such as windings and laminations a direct liquid cooling of this area is then required. This is achieved by flooding the stator region by using a retaining and electrically non-conductive stator sleeve isolating the rotor region; ducts created through the stator core along the stator outer diameter and slots along the inner diameter let the coolant flow through the machine.

Compared with indirect cooling, where the coolant only flows in the frame surrounding the machine, the direct liquid cooling leads to the reduction of temperature dependent losses of approximately 20%.It also leads to reduce the overall machine weight due to thinner housing required and a weight save of about 1 kg (representing the 10% of machine total mass) was achieved in this machine design.

Temperature rise of critical components such as windings and magnets is 25 and 50 degrees respect the oil inlet temperature.

In order to further reduce the impact of the machine weight on the aircraft synthetic oil commonly used on board for gears lubrication is employed as primary coolant.

## 9.2 Thermal Modelling Conclusions

### 9.2.1 Analytical Thermal Modelling

The lumped parameter thermal network method used for the thermal modelling of electrical machines allows quick analyses of the heat transfer problems with limited computational efforts; complex geometries and phenomena can be reduced to relatively simple networks of thermal resistances.

When solving conduction heat transfer problems between homogeneous and isotropic materials few nodes are sufficient for identifying temperature fields; however if conjugate heat transfer analyses are carried out and anisotropic materials need to be modelled, the complexity of the network can considerably increase. Furthermore if complex fluid flows are involved the analytical approach only is no longer sufficient as heat transfer coefficients cannot be calculated easily.

The use of numerical methods for the investigation of the fluid flow helps improving the accuracy of the analytical models so a combined use of the two modelling approaches lead to successfully describe the thermal behaviour of the electrical machines.

The main advantage of using this modelling approach is the fast calculation speed; indeed once the model is set up several scenarios can be investigated and cases can be compared within few minutes.

### 9.2.2 Numerical Thermal Modelling

Computational Fluid Dynamics provides more detailed modelling of the temperatures field within the machine and also it is capable of modelling complex fluid flows inside the generator.

Due to axisymmetric nature of the machine design a 20° sector model is able to accurately model the heat transfer and fluid flow, resulting in much faster computations.

Local investigation of machine critical areas allows the identification of optimal mesh densities; also it has a significant impact on the solution accuracy and calculation of full machine model.

The discretisation of the airgap is critical for a correct prediction of the fluid flow and friction loss; for this machine design 90 equal divisions are used along the axial direction whilst 26 cells, finer near walls and coarser in the middle of the airgap are used along the radial direction.

The reduction of the computational cost is also achieved by setting up a CAD model suitable for a CFD simulation. This implies the creation of simplified 3D models of machine components which do not include features like screws, threaded holes, small surfaces. Very complex components such as windings and bearing chambers are modelled as bulk solids and overall thermal properties are used. In order to improve the quality of the mesh and hence of the solution further simplification is required; the fluid and solid zones are split into sub-domain having more regular geometrical features. Mesh optimisation process leads to a reduction up to 20% in the full 360° machine model.

## 9.3 Novelty in this Thesis

- Use of lumped parameter thermal network (LPTN) for the thermal modelling of full high speed machine with two different fluid paths within the same network.
- Use of CFD for conjugate heat transfer analysis of full 3D machine design including two fluid domains and rotation up to 32,000 rpm.
- CFD investigation of stator end-regions for an accurate prediction of heat transfer coefficients and for the optimisation of mesh density.
- CFD investigation of airgap domain for the determination of optimal mesh density suitable for high rotational speeds and for an accurate prediction of windage loss due to viscous friction.
- Use of multiple turbulence models within the same fluid domain.

- Development of a detailed thermal network of bearing chambers for the investigation of conductive and convective heat transfer and overall thermal properties.
- Simultaneous and combined use of numerical and analytical models for accurate understanding and prediction of machine thermal behaviour.

## 9.4 Suggestions for Future Works

- The composition of electrical windings, consisting of copper and insulation makes the prediction of the thermal properties uncertain, for this reason experimental measurement would be necessary.
- Thermal measurements inside bearing chambers for the validation of the thermal network developed.
- Use of infrared fibre-optic sensors for measuring temperature of rotor core.
- Use of additional measurement points in the stator lamination and windings for more detailed information about temperature distribution.
- Torque measurements using non-magnetic rotor for investigating friction losses in more detail.
- Torque measurements using a torque sensor with smaller measuring range for further investigation of windage losses.

# *References*


1. Wenping, C., et al., *Overview of Electric Motor Technologies Used for More Electric Aircraft (MEA).* Industrial Electronics, IEEE Transactions on, 2012. 59(9): p. 3523-3531.
2. Boglietti, A., Cavagnino, A., Tenconi, A., Vaschetto, S. *The safety critical electric machines and drives in the more electric aircraft: A survey*. in *Industrial Electronics, 2009. IECON '09. 35th Annual Conference of IEEE*. 2009.
3. Naayagi, R.T. *A review of more electric aircraft technology*. in *Energy Efficient Technologies for Sustainability (ICEETS), 2013 International Conference on*. 2013.
4. Pyrhonen, J., T. Jokinen, V. Hrabovcová, *Design of Rotating Electrical Machines*2008, Chichester, West Sussex, United Kingdom: Wiley.
5. Stone G., C.I., Boulter E., Dhirani H., *Electrical Insulation for Rotating Machines: Design, Evaluation, Aging, Testing, and Repair, 2nd Edition*2014: Wiley-IEEE Press.
6. Hughes, A., *Electric Motors and Drives: Fundamentals, Types and Applications*. third ed2006: Elsevier Ltd.
7. Boglietti, A., Cavagnino, A., Staton, D., Shanel, M., Mueller, M., Mejuto, C., *Evolution and Modern Approaches for Thermal Analysis of Electrical Machines.* Industrial Electronics, IEEE Transactions on, 2009. 56(3): p. 871-882.
8. Bejan, A., *Heat Transfer*: Wiley 1993.
9. Hamid A. Toliyat, G.B.K., *Handbook of Electric Motors*. Second ed, New York: Marcel Dekker, Inc.
10. Staton, D., A. Boglietti, and A. Cavagnino, *Solving the More Difficult Aspects of Electric Motor Thermal Analysis in Small and Medium Size Industrial Induction Motors.* Energy Conversion, IEEE Transactions on, 2005. **20**(3): p. 620-628.
11. Boglietti, A., A. Cavagnino, and D. Staton, *Determination of Critical Parameters in Electrical Machine Thermal Models.* Industry Applications, IEEE Transactions on, 2008. 44(4): p. 1150-1159.
12. F. Kreith, R.M., Mark Bohn, *Principles of Heat Transfer*. 7th ed: Cengage Learning, 2011.
13. Mugglestone, J., *End Region Cooling in an Electric Motor*, 1998, The University of Nottingham.
14. Boglietti, A., Cavagnino, A., Staton, D. A., Popescu, M., Cossar, C., McGilp, M. I. *End Space Heat Transfer Coefficient Determination for Different Induction Motor Enclosure Types*. in *Industry Applications Society Annual Meeting, 2008. IAS '08. IEEE*. 2008.
15. Micallef, C., *End Winding cooling in electric machines*, 2007, The University of Nottingham.
16. A. Haumer, C.K., H. Kapeller, T. Bauml, J.V. Gragger, *The Advanced Machines Library: Loss Models for Electric Machines.* 2009.
17. Mlot, A., Korkosz, M., Grodzki, P., Lukaniszyn, M.,, *Analysis of The Proximity and Skin effects on Copper Loss in a Stator Core.* Archives of Electrical Engineering, 2014. 63(2): p. 221-225.

18. Atallah, K., Z.Q. Zhu, and D. Howe, *An improved method for predicting iron losses in brushless permanent magnet DC drives.* Magnetics, IEEE Transactions on, 1992. 28(5): p. 2997-2999.
19. Zivotic-Kukolj, V., W.L. Soong, and N. Ertugrul. *Iron loss reduction in an interior PM automotive alternator*. in *Industry Applications Conference, 2005. Fourtieth IAS Annual Meeting. Conference Record of the 2005*. 2005.
20. Fiorillo, F.a.R., AM, *Rotational and Alternating Energy Loss vs Magnetizing Frequency in Si-Fe Laminations.* Journal of Magnetisation and Magnetic Materials, 1990. 83: p. 402-404.
21. Krings, A., *Iron Losses in Electrical Machines - Influence of Material Properties, Manufacturing Processes and Inverter Operation*, 2014, KTH School of Electrical Engineering: Sweden.
22. Mi, C.C., G.R. Slemon, and R. Bonert, *Minimization of iron losses of permanent magnet synchronous machines.* Energy Conversion, IEEE Transactions on, 2005. 20(1): p. 121-127.
23. Paulides, J.J.H., G.W. Jewell, and D. Howe, *An evaluation of alternative stator lamination materials for a high-speed, 1.5 MW, permanent magnet generator.* Magnetics, IEEE Transactions on, 2004. 40(4): p. 2041-2043.
24. Polinder, H. and M.J. Hoeijmakers, *Eddy-current losses in the segmented surface-mounted magnets of a.* Electric Power Applications, IEE Proceedings - , 1999. 146(3): p. 261-266.
25. Ishak, D., Z.Q. Zhu, and D. Howe, *Eddy-current loss in the rotor magnets of permanent-magnet brushless machines having a fractional number of slots per pole.* Magnetics, IEEE Transactions on, 2005. 41(9): p. 2462-2469.
26. Saari, J., *Thermal Analysis of High-Speed Induction Machines*, 1998, Acta Polytechnica Scandinavica: Helsinki.
27. Dorrell, D.G., Staton, D. A., Kahout, J., Hawkins, D.,McGilp, M. I. *Linked Electromagnetic and Thermal Modelling of a Permanent Magnet Motor*. in *Power Electronics, Machines and Drives, 2006. The 3rd IET International Conference on*. 2006.
28. Boglietti, A., A. Cavagnino, and D.A. Staton. *TEFC induction motors thermal models: a parameter sensitivity analysis*. in *Industry Applications Conference, 2004. 39th IAS Annual Meeting. Conference Record of the 2004 IEEE*. 2004.
29. Deaconu, D.I., et al. *Thermal study of induction machine using Motor-CAD*. in *Electrical and Electronics Engineering (ISEEE), 2010 3rd International Symposium on*. 2010.
30. Mellor, P.H., D. Roberts, and D.R. Turner, *Lumped parameter thermal model for electrical machines of TEFC design.* Electric Power Applications, IEE Proceedings B, 1991. 138(5): p. 205-218.
31. Okoro, O.I., B. Weidemann, and O. Ojo. *An efficient thermal model for induction machines*. in *Industry Applications Conference, 2004. 39th IAS Annual Meeting. Conference Record of the 2004 IEEE*. 2004.
32. D. Staton, S.J.P., D. Lampard, *"Recent Advancement in the Thermal Design of Electric Motors".* SMMA 2001 Fall Technical Con., Durham. North Carolina, 3-5 Oct. 2001.

33. Gilson, G.M., et al. *A combined electromagnetic and thermal optimisation of an aerospace electric motor*. in *Electrical Machines (ICEM), 2010 XIX International Conference on*. 2010.
34. Wenying, J. and T.M. Jahns. *Coupled electromagnetic/thermal machine design optimization based on finite element analysis with application of artificial neural network*. in *Energy Conversion Congress and Exposition (ECCE), 2014 IEEE*. 2014.
35. H. K. Versteeg, W.M., *An Introduction to Computationa Fluid Dynamics, the Finite Volume Method*. Second ed: Pearson.
36. *www.ansys.com*.
37. Gerada, D., et al., *High-Speed Electrical Machines: Technologies, Trends, and Developments.* Industrial Electronics, IEEE Transactions on, 2014. 61(6): p. 2946-2959.
38. Zwyssig, C., S.D. Round, and J.W. Kolar, *An Ultrahigh-Speed, Low Power Electrical Drive System.* Industrial Electronics, IEEE Transactions on, 2008. 55(2): p. 577-585.
39. Borisavljevic, A., et al. *Motor drive for a novel high-speed micro-milling spindle*. in *Advanced Intelligent Mechatronics, 2009. AIM 2009. IEEE/ASME International Conference on*. 2009.
40. Gerada, D., et al. *Electrical machines for high speed applications with a wide constant-power region requirement*. in *Electrical Machines and Systems (ICEMS), 2011 International Conference on*. 2011.
41. Gerada, D., et al., *Design Aspects of High-Speed High-Power-Density Laminated-Rotor Induction Machines.* Industrial Electronics, IEEE Transactions on, 2011. 58(9): p. 4039-4047.
42. Yu, W., et al. *Research of novel water cooling jacket for explosion-proof motor*. in *Electrical Machines and Systems (ICEMS), 2013 International Conference on*. 2013.
43. Ponomarev, P., M. Polikarpova, and J. Pyrhonen. *Thermal modeling of directly-oil-cooled permanent magnet synchronous machine*. in *Electrical Machines (ICEM), 2012 XXth International Conference on*. 2012.
44. Li, Z., et al. *Study on spraying evaporative cooling technology for the large electrical machine*. in *Electrical Machines and Systems, 2009. ICEMS 2009. International Conference on*. 2009.
45. Tüysüz, A.S., M. Zwyssig, C. Kolar, J. *Advanced Cooling Concepts for Ultra-High-Speed Machines*. in *Proceedings of the 9th International Conference on Power Electronics (ECCE Asia 2015)*. 2015. Seoul, South Korea: IEEE.
46. P. deBock, B.G., *Thermal Challenges in Today's Commercial and Military Aviation.* Electronics Cooling, March 2011: p. 16-21.
47. Rolls-Royce, *The Jet Engine*. fifth ed1986, Derby, England: The Technical Publications Department.
48. Veinott, C.G., *Effect of Altitude on Ventilation and Rating of Aircraft Electric Machines.* American Institute of Electrical Engineers, Transactions of the, 1946. 65(2): p. 84-90.
49. Belady, C.L. *Design considerations for air cooling electronic systems in high altitude conditions*. in *Semiconductor Thermal Measurement and*

*Management Symposium, 1996. SEMI-THERM XII. Proceedings., Twelfth Annual IEEE*. 1996.
50. *US Standard Atmosphere*, 1976.
51. Turns, S.R., *An Introduction to Combustion. Concepts and Applications*, McGraw-Hill, Editor 2012: USA.
52. Streinfinger, H., *Fuel/Oil System Thermal Management in Aircraft Turbine Engine*, in *Design Principles and Methods for Aircraft Gas Turbine Engine*1998: Toulouse, France.
53. Sugden, G.B., *Oil-cooled a.c. generators for aircraft - present trends.* Students' Quarterly Journal, 1970. 40(160): p. 128-133.
54. Streifinger, H., *Fuel/Oil System Thermal Management in Aircraft Turbine Engines*, in *Design Principles and Methods for Aircraft Gas Turbine Engines*1998: Toulouse.
55. Polikarpova, M., *Liquid Cooling Solutions for Rotating Permanent Magnet Synchronous Machines*, 2014, Lappeenranta University of Technology: Finland.
56. K. Naresh Kumar, M.P.k., V. Krishna, D. Srinivasa Rao, *Experimental Investigation on Mechanical Properties of Coal Ash Reinforced Glass Fiber Polymer Matrix Composites* International Journal of Emerging Technology and Advanced Engineering, 2013. 3(8).
57. Davin, T., Pellè, J., Harmand, S., Yu, R., *Experimental study of oil cooling systems for electric motors.* Applied Thermal Engineering, 2014. 71(1): p. 607.
58. Simpson, N., R. Wrobel, and P.H. Mellor, *Estimation of Equivalent Thermal Parameters of Impregnated Electrical Windings.* Industry Applications, IEEE Transactions on, 2013. 49(6): p. 2505-2515.
59. Bossmanns, B. and J.F. Tu, *A thermal model for high speed motorized spindles.* International Journal of Machine Tools and Manufacture, 1999. 39(9): p. 1345-1366.
60. Nakajima, K., *Thermal Contact Resistance Beetween Balls and Rings of a Bearing Under Axial, Radial and Combined Loads.* Journal of Thermophysics and Heat Transfer, 1998. 9: p. 88-95.
61. Takeuchi, R., Eby, A., Blake, A., Demsky, M., Dickey, T. *Influence of Oil Lubrication on Spacecraft Bearing Thermal Conductance*. in *38th Aerospace Mechanisms Symposium*. 2006. Langley Research Center.
62. Takeuchi, R., Frantz, P., Hilton, M. . *Observations of Spacecraft Bearing Lubricant Redistribution Based on Thermal Conductance Measurements*. in *42nd Aerospace Mechanisms Symposium*. 2014. NASA Goddard Space Flight Center.
63. Glahn, A., Wittig, S., *Two-Phase Air/Oil Flow in Aero-Engine Bearing Chambers – Assessment of an Analytical Prediction Method for the Internal Wall Heat Transfer.* International Journal of Rotating Machinery, 1999. 5(155-165).
64. Busam, S., Glahn, A., Wittig, S., *Internal Bearing Chamber Wall Heat Transfer as a Function of Operating Conditions and Chamber Geometry.* Journal of Engineering for Gas Turbines and Power, 2000. 122(2): p. 314-320.

65. Brändlein, J., Eschmann, P,. Hasbargen, L., Weigand, K., *Ball and Roller Bearings: Theory, Design and Application, 3rd Edition*1999: Wiley.
66. SKF, *Rolling Bearings*, 2012.
67. Fakhfakh, M.A., et al., *Thermal Analysis of a Permanent Magnet Synchronous Motor for Electric Vehicles.* Journal of Asian Electric Vehicles, 2008. 6(2): p. 1145-1151.
68. Demetriades, G.D., et al., *A Real-Time Thermal Model of a Permanent-Magnet Synchronous Motor.* Power Electronics, IEEE Transactions on, 2010. 25(2): p. 463-474.
69. Connor, P.H., *Computational Fluid Dynamics Modelling of a Synchronous Electric Generator*, 2013, University of Nottingham.
70. Shanel, M., *Investigation of Rotor Cooling in Salient Pole Electrical Machines*, 2002: University of Nottingham.
71. Becker KM, K.J., *Measurements of Diabatic Flow in an Annulus with an Inner Rotating Cylinder.* Journal of Heat Transfer, 1962.
72. Kleine S, M.F., *Descibing uncertainties in single-sample experiments.* 1953. Mechanical Engineering.
73. Lapkov, A.S. and A.M. Litvinenko, *Analysis of effeciency of cooling system of hollow-shaft automotive alternator.* Russian Electrical Engineering, 2010. 81(10): p. 554-558.
74. Vlach, R., *Computational And Experimental Modelling of DC Machine Cooling by Heat Pipe*, in *6th ASME/WSEAS International Conference on Heat Transfer, Thermal Engineering and Enviroment*2008: Greece.
75. Streby, M.A., et al. *Design and testing of a high speed rotating heat pipe*. in *Energy Conversion Engineering Conference, 1996. IECEC 96., Proceedings of the 31st Intersociety*. 1996.
76. Hashimoto, R., Mizuta, K., Itani, H., Kura, K., Takahashi, Y., *Heat Transport Performance of Rotating Heat Pipes Installed in High Speed Spindles*, 1996, Mitsubishi Heavy Industries Ltd.
77. Ponnappan, R.a.L., J., *Rotating Heat Pipe for High Speed Motor/Generator Cooling.* Journal of Aerospace - V107-1, 1998.
78. Ponnappan, R., He, Q., Leland, J., *Test Results of Water and Methanol High-Speed Rotating Heat Pipes.* Journal of Thermophysics and Heat Transfer, 1998.
79. Andersson, B., *Lumped Parameter Thermal Modelling of Electric Machines, Analysis of an Interior Permanent Magnet Synchronous Machine for Vehicle Applications*, in *Department of Energy and Environment*2013, Chalmers University of Technology: Sweden.
80. Pal, S.K., *Heat Transfer in Electrical Machines - A critical machines*1987: ERA Technology LTD.
81. Chin Hong, L., *Thermal Modelling of the Ventilation and Cooling inside Axial Flux Permanent Magnet Generators* in *School of Engineering and Computer Science* 2010, Durham University, UK.
82. Wrobel, R. and P.H. Mellor, *A General Cuboidal Element for Three-Dimensional Thermal Modelling.* Magnetics, IEEE Transactions on, 2010. 46(8): p. 3197-3200.

83. Bianchi, N., Barcaro, M., Bolognani, S., *Electromagnetic and Thermal Analysis of Permanent Magnet Synchronous Machines*, in *Finite Element Analysis - From Biomedical Applications to Industrial Developments*2012, InTech.
84. Siesing, L., A. Reinap, and M. Andersson. *Thermal properties on high fill factor electrical windings: Infiltrated vs non infiltrated*. in *Electrical Machines (ICEM), 2014 International Conference on*. 2014.
85. Simpson, N., R. Wrobel, and P.H. Mellor, *A General Arc-Segment Element for Three-Dimensional Thermal Modeling.* Magnetics, IEEE Transactions on, 2014. 50(2): p. 265-268.
86. Staton, D.A. and A. Cavagnino, *Convection Heat Transfer and Flow Calculations Suitable for Electric Machines Thermal Models.* Industrial Electronics, IEEE Transactions on, 2008. 55(10): p. 3509-3516.
87. Schubert, E., *Heat Transfer coefficients at end winding and bearing covers of enclosed asynchronous machines.* Elektrie, 1968. 22.
88. A. Di Gerlando, I.V., *Thermal Networks of induction motors for steady state and transient operation analysis*, in *ICEM*1994.
89. Stokum, G., *Use of the results of the four-heat run method of induction motors for determining thermal resistance* Elektrotechnika, 1969. 62.
90. Taylor, G.I., *Distribution of Velocity and Temperature between Concentric Rotating Cylinders.* Proceedings of the Royal Society of London A: Mathematical, Physical and Engineering Sciences, 1935. 151(874): p. 494-512.
91. Howey, D.A., P.R.N. Childs, and A.S. Holmes, *Air-Gap Convection in Rotating Electrical Machines.* Industrial Electronics, IEEE Transactions on, 2012. 59(3): p. 1367-1375.
92. Becker, K.M. and J. Kaye, *Measurements of Diabatic Flow in an Annulus With an Inner Rotating Cylinder.* Journal of Heat Transfer, 1962. 84(2): p. 97-104.
93. Becker, K.M. and J. Kaye, *The Influence of a Radial Temperature Gradient on the Instability of Fluid Flow in an Annulus With an Inner Rotating Cylinder.* Journal of Heat Transfer, 1962. 84(2): p. 106-110.
94. Gaurav A., M.K., Sameer K., *Thermo-hydrodynamics of developing flow in a rectangular mini-channel array*, in *Proceedings of Twentieth National and Ninth International ISHMT-ASME Heat and Mass Transfer Conference*2010: Bombay, India.
95. Thirumaleshwar, M., *Fundamentals of Heat and Mass Transfer*2009: Pearson Education.
96. Ansys, *Fluent User Manual Version 14.5.7*.

# Appendices

## A. Dimensionless Numbers

In this section, equations of the dimensionless numbers will be provided

- Nusselt number:

$$Nu = \frac{h\ l}{k} \quad \text{A.1}$$

where $l$ is the characteristic length in m, $h$ the heat transfer coefficient in $W/m^2K$ and $k$ the fluid thermal conductivity in W/mK.

Several formulations of Nusselt numbers are available in literature as combination of dimensionless numbers as shown in Equations A.2 and A.3:

Natural convection $$Nu = a\ (Gr\ Pr)^b \quad \text{A.2}$$

Forced convection $$Nu = a\ (Re)^b\ (Pr)^c \quad \text{A.3}$$

Where a, b, c are constants depending upon the correlation used and Gr, Pr and Re are Grashof, Prandtl and Reynolds numbers which are shown in Equations A.4, A.5 and A.6.

- Grashof number:

$$Gr = \frac{\beta\ g\ \Delta T\ \rho^2\ l^3}{\mu^2} \quad \text{A.4}$$

Where β is the coefficient of cubical expansion of the fluid in $K^{-1}$, g is the gravitational acceleration in $m/s^2$, ΔT is the temperature gradient, ρ is the fluid density in $kg/m^3$ and μ is the fluid dynamic viscosity in kg/ms.

- Prandlt number:

$$Pr = \frac{C_p \, \mu}{k} \qquad \text{A.5}$$

where *Cp* is the fluid specific heat capacity in kJ/kgK.

- Reynolds number:

$$Re = \frac{\rho \, u \, l}{\mu} \qquad \text{A.6}$$

where *u* is the fluid velocity m/s.

- Graetz number

$$Gz = \frac{Re \, Pr}{l/d_h} \qquad \text{A.7}$$

Where $d_h$ is the hydraulic diameter in m.

# B. Theory behind the Lumped Parameters Thermal Network Method

The theory behind the Lumped Parameters Thermal Network method is essentially based on the analogy between thermal and electrical systems; this allows the resolution of a wide range of heat transfer problems by using the fundamental laws such as Ohm's and Kirchhoff's laws. Table B.1B.1 shows the thermal quantities corresponding to those of an electrical system.

| **Quantity** | **Thermal System** | **Electrical System** |
|---|---|---|
| Potential | T (K) | $V_E$ (V) |
| Flow | $\dot{Q}$(W) | I (A) |
| Resistance | $R_{th}$ (K/W) | R (Ω) |
| Capacitance | $C_{th}$ (J/K) | C (F) |

**Table B.1 Thermal-Electrical Analogy**

Before evaluating all thermal elements, the location and the number of nodes of the circuit must be defined, this step is called discretisation [79]. Nodes selection is usually an arbitrary process which might depend on the complexity

of the geometries or the need of a more accurate prediction of temperatures distribution; Figure B.0.aB.1 shows an example of discretisation of a simple system made of two bodies.

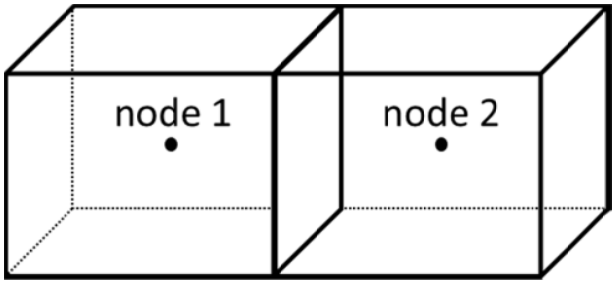



**Figure B.0.a: Discretisation**

Once the system is known, the thermal elements such as capacitance $C_{th}$ and resistance $R_{th}$ can be defined. $C_{th}$ can be estimated as in Equation B.1; this represents the ability of a body to store thermal energy and has to be included into the network when transient analyses should be carried out.

$$C_{th} = V\ \rho\ Cp \qquad \text{B.1}$$

Where V is the volume of the body in $m^3$, ρ is the density of the material in $kg/m^3$ and Cp the heat capacity in J/kg K.

Depending on the heat transfer mechanism involved, thermal resistances might be conductive, convective or radiative. The conductive resistance in Equation B.2 is function of the material thermal conductivity $k$ (W/mK), the length of the conductive path $l$ (m) and the cross-sectional heat transfer area $A$ ($m^2$). Figure B.0.b also shows a representation of the conductive thermal resistance of a simple homogeneous body.

$$R_{cond} = \frac{l}{k\ A} \qquad \text{B.2}$$

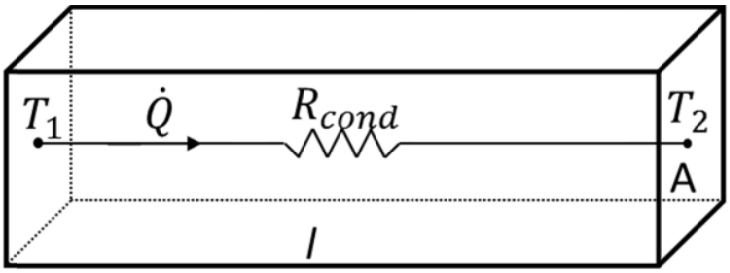



**Figure B.0.b: Conductive thermal resistance**

Equation B.3 shows the convective resistance as function of the surface area $A$ ($m^2$) and the convection heat transfer coefficient $h$ ($W/m^2K$)

$$R_{cond} = \frac{1}{h\,A} \qquad \text{B.3}$$

The challenge on quantification of the convective resistance is the estimation of the heat transfer coefficients. $h$ which strongly depends on the flow regime but also is affected by several factors such as surface shape and finish. Due to the complexity of the convective phenomena some empirical correlations, developed specifically for electrical machines, can be found in literature [10, 80]. In cases where heat transfer due to radiation can be significant, a radiative thermal resistance $R_{rad}$ can be also evaluated. As equation B.4 shows this resistance is function of surface area $A$ ($m^2$) and the radiation heat transfer coefficient $h_{rad}$ ($W/m^2K$). The determination of this quantity is a function of the emissivity of the surface, view factor and temperature; correlations can be found in literature [8].

$$R_{rad} = \frac{1}{h_{rad}\,A} \qquad \text{B.4}$$

When fluid flow is involved the determination of the amount of heat which can be absorbed by the coolant is required; this also gives an indication of the temperature rise of the coolant itself. By applying Ohm's Law to the thermal case, the heat flow is defined as the ratio between the temperature difference and the flow thermal resistance as in Equation B.5.

$$\dot{Q} = \frac{\Delta T}{R_{flow}} \quad \text{B.5}$$

Also the temperature rise ΔT of a fluid due to a heat input $\dot{Q}\,(W)$ can be expressed as in equation B.6 as the ratio between the power dissipated and the fluid density ρ (kg/m$^3$), fluid heat capacity Cp (J/kgK) and fluid volume flow rate $\dot{v}$ (m$^3$/s).

$$\Delta T = \frac{\dot{Q}}{\rho\, C_p \dot{v}} \quad \text{B.6}$$

It follows that the flow thermal resistance can be evaluated using equation B.7.

$$R_{flow} = \frac{1}{\rho\, C_p \dot{v}} \quad \text{B.7}$$

## B.1. Evaluation of critical parameters of electrical machines

Given the axisymmetric and geometrically simple nature of the electrical machines several components can be approximated to fairly simple geometries such as hollow cylinders and therefore the evaluation of most of thermal elements does not represent an issue.

However the use of additional models for the determination of thermal quantities is required for some critical areas such as:

- Stator slots – Containing windings made of copper and insulating material.
- End spaces – Region between stator lamination and end flanges, where end-windings are located.
- Airgap – Narrow gap located between the rotor outer diameter and stator inner diameter.
- Stator axial ducts – Ducts created to allow the fluid flow across the stator.
- Bearings.

In the next subsections the previous works in analysing these regions will be looked at in depth to establish the appropriate analysis approach for the work in this thesis.

### B.1.1 Stator Slots

From the thermal point of view stator slots can be considered as one of the most critical areas in electrical machines due to the high concentration of power losses. Slot cavities are randomly filled with multiple copper wires coated by a protective insulation layer, with empty spaces usually filled with an insulating resin to ensure short circuits do not occur as shown in Figure B.0.cB.3.

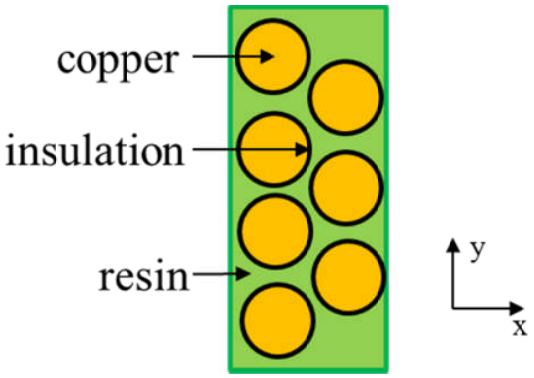
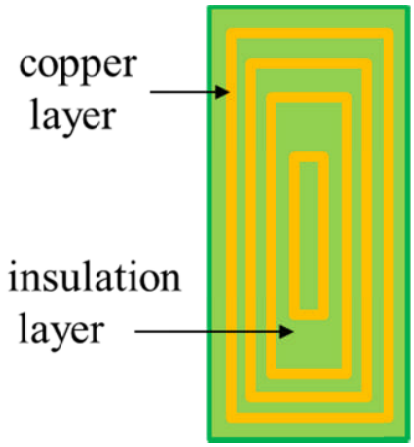



**Figure B.0.c: Typical wires distribution in slots**

The configuration described make the assessment of the thermal properties highly unpredictable, for this reason models such as the Layer Model [10] and the Cuboidal Model [58] have been used for the estimation of the overall slots properties.

The Layer Model, assumes that once the slot fill is known, the conductors which are expected to have similar temperature are lumped together. This leads to the assumption that the slot is made up of several layers of copper alternated by insulation layers as shown in FigureB.0.d The number of layers depends on the slot design, for example for slots containing a low number of thick wires

the number of layers will be small. This technique largely simplifies the process of estimating the thermal resistance.




**FigureB.0.d: Representation Layer Model**

When the Cuboidal Model is used instead windings are split into cuboids whose equivalent thermal conductivity is estimated using Equation B.8 which is function of thermal conductivities of materials constituting the slot such as copper $k_c$ , insulation $k_a$ and the volume of copper $v_c$.

$$k_{eq} = k_a \frac{(1+v_c)k_c + (1-v_c)k_a}{(1-v_c)k_c + (1-v_c)k_a} \qquad \text{B.8}$$

Whilst the thermal conductivity of the copper is known, $k_a$ must be calculated using the Equation B.9 as it represent the overall thermal conductivity of the resin and wire insulation together. Subscripts *ii* and *ci* represent the impregnation (resin) and conductor's insulation respectively.

$$k_a = k_{ii} \frac{v_{ii}}{v_{ii}+v_{ci}} + k_{ci} \frac{v_{ci}}{v_{ii}+v_{ci}} \qquad \text{B.9}$$

As literature shows, for the estimation of the overall thermal properties of electrical windings, several studies based on different approaches, were

conducted [58, 81-84]. Due to its reliability, the cuboidal model [58, 82, 85] described previously in this chapter was used in this work.

### B.1.2 End Spaces

The complexity of the fluid flow in the end regions is the result of the complex geometries and the influence of rotation. This area has been object of study for several authors having in common the use of the following experimentally derived formulation, Equation B.10 [86].

$$h = k_1 \left[1 + k_2 \, v^{k_3}\right] \qquad \text{B.10}$$

Where *v* is the reference velocity which is the average velocity of the rotating surfaces and the terms $k_1$, $k_2$, $k_3$ are curve fit coefficients. In particular $k_1$ accounts for the component of the natural convection, whilst $k_2$ and $k_3$ account for the convection due to rotation. Different values were proposed by different authors who investigated the phenomena at different operating conditions and locations as can be seen in Table B..2B.2.

| **Author** | $\boldsymbol{k_1}$ | $\boldsymbol{k_2}$ | $\boldsymbol{k_3}$ | **Case** |
|---|---|---|---|---|
| Mellor [30] | 15.5 | 0.39 | 1 | v< 7.5 m/s |
| Schubert [87] | 15 | 0.4 | 0.9 | End-Windings |
| Schubert [87] | 20 | 0.425 | 0.7 | Bearing cover |
| Di Gerlando [88] | 10 | 0.54 | 2 | End-Windings internal surface |
| Di Gerlando [88] | 40 | 0.1 | 1 | End ring |
| Stokun [89] | 33.2 | 0.0445 | 1 | Rotor end |

**Table B..2: End space curve fit coefficients**

All coefficients available in literature refer to air cooled machine in which the air velocity in the end spaces depends on the rotor velocity and the presence of fans. The different physics of the fluid flow in this work has required

numerical investigation to be carried out for the identification of the heat transfer coefficients in the end spaces; this are described in Chapter 5.

### B.1.3 Airgap

The airgap is a critical region in electric machines, not only from the electromagnetic point of view but from the thermal also. The prediction of the fluid flow and the heat transfer between concentric cylinders can be very challenging, especially at high rotational speeds, due to the formation vortices as observed by Taylor in [90]; several studies were carried out as shown in [91] leading to empirical correlations for the determination of the Nusselt number *Nu.* Factors such as the flow regime, the presence of axial flow and the presence of teeth slots can significantly affect the heat transfer.

For high speed applications, where rotating surfaces are smooth and no axial flow is expected, Nusselt number can be calculated using Equation B.11 proposed by Becker and Kaye in [92, 93].

$$Nu = 0.409 \left(\frac{Ta^2}{Fg^2}\right)^{0.241} \tag{B.11}$$

Where Ta is the Taylor number providing an indication of the relative effects of inertial forces and viscosity for an annulus (Equation B.12), and Fg is the geometric factor defined as in Equation B.13.

$$Ta = \frac{\omega\, r_m^{0.5}\, (r_s - r_r)^{1.5}}{\nu_a} \tag{B.12}$$

$$Fg = \frac{\pi^2}{41.19\,\sqrt{S}} \left(1 - \frac{r_s - r_r}{2\, r_m}\right)^{-1} \tag{B.13}$$

ω is the rotational speed in rad/s, $r_m$is the annulus mean diameter, $r_s$ and $r_r$ are the stator and rotor radii (m) and *S* is an non-dimensional coefficient function

of the annulus geometry. For an annulus in which only the inner cylinder is rotating *S* can be calculated using Equation B.14.

$$S = 0.0571\left[1 - 0.652\left(\frac{r_s - r_r}{r_r}\right)\right] + 0.0056\left[1 - 0.652\left(\frac{r_s - r_r}{r_r}\right)\right]^{-1} \quad \text{B.14}$$

Windage, the viscous heat generated due air shear stress during rotation, can be calculated using Equation 2.9.

### B.1.4 Stator Axial Ducts

The distribution of the axial ducts allowing the oil flowing through the stator lamination is described in Chapter 3.

Several empirical correlations are available in literature for the determination of the Nusselt number in ducts [8], they can vary according the flow regime and duct geometry; a better understanding of the fluid flow is required first.

The total flow rate used for the whole machine was 15 lt/min. Assuming an even distribution of oil among all ducts, the Reynolds number calculated is Re= 540; being well below 2000 means that the flow regime is laminar. The following step is establishing if the fluid flow is fully developed; this is an important aspect which should be taken into account given that in the entrance region the Nusselt number can be significantly higher. The entrance region can be evaluated using Equation B.15, where $d_h$ is the hydraulic diameter defined as $d_h = 4A/P$ where A is the cross sectional area and P the section perimeter.

$$X = 0.05\, Re\, d_h \quad \text{B.15}$$

The entrance region calculated is 55 mm, representing around the 75% of the whole duct length which is 80 mm long; it follows that a correlation for non-fully developed flow may be more appropriate. For comparison two different correlations were used [94, 95] and these are presented in Equation B.16,

which is also integrated in MotorCAD and Equation B.17; both are suitable for square pipes with laminar flow and non-fully developed flow.

$$Nu = 3.65 + \frac{0.0668\,(d_h/l)Re\,Pr}{1 + 0.04\,[(d_h/l)\,Re\,Pr]^{2/3}} \qquad \text{B.16}$$

$$\frac{Nu}{4.364\,[1 + (Gz/29.6)^2]^{1/6}} = \left[1 + \left(\frac{Gz/19.04}{\left[1 + (Pr/0.0207)^{2/3}\right]^{1/2}\,\left[1 + (Gz/29.6)^2\right]^{1/3}}\right)^{3/2}\right]^{1/3} \qquad \text{B.17}$$

Where $Gz$ is the Graetz number defined in Appendix A.

Both correlations lead to very similar results of Nusselt number (13.5 and 15 respectively), leading to heat transfer coefficients between 865 and 975 W/m$^2$K.

The pressure drop across the pipe Δp can be estimated using the Darcy-Weisbach formulation shown in Equation B.18.

$$\Delta p = f_D\,\frac{l}{D}\,\frac{\rho\,u^2}{2} \qquad \text{B.18}$$

Where $f_D$ is the dimensionless Darcy friction factor, $l$ is the pipe length (m), D is the pipe hydraulic diameter (m), $\rho$ is the fluid density (kg/m$^3$) and $u$ is the fluid mean velocity calculated as the ratio between the volumetric flow rate and the pipe cross sectional area. As the flow regime expected is laminar, the Darcy friction factor can be calculated as 64/Re. A pressure drop of just 3 kPa is expected.

### B.1.5 Bearings

The point contact between spheres and races introduce a significant complications on the thermal modelling of bearings, additionally the use of lubricants such as oil or grease makes the determination of an equivalent thermal resistance even more challenging.

Based on some experimental data, Motor-CAD has treated this component as an equivalent interference gap [11]. Table B.3 shows some data currently available in literature.

| Motor | Inner Diameter [mm] | Outer Diameter [mm] | Width [mm] | Equivalent interface gap [mm] |
|---|---|---|---|---|
| 4 kW | 30 | 72 | 19 | 0.35 |
| 7.5 kW | 40 | 80 | 18 | 0.23 |
| 15 kW | 45 | 100 | 25 | 0.40 |

**Table B.3: Bearing equivalent interface gap**

In order to get a better understanding of the heat transfer within the bearings used in the machine design, a thermal network for the bearing chambers was developed in Mat-Lab Simulink and this is presented later in section 4.4.

## B.2 Calculation Bearing Friction losses

As described in section 4.4.3 the Palmgren's model used for the estimation of the bearing friction loss is given by Equation 4.2.

The viscous friction torque $M_0$ is defined as in Equation B.19, where $d_m$ is the bearing mean diameter in mm, ν the lubricant viscosity in cSt, n the rotational speed in rpm and $f_0$ is a tabled coefficient depending on the bearing type and lubrication method. This empirical correlation can be used when the product $(\nu \cdot n) > 2000$ and when oils with density around 900 kg/m$^3$ are employed.

$$M_0 = 10^{-7} f_0 \, d_m^3 (\nu \, n)^{2/3} \quad \text{B.19}$$

The frictional torque $M_1$ due to the applied load is given in Equation B.20.

$$M_1 = P \, f_1 \, d_m \quad \text{B.20}$$

Where *P* is the equivalent dynamic load in N that for angular contact bearings is calculated as in Equation B.21, where α is the characteristic angle of the bearing and *Pa* and *Pr* are the axial and radial loads in N respectively, for cylindrical roller bearings *P=Pr* which has been assumed as the half of the total weight of the rotor.

$$P = 0.9 \, P_a \, \cot(\alpha) - 0.1 \, P_r \quad \text{B.21}$$

The coefficient $f_1$ is function of the bearing design and is calculated as in Equation B.22, where *z* and *y* are tabled values and *Cs* is the static load rating provided by the manufacturer.

$$f_1 = z \left( \frac{Ps}{Cs} \right)^y \quad \text{B.22}$$

*Ps* is the equivalent static load in N defined as in Equation B.23 where the coefficient $Y_0$ is provided by the manufacturer. For cylindrical roller bearings *Ps = Pr.*

$$P_s = P_r + Y_o \, P_a \quad \text{B.23}$$

The SKF loss model was presented in Equation 4.3

$M_{rr}$ and $M_{sl}$ are calculated using Equations B.24 and B.25

$$M_{rr} = G_{rr} (n \, \nu)^{0.6} \quad \text{B.24}$$

$$M_{sl} = G_{sl} \mu_{sl} \quad \text{B.25}$$

Where $\nu$ is the lubricant kinematic viscosity in $mm^2/s$, $n$ the rotating speed in rpm and $\mu_{sl}$ is the sliding friction coefficient which is function of the bearing and lubricant used (0.04 for ball bearings lubricated with synthetic oils and 0.02 for cylindrical roller bearings). The expression used to calculate $G_{rr}$ and $G_{sl}$ vary according the bearing used.

*Paired Angular Contact Bearings*

$G_{rr}$ and $G_{sl}$ for angular contact bearings are calculated using Equations B.26 and B.27

$$G_{rr} = R_1\, dm^{1.97}[Fr + (R_3\, dm^4 n^2) + R_2 Fa]^{0.54} \quad \text{B.26}$$

$$G_{sl} = S_1\, dm^{0.26}\left[(Fr + S_3 dm^4 n^2)^{\frac{4}{3}} + S_2 Fa^{\frac{4}{3}}\right] \quad \text{B.27}$$

Where $d_m$ is the bearing mean diameter in mm, Fr is the external radial load (assumed as 50% of the rotor weight, 26.4 N) and Fa is the external axial load (assumed equal to the preload applied, 100 N). All other coefficients are tabled for this bearing type in Table B.4B.4.

| | | |
|---|---|---|
| $S_1$ = 0.00756 | $S_2$ = 1.21 | $S_3$ = 7.83E-13 |
| $R_1$ = 6.34E-07 | $R_2$ = 1.41 | $R_3$ = 7.83E-13 |

**Table B.4: S and R values for paired angular contact bearings**

*Cylindrical Roller Bearings*

$G_{rr}$ and $G_{sl}$ for cylindrical roller bearings are calculated using Equations B.28 and B.29.

$$G_{rr} = R_1\, dm^{2.41}\, Fr^{0.3}(\nu\, n)^{0.6} \quad \text{B.28}$$

$$G_{sl} = S_1\, dm^{0.9}\, F_a + S_2\, dm\, F_r \qquad \text{B.29}$$

In this case no axial preload is applied so Fa = 0. Coefficients $R_1$, $S_1$ and $S_2$ are listed in Table B.5B.5.

| | | |
|---|---|---|
| $S_1$ = 0.17 | $S_2$ = 0.0015 | $S_3$ = N/A |
| $R_1$ = 1.12E-06 | $R_2$ = N/A | $R_3$ = N/A |

**Table B.5: S and R values for cylindrical roller bearings**

*Reduction Factors*

$$\phi_{ish} = \frac{1}{1 + 1.84 \cdot 10^{-9} (n\, dm)^{1.28}\, \nu^{0.64}} \qquad \text{B.30}$$

$$\phi_{rs} = \frac{1}{e^{K_{rs}\, \nu\, n\, (d+D) \sqrt{\frac{K_z}{2(D-d)}}}} \qquad \text{B.31}$$

*D* and *d* are the outer and inner bearing diameters respectively. Krs is $3*10^{-8}$ for oil jet lubrication. Kz depends on the bearing type as shown in Table B.5B.6.

| **Bearing** | **Kz** |
|---|---|
| Cylindrical roller bearing | Kz = 6.2 |
| Paired Angular contact bearings | Kz = 3.1 |

**Table B.5: Kz values**

Bearing friction losses calculated at different operating speeds (between 1,000 and 32,000) and different oil temperatures are shown in Figure B.0.eB.5.

| | Bearing Losses (W) | | | | | | | |
|---|---|---|---|---|---|---|---|---|
| | SKF | | | | Palmgren | | | |
| | Angular contact | | Cylindrical roller | | Angular contact | | Cylindrical roller | |
| Speed (rpm) | Oil at 40°C | Oil at 100°C | Oil at 40°C | Oil at 100°C | Oil at 40°C | Oil at 100°C | Oil at 40°C | Oil at 100°C |
| 32000 | 231.6 | 179.5 | 122.9 | 100.5 | 414.4 | 169.8 | 393.3 | 163.3 |
| 31000 | 215.8 | 164.9 | 120.6 | 96.9 | 393.2 | 161.2 | 373.3 | 155.1 |
| 30000 | 200.6 | 151.2 | 118.1 | 93.2 | 372.5 | 152.8 | 353.7 | 147.0 |
| 29000 | 186.1 | 138.2 | 115.5 | 89.5 | 352.3 | 144.6 | 334.5 | 139.2 |
| 28000 | 172.2 | 126.0 | 112.8 | 85.8 | 332.5 | 136.5 | 315.8 | 131.5 |
| 27000 | 158.9 | 114.5 | 109.9 | 82.1 | 313.1 | 128.7 | 297.5 | 124.0 |
| 26000 | 146.3 | 103.8 | 106.9 | 78.3 | 294.2 | 121.0 | 279.6 | 116.6 |
| 25000 | 134.2 | 93.7 | 103.7 | 74.6 | 275.8 | 113.5 | 262.2 | 109.5 |
| 24000 | 122.7 | 84.4 | 100.4 | 70.9 | 257.9 | 106.2 | 245.2 | 102.5 |
| 23000 | 111.9 | 75.6 | 97.0 | 67.1 | 240.4 | 99.1 | 228.7 | 95.7 |
| 22000 | 101.6 | 67.5 | 93.4 | 63.4 | 223.4 | 92.1 | 212.6 | 89.1 |
| 21000 | 91.8 | 60.0 | 89.6 | 59.6 | 207.0 | 85.4 | 197.0 | 82.7 |
| 20000 | 82.7 | 53.1 | 85.7 | 55.9 | 191.0 | 78.9 | 181.8 | 76.4 |
| 19000 | 74.0 | 46.7 | 81.6 | 52.2 | 175.5 | 72.6 | 167.2 | 70.4 |
| 18000 | 65.9 | 40.9 | 77.5 | 48.6 | 160.6 | 66.5 | 153.0 | 64.5 |
| 17000 | 58.4 | 35.6 | 73.1 | 44.9 | 146.2 | 60.6 | 139.4 | 58.9 |
| 16000 | 51.4 | 30.8 | 68.7 | 41.3 | 132.3 | 54.9 | 126.2 | 53.4 |
| 15000 | 44.9 | 26.4 | 64.1 | 37.8 | 119.0 | 49.5 | 113.6 | 48.2 |
| 14000 | 38.9 | 22.4 | 59.4 | 34.3 | 106.2 | 44.2 | 101.5 | 43.1 |
| 13000 | 33.4 | 18.9 | 54.6 | 30.9 | 94.1 | 39.2 | 89.9 | 38.3 |
| 12000 | 28.4 | 15.8 | 49.7 | 27.5 | 82.5 | 34.5 | 78.9 | 33.8 |
| 11000 | 23.8 | 13.0 | 44.7 | 24.3 | 71.5 | 30.0 | 68.5 | 29.4 |
| 10000 | 19.8 | 10.6 | 39.7 | 21.1 | 61.2 | 25.7 | 58.6 | 25.3 |
| 9000 | 16.1 | 8.5 | 34.7 | 18.1 | 51.5 | 21.7 | 49.4 | 21.4 |
| 8000 | 12.9 | 6.7 | 29.7 | 15.1 | 42.5 | 18.0 | 40.8 | 17.8 |
| 7000 | 10.1 | 5.2 | 24.8 | 12.4 | 34.1 | 14.5 | 32.9 | 14.4 |
| 6000 | 7.7 | 3.9 | 20.1 | 9.8 | 26.5 | 11.4 | 25.6 | 11.3 |
| 5000 | 5.6 | 2.8 | 15.5 | 7.4 | 19.7 | 8.5 | 19.1 | 8.5 |
| 4000 | 3.9 | 1.9 | 11.2 | 5.2 | 13.7 | 6.0 | 13.4 | 6.1 |
| 3000 | 2.4 | 1.2 | 7.3 | 3.3 | 8.6 | 3.8 | 8.4 | 3.9 |
| 2000 | 1.3 | 0.6 | 3.9 | 1.8 | 4.5 | 2.0 | 4.4 | 2.1 |
| 1000 | 0.4 | 0.2 | 1.3 | 0.6 | 1.5 | 0.7 | 1.5 | 0.8 |

**Figure B.0.e: Bearing Power Losses**

## B.2.1 Simulink Thermal Network

# C. Theory Behind CFD

## C.1 Fluid Flow Equations

The set of Navier-Stokes equations governing fluid flow, includes three distinct momentum equations along all three dimensional directions, and these are solved with the continuity equation and the energy equation (Equation C.1 to Equation C.5) [35]:

x-momentum $$\rho \frac{Du}{Dt} = -\frac{\partial \rho}{\partial x} + div(\mu\ grad\ u) + S_{Mx} \quad \textbf{C.1}$$

y-momentum $$\rho \frac{Dv}{Dt} = -\frac{\partial \rho}{\partial y} + div(\mu\ grad\ v) + S_{My} \quad \textbf{C.2}$$

z-momentum $$\rho \frac{Dw}{Dt} = -\frac{\partial \rho}{\partial z} + div(\mu\ grad\ w) + S_{Mz} \quad \textbf{C.3}$$

continuity $$\frac{\partial \rho}{\partial t} + div(\rho u) = 0 \quad \textbf{C.4}$$

energy $$\rho \frac{Di}{Dt} = -\rho\ div\ u + div(k\ gradT) + \Phi + S_i \quad \textbf{C.5}$$

The complete Navier-Stokes equations in integral form may be represented by the transport equation using the variable φ as in Equation C.6:

$$\frac{\partial}{\partial t}\left(\int_V \rho\phi dV\right) + \int_A \vec{n}(\rho\phi\vec{u})dA = \int_A \vec{n}(\Gamma grad\phi)dA + \int_V S_\phi dV \qquad \textbf{C.6}$$

In words this equation can be described as

| Rate of increase of φ | + | Net rate of decrease of φ due to convection across the boundaries | = | Rate of increase of φ due to diffusion across the boundaries | + | Net rate of creation of φ due to sources |
|---|---|---|---|---|---|---|

Replacing the property φ by for velocities along x, y and z-directions, the momentum equations are formed, if the internal energy *i* is used instead the energy equation is formed [35].

## C.2 Turbulence Modelling

Turbulent flow can be solved by Navier-Stokes equations if the cells size is smaller than the Kolmogorov length scale [35], this is known as Direct Numerical Solution (DNS); however this would require extremely fine meshes and computational efforts far beyond the capabilities of ordinary PCs. Due to the rotational, unsteady, and highly irregular nature of turbulence the problem cannot be approached directly and for this reason several turbulence models were introduced.

In most of engineering problem the time averaged velocity is sufficient; the velocity components are then split into a fluctuating $u_i'$ and mean $\bar{u}_I$ components as in Equation C.7

$$u_i = \overline{u_i} + u_i' \qquad \text{C.7}$$

By substituting this velocity into the Navier-Stoke equations a new set of equations known as Reynolds Averaged Navier-Stokes (RANS) are obtained. This leads to six additional terms, known as Reynolds Stresses, leaving open equations; turbulence models are used to close these equations.

One of the most widely used models, robust and suitable for most of engineering problems is the two-equation Standard k-ε, an Eddy Viscosity Model (EVM) based on the Boussinesq approximation; this approximation treats density as a constant value in all solved equations, except for the buoyancy term in the momentum equation. k and ε are the turbulent kinetic energy and the dissipation rate respectively, defined as in Equation C.8 and Equation C.9.

$$k = \frac{1}{2}(u'^2 + v'^2 + w'^2) \tag{C.8}$$

$$\varepsilon = \frac{dk}{dt} \tag{C.9}$$

Other variants of the two-equation k-ε models are available:

- RNG k-ε, suitable for complex shear flows involving rapid strain, moderate swirl, vortices, and locally transitional flows; it can cause convergence issues and unstable solutions.
- Realizable k-ε, can provide superior performance compared with the Standard k-ε model for flows involving rotation.

The selection of a turbulence model depends on the problem analysed and the flow nature expected; for example for problems involving external flows where viscous forces are significant the Shear Stress Transport (SST) k-ω can be more appropriate. This is a Reynolds Stress Model (RSM).

The Reynolds Stress Models, RSM, generally do not assume the turbulence to be isotropic as in the EVM models. They use six different transport equations to model each of the six distinct Reynolds stresses. Generally the computational costs involved to solve these equations outweigh their benefits [15].

Due to its stability and suitability for modelling electrical machines [70] the k-ε turbulence model was used in this work.

## C.3 Wall Treatment

Depending on the case walls can be the main source of vorticity and turbulence and usually increase the turbulent momentum and the thermal boundary layers, especially in near-walls regions where sharpest gradients occur. An accurate modelling of the wall effects is then important for a successful prediction of frictional drag, pressure drops, thermal boundary layer, etc.

Plotting the dimensionless velocity $U/U_\tau$, where $U_\tau$ is the friction velocity, against the dimensionless wall distance $y^+$ as shown in Figure C.1, a profile common to many flows in the proximity of the walls is obtained. Depending on the order of the viscous effects, in the boundary layer three regions can be identified; the viscous sublayer where the viscous effects are dominant, a buffer layer where both contributes are comparable, and the fully turbulent region where turbulence plays a major role.

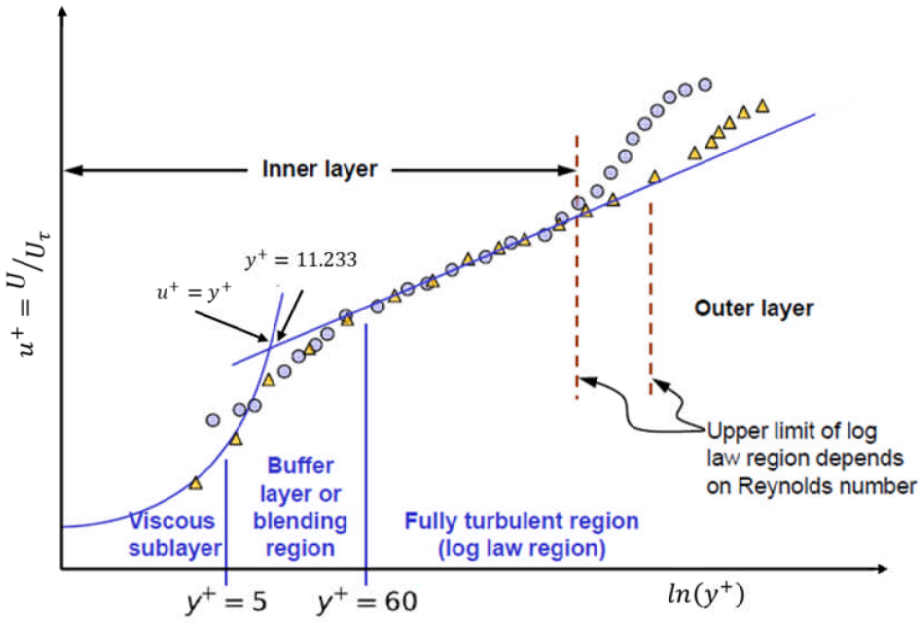



**Figure C.1: Near-Wall Regions [96]**

$U_\tau$ and $y^+$ are defined in Equation C.10 and Equation C.11 respectively, where $\tau_{wall}$ is the shear stress, $\rho$ the fluid density, $y$ the wall distance and $\nu$ the fluid kinematic viscosity.

$$U_\tau = \sqrt{\frac{\tau_{wall}}{\rho}} \qquad \text{C.10}$$

$$y^+ = \frac{yU_\tau}{\nu} \qquad \text{C.11}$$

Two wall modelling strategies are commonly available in CFD; the Wall Function Approach and the Near-Wall Model Approach shown in Figure C.2 C.2. The latter is capable of resolving the viscous sublayer but requires a $y^+$value of about 1, implying that the mesh count can significantly increase; the Wall Function instead does not resolve the viscous sublayer and requires significantly lighter meshes the $y^+$ needed being between 30 and 300.

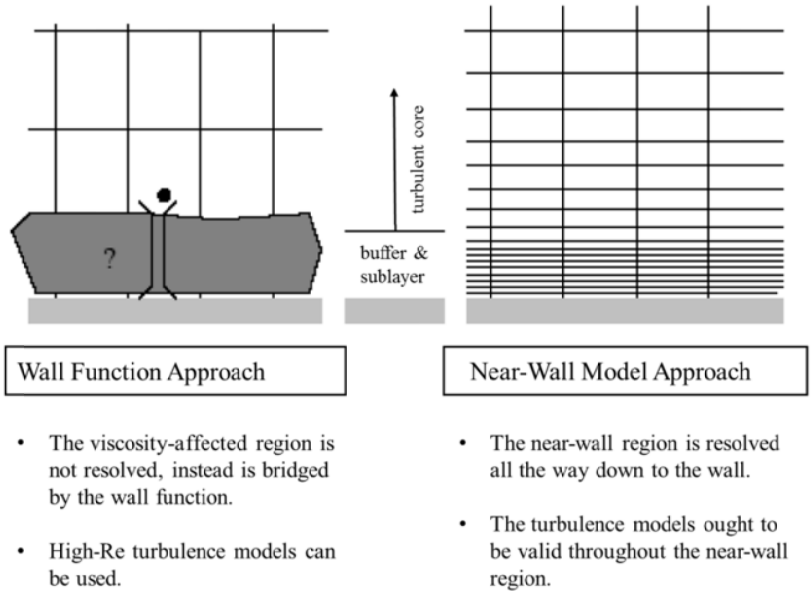



**Figure C.2: Wall Modelling Approaches [96]**

The choice of the approach depends on the level of accuracy required at the wall, so for problems involving aerodynamic drag, turbomachinery blade performance the Near-Wall Model Approach is required.

As within this work there is a requirement to estimate the viscous heat generated due to the rotation, especially in the airgap, the Enhanced Wall

Treatment function available in Ansys Fluent is used; this allows an automatic switch from approach to another depending on the $y^+$ set.

## D. CFD General Algorithm

Several CFD codes are currently available, however the approach and the algorithms used when carrying out numerical studies are the same for all of them, Figure D.1 shows the general process followed.

The definition of the problem is an extremely important step; quantities looked for, degree of accuracy required and domain needed should be clearly known before using any software.

The following three main components usually constitute a CFD code:

- Pre-Processor – Once goals and domain are identified the geometry is created and discretised into subdomains, boundary conditions are defined and appropriate physical models are selected.
- Solver – The discretised conservation equations are solved iteratively for each element until convergence.
- Post-Processor – Data obtained can be processed and their accuracy analysed.

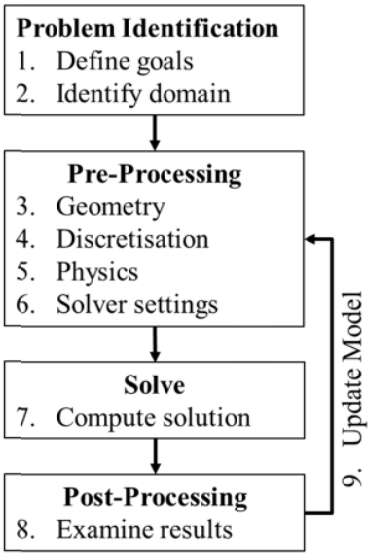



**Figure D.1: CFD process**

A general description of these steps will be initially provided, followed by a more detailed description of the domains analysed.

## D.1 Domain Identification

The identification of the domain is generally strictly linked to the goals defined; however the choice can also be based on the user's experience. The first consideration regards the domain extent, this can be limited to the fluid domain or both fluid and solids domains when dealing with conjugate heat transfer analyses. In the case of problems involving axisymmetric domains, as in the case of electrical machines, it can be chosen whether modelling the full 3D domain [69], a limited sector as done in [15, 91] or, if geometries are particularly simple, a 2D section only.

## D.2 Geometry of Domain

When generating the domain the main target is creating an optimised geometry for the CFD analysis capable of capturing the most crucial fluid flow and heat transfer phenomena; often, this requires some simplifications to be done on the original domain.

As the situations analysed within this thesis relate to an axisymmetric case most of the domains analysed consist of 20 degrees sectors. A full 360 degrees model was also created to validate the accuracy of these 20 degree sectors.

In addition to symmetry geometrical simplifications are often required, either because some features' contribution to the analysis outcome might not be relevant but also to for improving mesh quality and hence reducing the computational cost of the simulations and improving the stability of the solutions.

In electrical machines for example some components such as electrical windings, laminated materials, bearings, etc are modelled as bulk solids, significantly reducing the mesh count. This modelling strategy is also adopted in this work.

Other small features such as bolts, connectors, threads are not modelled as they would only add mesh complexities leading to computation issues. But have a negligible impact on the heat or fluid flow.

## D.3 Domain Discretisation

As mentioned earlier in this chapter, CFD iteratively solves equation for every sub-domains created; a good discretisation, or mesh, is then the key for computing accurate solutions.

The discretisation is carried out by fragmenting the whole domain into small volumes, or cells; when working with 3D cases, CFD codes usually employ tetrahedral (tetra), hexahedral (hexa), prismoidal (prism) or pyramidal volumes shown in FigureD.2. Ansys Mesher, the software used in this work, mostly uses tetrahedral and hexahedral elements.

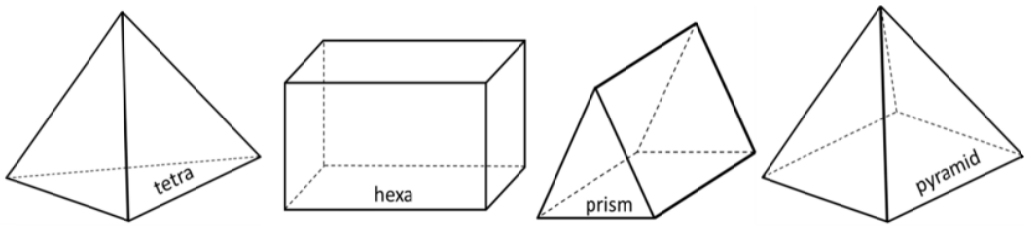



**Figure D.2: Typical Mesh Elements**

The use of the optimal number of cells (mesh density) and the selection of the right cell type are the factors which mostly affect the accuracy of the solutions. When modelling multi-body geometries both mesh density and cell type can vary within the domain; this strongly depends on the complexity of the geometries, dimensions and zone type (fluid or solid regions). The user's experience also plays an important role on the generation of a good mesh.

For solid regions having simple geometries hexa elements are commonly used, this tends to reduce the mesh count and hence the calculation time. Fluid domains, unless they consist of straight pipes or narrow gaps, are usually discretised using tetra elements as it has been done in this work; however for more accurate boundary layer resolution hexa elements are used in near-wall

regions and the creation of inflation layers is then required. Higher mesh densities are usually required in fluid domains to accurately determine gradients in flows. Generally speaking, hexa elements lead to quicker solution convergence and, in case of mesh adaption, cell quality remains unchanged; using tetra elements instead angles might deteriorate leading to high skewed cells which can be source of numerical inaccuracies. The skewness is defined by Equation D.1 where the optimal cell size refers to an equilateral cell; skewness above 0.97 is considered unacceptable. All meshes generated in this work have a maximum skewness of 0.95 which is considered acceptable [96]. This parameter generally gives an indication about the quality of the mesh generated.

$$Skewness = \frac{optimal\ cell\ size - cell\ size}{optimal\ cell\ size} \qquad \text{D.1}$$

Another important statistic used to judge the quality of the mesh the aspect ratio which is defined as the ratio between the long and the short edges of the element; generally this value should not exceed 100.

The mesh count has also a significant impact on the computational effort required as equations are solved for each element; finer meshes are then only recommended for limited regions where higher gradients are expected, this aims to resolve the most relevant flow details. The approach commonly used consists of starting computing the case using a coarse mesh, then gradually refining the mesh until the same solution is obtained; this process is called Mesh Independency Analysis. Due to the large number of components constituting the machine, the Mesh Independency Analysis was conducted for some regions only as discussed in section 5.3.

## D.4 Solver Settings

Once the domains are defined and the turbulence model is selected, it is necessary to specify in which order the Reynolds Averaged Navier-Stokes

equations are solved and the degree of accuracy the field variables should be interpolated within each cell. Two solvers are available in Fluent:

- Pressure Based
- Density Based

The first solves mass and momentum equations are solved at the same time, followed by the energy equation and the turbulence equations. The second solver instead solves mass, momentum and energy at the same time followed by the turbulence equations last. Whilst the Density Based solver is recommended for high speed compressible flows involving combustion or hypersonic flows, the Pressure Based solver is applicable for a wide range of compressible flows and also requires lower memory; for these reasons the Pressure Based solver is preferred in this work.

During the computation variables are stored at the centre of the grid cell, $\varphi$, these must be interpolated to the faces of the control volumes, $\varphi_f$ (Figure D.D.3).

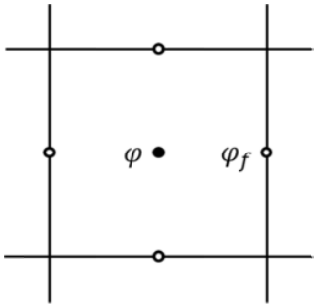



**Figure D.3: Control Volume**

Four interpolation schemes are available in Fluent [96]:

- *First-Order Upwind* – Is the easiest to converge being only first-order accuracy scheme; this implies that the face values is set equal to the cell-centre value of $\varphi$ in the upstream cell.

- *Power Law* – This scheme interpolates the face value of a variable, using the exact solution to a one-dimensional convection-diffusion equation. It is recommended for flows with very low Reynolds number.
- *Second-Order Upwind* – Being a 2nd order accuracy scheme, it is more accurate of the previous schemes described. Using this scheme $\varphi_f$ depends on cell-centred values, its gradient $\nabla\varphi$ and the vector $\vec{r}$ directed from the cell centroid toward the face centroid upstream cell gradient (Equation D.2). This scheme is essential when mostly tetrahedral elements are used; for this reason it was employed in this work.

$$\varphi_f = \varphi + \nabla\varphi\,\vec{r} \qquad \text{D.2}$$

- *Quadratic Upwind Interpolation* (QUICK) – Is more accurate of the schemes above described, being a 3rd order accuracy scheme, but it can only be used with hexa dominant meshes.

When using the Pressure Based solver, numerical algorithms for the pressure-velocity coupling must be implemented; these use a combination of continuity and momentum equations to derive an equation for pressure. Within Fluent the most robust and suitable for steady-state simulation is the Semi-Implicit Method for Pressure-Linked Equations algorithm, known as SIMPLE.

## D.5 Convergence

The number of iterations to a converged solution is linked to the domain extensions, mesh count and physics involved.

The following conditions should be satisfied in order to consider the solution converged:

- The solution is steady and it does not change with subsequent iterations.
- Overall momentum, mass and energy are balanced.

- All equations are obeyed in all control volumes to a specified tolerance.

The difference between the previous and current result of an equation is called residual; in Fluent this can be plotted for all equations providing a good indication of the solution accuracy and whether the solution has convergence issues or not. Additional monitors can be also created and plotted for quantities which can be particularly important for the type of problem considered. In the case of electrical machines a parameter to be monitored is the moment given by the viscous force generated on the rotor surface due to the rotation; this is particularly important for achieving an accurate prediction of the windage generated.

General Fluent guidelines suggest that good convergence can be assumed when continuity and momentum equations converge with an order of $10^{-3}$ and $10^{-7}$ for the energy equation. For particularly complex domains $10^{-3}$ might not be achieved but if residuals no longer change an order of $10^{-2}$ can still be considered converged.

## D.5 Post-Processing

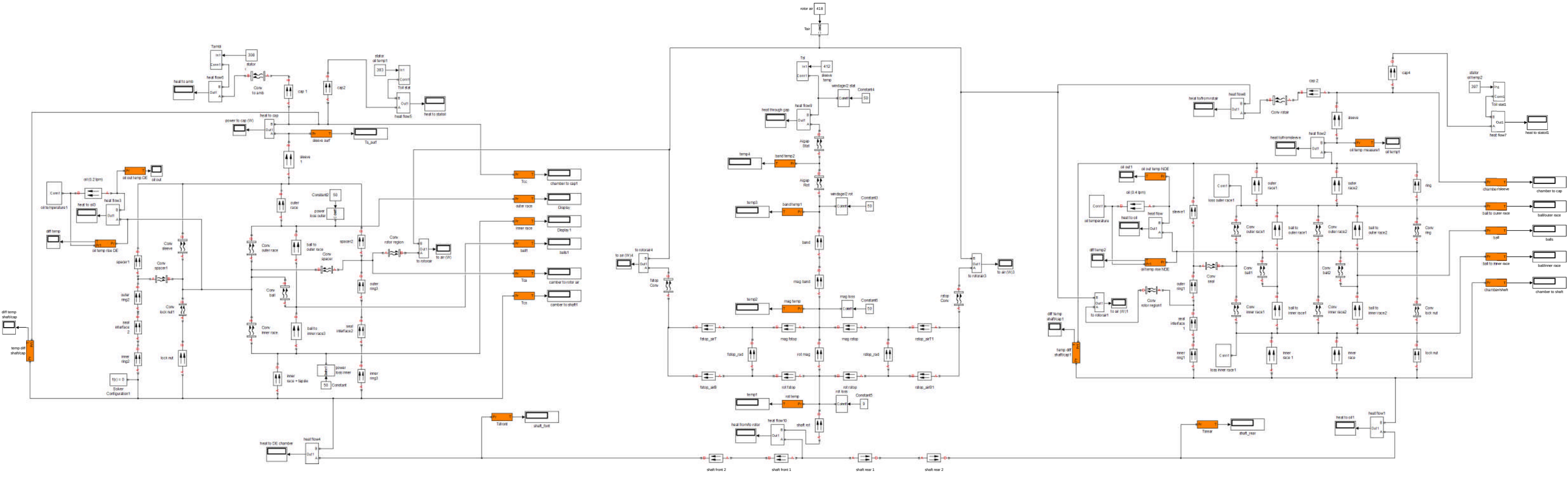
Post-Processing groups all operations aiming to analyse the numerical data computed. Before extracting data, solution results need to be checked in order to assess their consistency; this is generally based on the user judgement as a converged solution does not necessarily mean reliable results. Once the solution has been checked, data of interest can be plotted using graphs, contours, streamlines or vectors.

# E. PC Specification

Analytical and Numerical analyses were carried out using a desktop PC.

| | |
|---|---|
| Operating System | Windows 7 – 64 bit |
| Processor | Intel Core i7 2.79 GHz |
| RAM | 24 |
| Graphics Card | NVIDIA Quadro 2000 |

**Table E.1: PC specification**


rotor air
418
Tair
Tsl
412
sleeve temp
windage2 stat
Constant4
50
heat through gap
heat flow9
Out1
Adjust Stat
temp4
band temp2
Adjust Rot
temp3
band temp1
windage2 rot
Constant3
50
band
to rotorair4
to air (W)14
fstop Conv
mag band
temp2
mag temp
mag loss
Constant6
50
fstop_airT
mag fstop
mag rstop
rstop_airT1
fstop_rad
rot mag
rstop_rad
fstop_air8
rot fstop
rot rstop
rstop_air81
temp1
rot temp
rot loss
Constant5
0
heat from/to rotor
heat flow10
shaft rot
to rotorair3
to air (W)3
rstop Conv
shaft front 2
shaft front 1
shaft rear 1
shaft rear 2
Tcc
chamber to cap1
outer race
Display
Tir
Display1
Tcs
cambar to rotor air
Tca
cambar to shaft1
Tstator
stator oil temp1
393
Toil stat
heat flow5
heat to stator
Tamb
308
stator
heat to amb
Conv to amb
cap 1
cap2
power to cap (W)
heat to cap
sleeve surf
Ts_surf
sleeve 1
oil (0.2 lpm)
oil out temp DE
oil out
oil temperature1
heat to oil3
heat flow3
diff temp
oil temp rise DE
Conv sleeve
spacer1
Conv spacer1
outer ring2
seal interface 2
inner ring2
Conv lock nut1
lock nut
f(u) = 0
Solver Configuration1
Constant2
50
power loss outer
Conv outer race
ball to outer race
Conv spacer
spacer2
Conv rotor region
to rotorair
to air (W)
outer ring3
Conv ball
Conv inner race
ball to inner race3
seal interface2
inner race + ballss
power loss inner
50
Constant
inner ring3
heat to DE chamber
heat flow4
Tdrive
shaft_front
temp diff shaftcap
diff temp shaftcap
cap4
cap 2
heat to/from rotor
heat flow8
Conv rotor
sleeve
heat to/from sleeve
heat flow2
oil temp measure1
oil temp1
stator oil temp2
397
Toil stat1
heat flow7
heat to stator1
oil out 1
oil out temp NDE
oil (0.4 lpm)
oil temperature
heat to oil
heat flow
Out1
sleeve1
diff temp2
oil temp rise NDE
Conv seal
outer ring1
seal interface 1
inner ring1
Conv rotor region1
to rotorair1
to air (W)1
temp diff shaftcap1
diff temp shaftcap1
loss outer race1
outer race1
outer race2
ring
Conv outer race1
ball to outer race1
Conv outer race2
ball to outer race2
Conv ring
Conv ball1
Conv ball2
Conv inner race1
ball to inner race1
Conv inner race2
ball to inner race2
Conv lock nut
loss inner race1
inner race 1
inner race
lock nut
Tdrear
shaft_rear
heat to oil1
heat flow1
chamber/sleeve
chamber to cap
ball to outer race
ballouter race
ball
balls
ball to inner race
ballinner race
chamber/shaft
chamber to shaft